

The Pennsylvania State University

The Graduate School

Department of Energy and Geo-Environmental Engineering

**DETERMINATION OF MECHANICAL AND HYDRAULIC BEHAVIOR OF
TENSILE FRACTURES UNDER MULTIPHASE FLOW USING X-RAY
COMPUTED TOMOGRAPHY**

A Thesis in

Petroleum and Natural Gas Engineering

by

Freddy Alvarado

© 2005 Freddy Alvarado

Submitted in Partial Fulfillment
of the Requirements
for the Degree of

Doctor of Philosophy

December 2005

The thesis of Freddy Alvarado has been reviewed and approved* by the following:

Abraham S. Grader
Professor of Petroleum and Natural Gas Engineering
Thesis Co-Advisor
Co-Chair of Committee

Phillip M. Halleck
Associate Professor of Energy and Geo-Environmental Engineering
Thesis Co-Advisor
Co-Chair of Committee

Turgay Ertekin
Professor of Petroleum and Natural Gas Engineering
George E. Trimble Chair in Earth and Mineral Sciences
Graduate Program Chair of Petroleum and Natural Gas Engineering

Derek Elsworth
Professor of Energy and Geo-Environmental Engineering

Chris J. Marone
Professor of Geosciences

*Signatures are on file in the Graduate School.

ABSTRACT

Understanding fracture morphology in terms of a porous media is necessary for accurate simulation of multiphase transport in fractured rocks. Although ambient-stress methods for obtaining fracture morphology exist, previous research lacks the ability to map fracture closure as a function of stress or the distribution of immiscible phases in the fracture. This study focuses on the mechanical and hydraulic behaviors of fractures under multiphase flow at different confining stress.

A twenty-five-millimeter cylindrical sandstone samples were artificially fractured in tension and placed under confining stress in an x-ray transparent vessel. The fracture morphology was characterized under dry conditions and at different confining stress using high-resolution x-ray computed tomography. Multi-phase fluid distributions in the fracture were mapped between limits of the mobile saturation range using controlled fractional flows. These distributions were correlated with flow rate and pressure drop measurements. We observed order of magnitude differences in effective permeabilities under conditions of nearly constant overall fracture saturations. These differences in permeability are associated with re-arrangement of the physical distribution of the phases. Distributions associated with low permeability are unstable on a time frame of several hours, much longer of the time frame associated with snap-off phenomena. This phenomenon may be responsible for similar field observations reported in the literature.

TABLE OF CONTENTS

	<u>page</u>
LIST OF FIGURES.....	vi
LIST OF TABLES.....	xiii
ACKNOWLEDGMENTS.....	xiv
CHAPTER 1. INTRODUCTION.....	1
CHAPTER 2. LITERATURE REVIEW.....	3
CHAPTER 3. OBJECTIVE AND APPROACH.....	11
CHAPTER 4. EXPERIMENTAL METHOD AND PROCEDURES.....	12
4.1 Computed Tomography.....	12
4.2 Materials.....	13
4.2.1 Rock samples.....	13
4.2.2 Fluids.....	13
4.3 Fracture preparation.....	14
4.4 Flow distributor system.....	18
4.5 Core holders.....	18
4.6 Injection pumps.....	21
4.7 System.....	22
4.8 MCT (OMNI-X) unit.....	24

CHAPTER 5. EXPERIMENTAL RESULTS.....	25
5.1 Mineral characterization of Berea Sandstone.....	25
5.2 Fracture characterization.....	31
5.2.1 Structure Model Index (SMI).....	50
5.2.2 Connectivity density coefficient (EPC).....	52
5.3 Fluid flow experiments.....	62
5.3.1 Core #1	64
5.3.2 Core #2	67
5.3.3 Core #3	69
5.3.4 Core #4	71
5.4 Multi-phase flow injection with CT data.....	72
5.4.1 Fractional flow	81
5.4.2 Confining pressure from 500 to 2500 psig.....	96
CHAPTER 6. CONCLUSIONS	107
REFERENCES.....	110

LIST OF FIGURES

	<u>page</u>
Figure 4.1: Drilling and machining process for a two inch diameter cores.	14
Figure 4.2: Application of the modified Brazilian test to create a single extensional fracture. Core length was 140 mm.....	15
Figure 4.3: Tensional fractures under modified Brazilian test (Machine 2).	16
Figure 4.4: Sub-drilling (left). One inch core after fracturing and sub-drilling (right).....	17
Figure 4.5: Cutting process of the cores (left). One inch core after fracturing and resizing (center and right).....	17
Figure 4.6: Core holder end-plugs. Left: Injection. Right: Outlet.....	18
Figure 4.7: Aluminum core holder sleeve used in one of the experiments.	19
Figure 4.8: Carbon composite core holder sleeve used in the final experiments.....	20
Figure 4.9: Two-phase injection pump system.....	21
Figure 4.10: Schematic diagram of the fluid flow system.....	22
Figure 4.11: HD-600 OMNI-X high resolution MCT unit.....	24
Figure 5.1: Scanning Electromagnetic System (SEM) system.....	26
Figure 5.2: Berea Sandstone. Image of a region of 7 mm-square.....	27
Figure 5.3: Berea sandstone image, 0.1mm-square.....	28

Figure 5.4:	Increased magnification SEM image showing kaolinite clay...	29
Figure 5.5:	Mineral composition of section E marked on Figure 5.4.....	30
Figure 5.6:	A single CT slice at various stages of processing. a: original. b :rotated. c: cut and masked.....	31
Figure 5.7:	: Original core before and after scanning and extracting a region that contains the fracture.....	32
Figure 5.8:	CT image at the same location for increasing confining pressure Slice 140.....	33
Figure 5.9:	Aperture profiles as a function of confining pressure at the same location in the sample.....	34
Figure 5.10	Aperture fracture map for 100, 500 1000 1500 2000 and 2500 psig confining pressure.....	35
Figure 5.11:	a: CT profile at x = 140 b: images for 100 and 2500 psig confining pressure c: CT profile at x = 660.....	37
Figure 5.12:	CT profiles at different locations (100 psig and 2500 psig confining pressure).....	38
Figure 5.13:	Fracture aperture surrounded by matrix.....	39
Figure 5.14:	Three-dimensional images of the fracture under 100 and 2500 psig confining pressures.....	40
Figure 5.15:	Fracture aperture volume with coronal slice planes.....	41

Figure 5.16:	Cartoon of the three-dimensional (binary) fracture aperture array.....	41
Figure 5.17:	Two dimensional fracture aperture maps. a: 100 psig. b: 2500 psig.....	42
Figure 5.18:	Two dimensional asperities maps.....	44
Figure 5.19:	Probability plot from the fracture aperture.....	45
Figure 5.20:	Fracture aperture distribution (2500 psig).....	46
Figure 5.21:	Fracture aperture distributions for 100 and 2500 psig.....	46
Figure 5.22:	Figure 5.22: Fracture aperture distribution (2500 psig).....	48
Figure 5.23	Fracture aperture distribution 360 microns thickness or more...	49
Figure 5.24:	Changes in pressure drop for different confining pressure at fixed injection rate.....	52
Figure 5.25:	Pressure drop in the fracture for different fractional flow values.....	53
Figure 5.26	Pressure drop in the fracture vs fractional flow, 1000 psig confining pressure.....	55
Figure 5.27:	Pressure drop in the fracture vs fractional flow for 800 and 1000 psig.....	56
Figure 5.28	Pressure drop in the fracture vs fractional flow for 200 psig. Set # 1.....	57

Figure 5.29	SMI distribution for the 16x16 case at 2500 psig. The width is 3.120 mm and the length is 3.968 mm.....	58
Figure 5.30:	EPC distribution for the 2x2, 4x4, 8x8 and 16x16 case at 2500 psig.....	59
Figure 5.31:	EPC average values for the 2x2, 4x4, 8x8 and 16x16 case at 500 and 2500 psig.....	60
Figure 5.32:	SMI average values for the 2x2, 4x4, 8x8 and 16x16 case at 500 and 2500 psig.....	61
Figure 5.33	Changes along pressure drop for different confining pressure at fixed injection rate.....	64
Figure 5.34	Pressure drop along the fracture for different fractional flow values.....	65
Figure 5.35	Pressure drop along the fracture vs fractional flow, 1000 psig confining pressure.....	66
Figure 5.36:	Pressure drop in the fracture vs fractional flow for 800 and 1000 psig.....	67
Figure 5.37:	Pressure drop in the fracture vs fractional flow for 200 psig. Set # 1.....	68
Figure 5.38:	Pressure drop in the fracture vs fractional flow for 200 psig. Set # 2.....	68
Figure 5.39:	Pressure drop in the fracture vs fractional flow for a confining pressure equal to 800 psig.....	69

Figure 5.40:	Fractional flow range: 0.25-0.50. 800 psig confining pressure.	70
Figure 5.41:	Fractional flow range: 0.50-0.83. 800 psig confining pressure.	70
Figure 5.42:	Pressure drop in the fracture vs fractional flow for 500 psig.	
	Core # 4.....	71
Figure 5.43:	Fractured core (top), matrix reduction (bottom).....	72
Figure 5.44:	Pressure drop in the fracture for water injection.....	73
Figure 5.45:	Water pressure drop in the fracture for different saturation conditions.....	75
Figure 5.46:	Relative permeabilities curve for a fractured system at 500 psig.....	76
Figure 5.47:	Fracture volume for different threshold numbers.....	77
Figure 5.48:	Three dimensional rendition of fracture asperities.....	78
Figure 5.49:	Fluids distribution maps: a: dry. b: oil. c: water at residual water saturation state.....	79
Figure 5.50:	Fluids distribution maps: a: dry. b: Residual oil. c: Water	80
Figure 5.51:	Pressure drop as function of fractional flow: two drainage and imbibitions cycles.....	81
Figure 5.52:	Pressure drop in the fracture for different fractional flow. q_{total} $= 12 \text{ cc/min}$	82
Figure 5.53	Fluids distribution in the fracture at low pressure drop. a: Oil b: water.....	83

Figure 5.54	Oil saturation profile for the low pressure drop condition (left).Three-dimensional distribution of oil in the fracture (right).....	85
Figure 5.55:	Disconnected oil globules in the fracture at low pressure drop condition.....	86
Figure 5.56:	Oil feed distribution at low pressure drop.....	87
Figure 5.57:	Fracture pressure drop during different fractional flows including a spontaneous pressure change.....	88
Figure 5.58:	Oil saturation profile for the high pressure drop condition (left).Three-dimensional distribution of oil in the fracture (right).....	90
Figure 5.59:	Oil distribution in the fracture. Left: Low pressure drop. Right: high pressure drop.....	92
Figure 5.60:	Oil distribution low pressure drop (a). Oil distribution high pressure drop (b).....	93
Figure 5.61:	Pressure drop as a function of flow rate for a non-fractured and a fractured core.....	94
Figure 5.62:	Schematic of the volume changes with confining pressure.....	96
Figure 5.63:	CT profile in the matrix area near the fracture (Dry and Wet)...	98
Figure 5.64:	CT profile in the matrix area near the fracture at 500 and 2500 psig.....	99
Figure 5.65:	Residual oil saturation map at 2500 psig.....	101

Figure 5.66:	Pressure drop in the fracture at 2500 psig for a total liquid flow rate of 1cc/min.....	102
Figure 5.67:	Changes in CT average (2500 psig) after injecting alcohol and vacuum drying of sample.....	103
Figure 5.68:	Three-dimensional recreation of the fracture at 500 (left) and 2500 (right) psig.....	105
Figure 5.69:	Thickness aperture map of the fracture at 500 (left) and 2500 (right) psig.....	106

LIST OF TABLES

	page
Table 5.1: Roughness factor values.....	47
Table 5.2: SMI parameters for 500 and 2500 psig.....	51
Table 5.3: Summary of the segmentation process and block dimensions.....	54
Table 5.4: Summary of SMI and Euler-Poincaré values (Averages).....	54
Table 5.5: Liquid flow rates and Fractional flow.....	63
Table 5.6: Fluid fracture saturation comparison at high and low pressure	91
Table 5.7: Volume change with confining pressure. Before and after P_c changes.....	97
Table 5.8: Fracture fluids saturation before and after changes in P_c	100
Table 5.9: Residual oil saturation and mobile at 500 and 2500 psig.....	100

ACKNOWLEDGMENTS

I would like to thank Dr. Grader and Dr. Halleck for their support and contribution to this research.

I want to express my sincere gratitude to my mom and my father, who day by day made sacrifices to give me the best of them; you are present in all my days.

To my wife Lissett for all the love and support during my studies but especially during this project, this is also yours. To Nicole, a new light in our hearts, you have changed our lives. We will love you for ever. To my brothers, Mario and Meiling, for being so special. Finally, I will thank all my friends for their support and words during this journey.

As I always say,

“If there is a will, there is a way...”

CHAPTER 1

INTRODUCTION

Two-phase flow in fractured systems is a common phenomenon in hydrocarbon reservoirs. Oil and water are the most common phases in this type of reservoirs. However, it is also possible to find gas-liquid systems where two phase flow occurs. This study uses Micro Computed Tomography (MCT) for analyzing two phase flow behavior in tensile fractures under confining pressure and different fractional flow conditions.

Previous work on flow transport, Witherspoon *et al.* (1980), used a parallel plate approximation for studying fracture flow. They found that the cubic expression, known as the cubic law, appeared to be suitable for a tight fracture under stress. However, more recent studies have questioned the validity of this cubic law given the complex geometry of fractures. The surface roughness and fracture aperture distributions play a key role in the conductivity of the fracture and its mechanical behavior during the changes in confining pressure. Previous attempts to describe fracture apertures and fluid distribution have failed as a consequence of the heterogeneities of the porous media. Therefore, early investigations have reported the lack of fracture characterization for modeling fluid flow through fractures.

MCT provides an innovative technique to characterize the fracture and to map the fluid phases present in the fracture with high spatial resolution. In this research, two major areas were investigated by experimental work: one focused in the interaction and occupancy of the fluids in the fracture, and the other focused on the mechanical behavior of the fracture and its impact on flow properties. The main goals of this study are to correlate multiphase flow behavior in the fracture with changes in fractional flow and confining stress.

CHAPTER 2

LITERATURE REVIEW

Multiphase flow in fractures is an important phenomenon that has been studied in different fields such as oil industry, nuclear engineering, ground water hydrology, and geothermal industry. However, there is still a lack of understanding of the mechanical and hydraulic response of fractures including fluid interactions and fluids occupancies in the fractures. In oil reservoirs, as production declines, the net confining pressure increases, affecting the fracture topology, (aperture, porosity, surface roughness and tortuosity) and therefore the multiphase transport characteristics, Barton *et al.* (1985), Gentier *et al.* (1986). Gray *et al.* (1963) did experimental work to prove that the permeability of sandstones is a function of the overburden pressure. The apparatus was designed to use cores between two and three inches diameter with a maximum of 5000 psig loading. They observed that under non-uniform stress the reduction of permeability was lower than under uniform stress. They also concluded that the maximum reduction in permeability occurred under hydrostatic loading (uniform).

In early investigations, the flow through fractures was simulated by using two parallel glass plates. Lomize (1951) and Louis (1969), who performed such experiments, are recognized as the fathers of the well known cubic law.

This law relates flow rates, hydraulic head and fracture aperture. However, it does not take into account the rugosity of the fractures. Iwai (1976) created artificial fractures, in an attempt to include contact point areas and fracture roughness. He loaded the system with normal stress and found that large contact areas (small apertures) compromise the validity of the cubic law.

Witherspoon *et al.* (1980) present a study of the validity of the cubic law for fluid under fractured samples. They used different rock samples, fracturing them with a modified Brazilian test. The results that they obtained showed that the cubic law was valid for the cases that they ran. The only deviation from the parallel plate model that they reported was due to the reduction in flow. They took into account such deviation by defining an f factor that varied from 1.04 to 1.65.

Neuzil *et al.* (1981) presented an alternative fracture flow model. The model accounted for aperture variations (normal to the flow) that lead to a modified Poiseuille's equation. They concluded that more experimental data were needed to provide a solid base of the fracture flow theory. Four years later, Tsang (1984) presented an investigation that related the tortuosity effect through a single fracture. She proved that the experimental flow rates were smaller than the ones predicted by the cubic law. He claimed that such deviations were a consequence of tortuosity present in the fracture and not taken into account in the parallel plate model.

Raven *et al.* (1985) performed a flow experiment to evaluate water flow behavior in a natural fracture as a function of stress and sample size. They found that the impedance decreased with the increasing in sample size and with each additional loading cycle. The fracture aperture showed different paths for the loading and unloading processes, such a difference in path is called hysteresis, and was confirmed by Barton *et al.* (1985) with the application of normal loads. The larger samples showed more asperities in contact and therefore lower contact point stresses and more tortuous flow channels. To compute the fracture aperture Schrauf *et al.* (1986) injected gas in a single fracture. This technique was based on Bolyes' law. However, given the small volume of the gas in the fracture, the calculations of the fracture aperture were very difficult and not accurate.

Tsang *et al.* (1987) in an attempt to gain a better understanding of the flow in fractures described the flow channels by using an aperture density distribution function and a spatial correlation length. They used at log-normal function of the fracture aperture for determining the relationship between flow and transport measurements of variable apertures. Although this conceptual model failed to reproduce experimental data, it emphasized the need for a better characterization of the fractures. One year later, Chen *et al.* (1989) presented a theoretical model for analyzing the effect of the contact area on the permeability of the fracture. They considered an idealized fracture consisting of two parallel plates propped by isolated asperities.

The numerical and analytical results were in agreement with the experimental results obtained by Walsh (1981). Although this study presented valuable information on the effect of the contact area on the fracture permeability, its basic assumption, the parallel plate model, constituted an impractical approach for characterizing the effect of the tortuosity induced by the contact areas.

Pyrak-Nolte *et al.* (1990) performed a percolation model to analyze fluid flow through single fractures. They simulated experimentally-observed flow path geometries. From the analysis of unsaturated fluid flow in fractures, they concluded that the non-wetting phase permeability decreases rapidly with increasing wetting phase saturation. It was also observed that the cross-over in permeability of the wetting and non-wetting phases is essentially invariant with stress. This led to the important conclusion that if the percentage of one of the phases is known, one can determine which phase dominates the flow at any stress.

At the beginning of the 90's a group of researchers focused their attention not only looking at the mechanical but also at the fracture hydraulic behavior, in an attempt to expand the boundary of knowledge of the behavior of two-phase flow in fractures.

Horie *et al.* (1990) presented experimental and theoretical models that incorporated the capillary-continuity concept for dual-porosity models. They ran three different scenarios;

the first one considered zero capillary pressure in the fracture, the second one was based on a relationship between the capillary pressure and the distance between two parallel plates and, the last model assumed that the fracture capillary pressure curve had a shape similar to that of the porous media but with major difference in curvatures. The experimental work performed showed no agreement with the firsts two models, and the simulation results indicated (sensitivity study) that the fracture capillary pressure might have a functional form similar to that of a matrix.

Babadagli *et al.* (1992), conducted experimental work and coupled it with numerical modeling. They studied the imbibition-assisted two-phase flow in natural fractures. They observed that the composite-system relative permeability curves were strong functions of flow rate, flow direction, matrix permeability, wettability, matrix saturation (initial) and fracture shape. Trying to validate the X-shaped relative permeability curves for fractures, Persoff *et al.* (1985) conducted two-phase flow experiments using transparent replicas of natural fractures. Once again, they found deviations from the X-shapes relative permeabilities curves used for fractures (no phase interference).

Keller (1996) performed X-ray (CT) experiments using three samples of fractured Berea Sandstone. From CT core characterization he found that log-normal distribution was adequate for the fracture aperture. Using a similar approach, Pyrak-Nolte *et al.* (1997) compared the aperture porosity and distribution of the entire fracture network. They combined medial CT imaging and wood metal injection for analyzing the persistence of

fracture network porosity and fracture aperture over cores containing natural fracture networks. They proved that the two-dimensional modeling of fluid flow through fractures must consider that the fracture geometry can change in the axial direction. Two years later, Montemagno *et al.* (1999) suggested, based on experimental work, that fracture intersections may be preferentially connected and correlated over distances in the main direction of flow.

The mechanical and hydraulic (single phase) behaviors of the fractures are related to the changes of flow paths. Walter *et al.* (1999) investigated the effect of a variable-aperture system in an oil sand fracture. They analyzed the hydraulic and mechanical fracture response due to changes in confining pressure. One more time, the flow test experiments showed deviation from the cubic law (nonlinear behavior), indicating the roughness effect and therefore a strong relationship between the hydraulic and the mechanical behavior, Raven and Gale (1985).

One important technology used to validate fluid flow model is the X-ray computerized tomography. Alajmi *et al.* (2000) investigated the interaction between an induced fracture and the surrounding matrix. They used CT scans to quantify the fluid saturations at different stages of the flow injection in a partially fractured core (Berea sandstone). They found a strong effect of fracture capillary pressure on simulations that matched their experimental results.

Different fluid flow behaviors were observed in the core at different locations (fracture region, tip of the fracture, non-fracture region) showing the importance of the interaction between fracture/matrix and matrix/fracture. Two year later, Durham *et al.* (2001) carried out experimental work to examine the relationship between local rate of dissolution and local aperture during flow of a slightly acid aqueous solution through a fracture. They recognized the advantage of the CT scans to analyze the fluid flow through fractures. However, they pointed to a lack of spatial resolution (1 mm maximum voxel resolution) obtained by CT (medical scanner) at the moment of their work. The experimental work was done using digital reconstruction of the fracture aperture before and after the injection of the flow tests. They found that the dissolution process resulted in the displacement of the two rock halves, decreasing the overall fracture permeability. However, they were not able to explain the inverse relationship between the magnitude of the fluid flux and the rate of dissolution.

The literature review presents most of the relevant work (experimental and theoretical) presented in the study of the mechanical and hydraulic behavior of fractures. Most of the mechanical studies of fractures have been performed under single phase flow, not considering the fracture-phase flow interaction. The characterization of the fracture aperture changes has been performed using two methods, destructive and nondestructive.

The destructive methods include: injection methods [Tsang and Tsang (1987)], the surface topography method [Gentier and Hopkins (1986)], and the casting method [Yeo *et al.* (1998)]. The nondestructive methods are: magnetic resonance and absorbance intensity of x-ray. Micro Computed Technology (MCT) presents an advantage over the magnetic resonance, since MCT allows in-situ injection of fluids into the samples, at high resolution, and the ability to obtain three-dimensional maps of a multi-phase system. Alvarado *et al.* (2004).

The literature review highlights the need for a better fracture characterization and multiphase behavior in order to enhance the understanding of fluid flow through fractures. Previous attempts to find an accurate characterization of fracture apertures have failed as a consequence of the lack of available technology. This study uses state of the art Micro Computed Tomography for characterizing fracture apertures at high spatial resolution and to map and correlate the multiphase flow behavior under the effect of changes in confining pressure and fractional flow.

CHAPTER 3

OBJECTIVES AND APPROACH

Hypotheses:

- Fluid distribution during multiphase flow in fracture affects the conductivity of the fracture.
- Changes in confining pressure modified the topology of the fracture and therefore the fluid saturation on the fracture.

Approach:

- To use a micro computed tomography technique for acquiring images of two fluid phases in the fracture.
 - Different fractional flows
 - Different confining pressures
- To monitor the fracture flow changes through pressure drop, confining pressure, temperature and flow rate changes.
- To develop procedures for computing the fracture characterization through fracture aperture, asperities distribution, maps of flow channels, and multi-phase flow occupancy.
- To develop procedures for determining three-dimensional maps of two-phase saturation distributions in the fracture from volumetric computed tomography data.

CHAPTER 4

EXPERIMENTAL METHOD AND PROCEDURES

In this chapter experimental method and procedures are described.

4.1 Computed Tomography

X-ray Computed Tomography is a non-destructive technique for mapping the internal distribution of the density and atomic numbers of an object. It was originally developed in Great Britain in 1972 primary for medical purposes. This technique is used today in industrial application under the category of non-destructive evaluation, NDE. Computed Tomography has been used in the oil industry since 1980's [Wang *et al.* (1984), Wellington *et al.* (1987), Hicks *et al.* (1992), Grader *et al.* (1998)]. Computed Tomography has been used to study fluid flow in rock samples, for detailed characterization, and for screening cores. This technique is based on the attenuation of X-ray as they pass through a sample. X-ray sources are made in a range of acceleration voltages and applied currents. The penetration ability of x-rays depends on the voltage, and the current defines how many protons are generated at a specific voltage.

Small focal spots at the x-ray sources provide better resolution. However, it is difficult to make high voltage and high current x-rays to emit from a small focal spot. In this study, we used a micro-focus x-ray source at 160 KV and 500 μ A with a focal spot about 5 microns theoretically. This allows us to generated resolutions of about 30 microns, a resolution sufficient for imaging fractures in the Berea sample used in the experiments.

4.2 Materials

4.2.1 Rock samples

The rock samples used are Berea sandstone fractured cores. The average permeability (prior fracturing) is about 100 mD. The bedding planes are perpendicular or parallel to the tensile fracture. Different orientations will be used depending on the experiment.

4.2.2 Fluids

The two fluids used for this experiment are water tagged with KCl or NaI (7%) and Kerosene. The immiscibility of the two fluids resembles the interaction of the fluids present in the reservoir. These two fluids also provide a clear contrast in x-rays attenuation, allowing the partitioning of the phases in the fracture.

4.3 Fracture preparation

The first step of the core preparation was to cut several two-inch diameter samples. Cores parallel and perpendicular to bedding planes were cut. Figure 4.1 (a) shows the drilling process of two-inch cores. These cores were machined to precision cylinders so that they can break uniformly when they are subject to uniform stress for creating tensional fractures. Figure 4.1 (b) and (c), show the machining process of two inch cores.

(a)



(b)



(c)

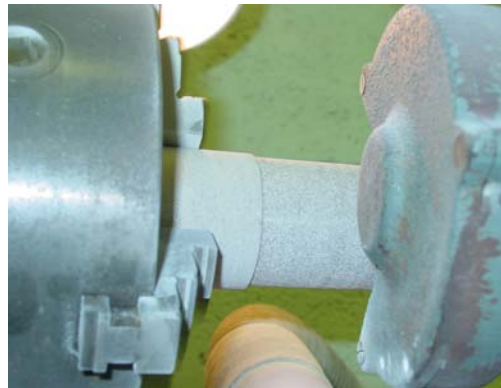


Figure 4.1: Drilling and machining process for a two inch diameter cores.

After machining, a modified Brazilian test was used to create a single extensional fracture. Figure 4.2 shows one of the cores during the fracturing process.



Figure 4.2: Application of the modified Brazilian test to create a single extensional fracture. Core length was 140 mm.

Figure 4.2 shows a core before and after fracturing. A force of 9,000 pounds (force) was applied to the core before creating the tensile fracture.

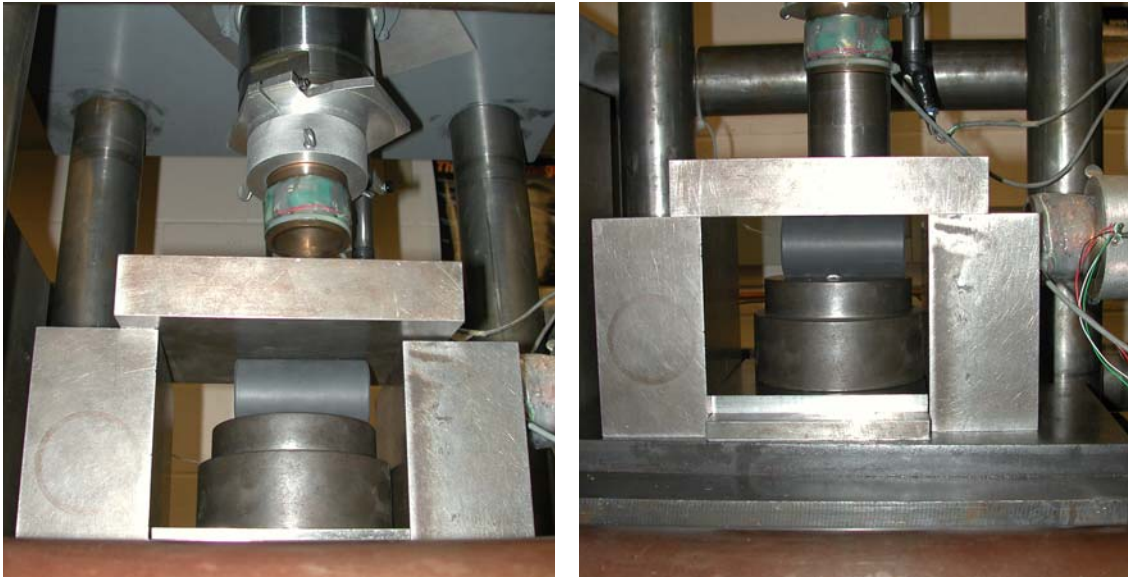


Figure 4.3: Tensional fractures under modified Brazilian test (Machine 2).

Figure 4.3 presents a two-inch sandstone core during the fracturing process in a second machine different from the one displayed in Figure 4.2. This second machine (Figure 4.3) has more control over the vertical displacement, helping the process of fracturing, especially after the core failure, resulting in a better tensional fracture and preserving the entire core.

After creating the tensional fracture, the core was drilled to a 1 inch diameter, preserving the fracture along the length of the core. Figure 4.4 (left) shows the over drilling process while Figure 4.4 (right) presents the resulting one inch core. This cutting process must be

done in order to avoid deformation (boundary) that may create a wedge along the external edge of the fracture.



Figure 4.4: Sub-drilling (left). One inch core after fracturing and sub-drilling (right).

The final step before having the cores ready for the experiments consists of cutting and squaring all the edges of the cores. Figure 4.5 shows the one-inch core in the final phase of the core preparation process.



Figure 4.5: Cutting process of the cores (left). One inch core after fracturing and resizing (center and right).

4.4 Flow distributor system

An end-plug flow distributor was designed in order to allow the injection of two phases into a tensile fracture. This end-plug will achieve a better injection of the fluids into the fracture and will also allow the measurement of the pressure drop along the fracture. Figure 4.6 shows the end-plug. The pressure and the fluid ports can be observed in Figure 4.6 (left).



Figure 4.6: Core holder end-plugs. Left: Inlet. Right: Outlet.

4.5 Core holders

A plastic core holder was used for preliminary flow experiments with low confining pressure. For cases of high confining pressure (higher than 200 psig) an Aluminum core holder was used in the preliminary experiments.

A maximum of 3000 psig can be reached with this core holder (at 100 C). The maximum confining pressure applied to the core during the fracture closure analysis was 2500 psig. Figure 4.7 shows the aluminum core holder standing vertically.



Figure 4.7: Aluminum core holder sleeve used in one of the experiments.

In order to minimize the attenuation of the x-rays by the aluminum core holder, a composite fiber carbon core holder was designed and used for the final experiments at high confining pressure (2500 psig). Figure 4.8 shows a photograph of the one-inch carbon composite core holder. The working pressure for this core holder was 3000 psig at 100 C. The low x-ray resistance of this type of core holder improves signal to noise ratios and results in superior three-dimensional CT data that are the basis of determining fluids distribution in the fracture.



Figure 4.8: Carbon composite core holder sleeve used in the final experiments.

4.6 Injection pumps

For the injection of the two phases a Quizix SP-5400 pump system was used (2 subsystems, two cylinders per single phase flow). The pump system provides continuous, pulse-free fluid flow even for a high pressure. This pumps system (SP-5400) has high accuracy for fluid flow rates (Figure 4.9). The SP-5400 system provides volume resolution of less than one-tenth of a nanoliter (0.000001 ml) per motor step, and is designed for applications requiring ultra-low flow rates.

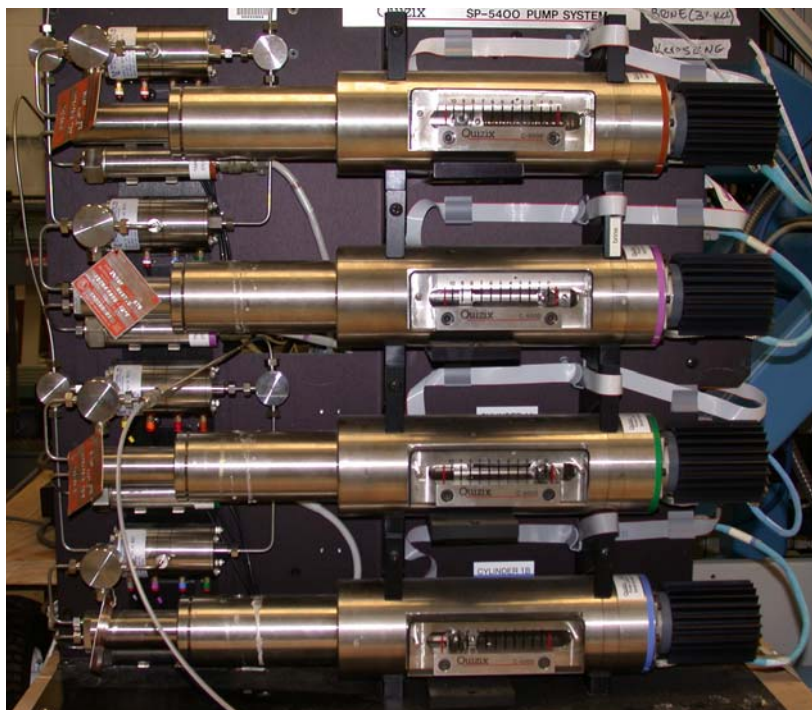


Figure 4.9: Two-phase injection pump system.

4.7 System

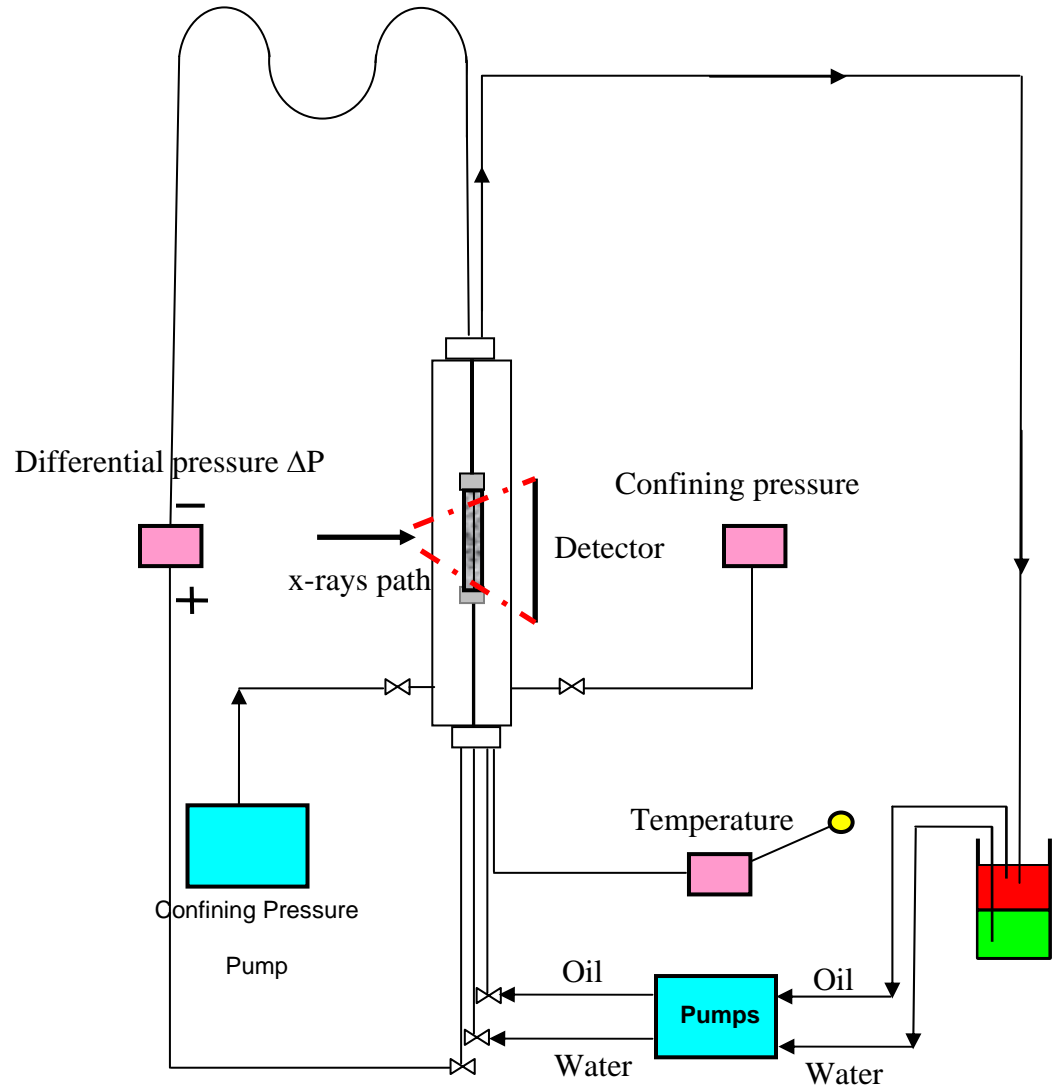


Figure 4.10: Schematic diagram of the fluid flow system.

Figure 4.10 shows the fluid flow system. Differential pressure, 0-18 psi range, confining pressure 0-2500 range, flow rates 0-14 cc/min range, and temperatures, fluid and room temperatures are the parameters that are measured during flow experiments.

4.8. MCT (OMNI-X) unit

The industrial (OMNI-X) CT unit is a third generation scanner where the source and detector are fixed and the scanned object rotates. The system has a 225 KV micro-focus x-ray generator and a 225 mm diameter image intensifier. The micro-focus x-ray source allows high magnification by placing the object near the x-ray source.

The highest resolution that can be obtained by the micro-focus source is 5 microns. Once the object is brought to its position and the scanner is activated, the projections of the magnified object are captured by the image intensifier. When the MCT source is active, the x-ray energy travels through the object and reaches the image intensifier, which converts x-ray energy into a form of light that the digital video camera can record. The digitized data are sent to a computer and turned into raw files that can be processed into images.

High-resolution two-dimensional slices have 1024x1024 pixel elements, giving a total grid of 1,048,576 individual pixels per slice. The scanner can also produce reconstructed images with dimensions of 512x512 or 256x256 pixels. As the object rotates in the x-ray beam the detector records the attenuated signal periodically. These recordings are called views and the resulting records can be used to construct single or several slices in one rotation. When several images are reconstructed from one rotation, the system is in “volume mode” producing a volume representation of the sample.

In the work presented here 2400 views were collected for each 360 degree rotation. Precise movement and high-level magnification are essential for this study since fluid observation at the high magnification is required. Figure 4.11 shows a photograph of the x-ray OMNI-X CT unit system.

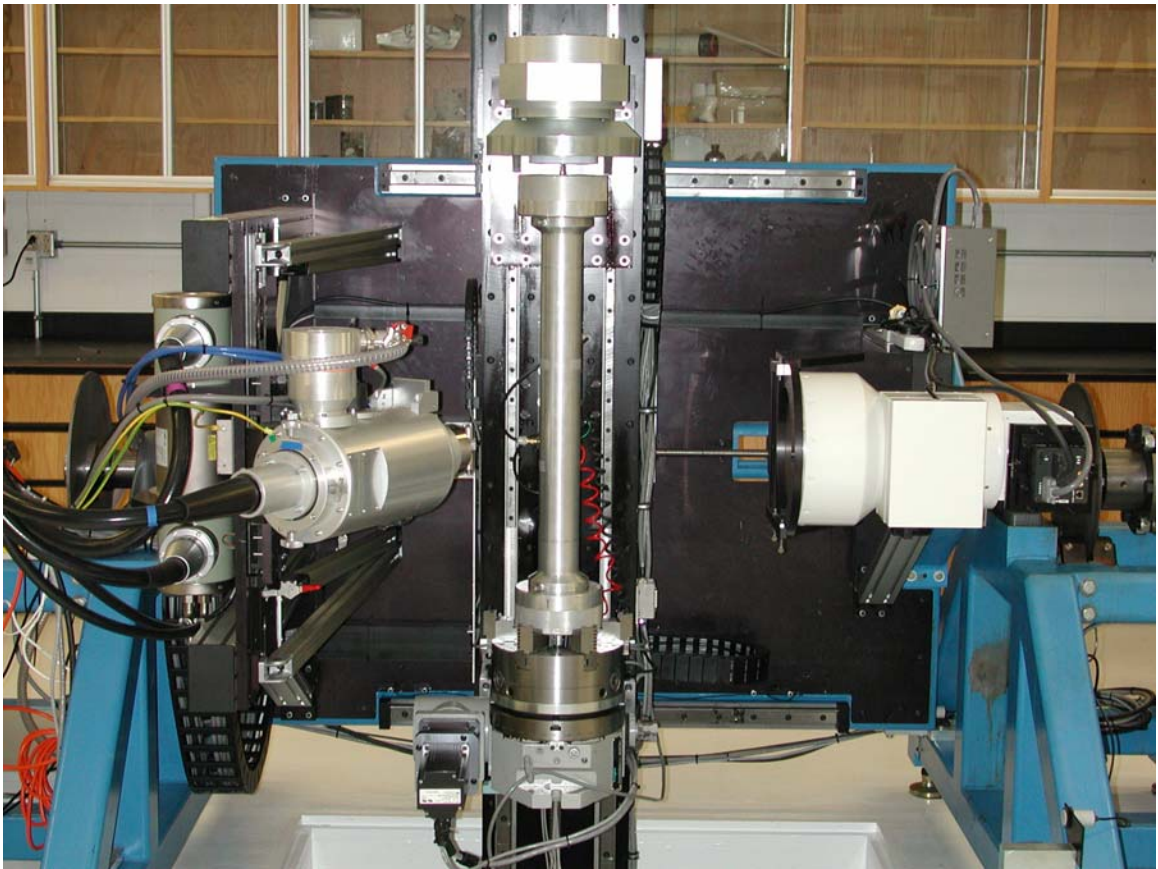


Figure 4.11: HD-600 OMNI-X high resolution MCT unit.

CHAPTER 5

EXPERIMENTAL RESULTS

5.1. Mineral characterization of the Berea Sandstone

The injection of fluid into a rock could cause dissolution or chemical reactions. These mechanical or chemical reactions could form new chemical components and they may have significant affects on the rocks properties, as porosity and permeability. Different cementing materials coexist in sandstone rocks the more common are: clay minerals including kaolinite, smectite and illite, carbonate (calcite and dolomite) and quartz (mainly in the form of overgrowths).

Reduction in permeability when salt water is replaced by fresh water has been reported in the literature, Khilar *et al.* (1987). The sensitivity of sandstone to fresh water is mainly due to the blocking of pore passages available for flow. A critical salt concentration, defined as the minimum salinity required for protecting the formation from swelling and mobilization of clays fines, has been reported in the literature and is mineral dependent. In order to characterize the rock samples an SEM analysis was perform. The main objective is to have a mineralogical study that helps to prepare fluids that preserve the core during the injection process.

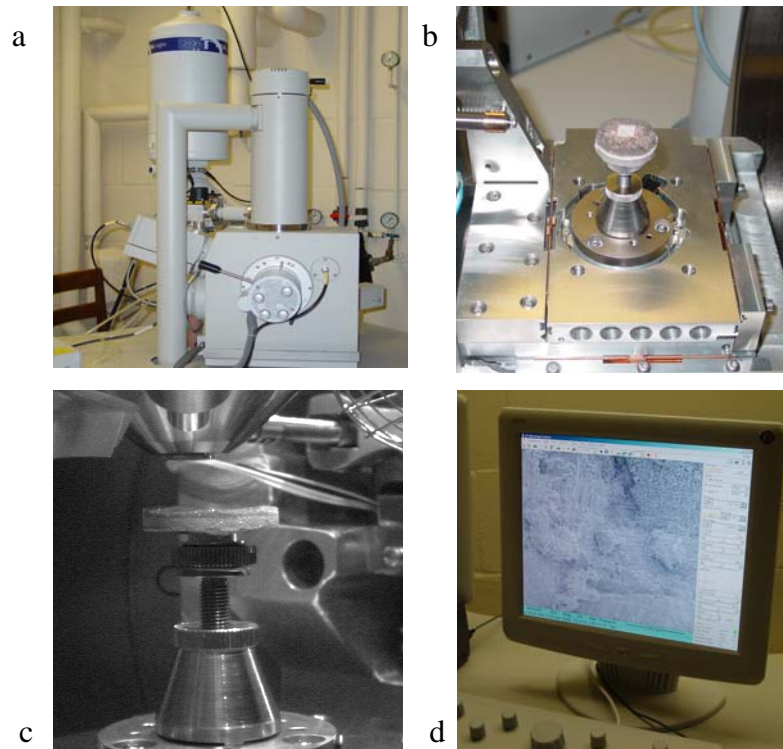


Figure 5.1: Scanning Electromagnetic System (SEM) system.

Figure 5.1a shows the gas chamber of the SEM system, different pressures can be used in order to obtain good quality images. Figure 5.1b shows a piece of Berea sandstone inside the chamber moments before scanning. Figure 5.1c shows the sample rock viewed from an internal camera. This camera is used to observe the movement of the sample in the vacuum chamber.

Figure 5.2 shows a small portion of the sample, 7 mm square approximately. Different minerals are present in the region. Quartz (silica), sodium (Na), calcium (Ca), and gold (Au) among others are observed from the graph (bottom). The presence of gold (Au) in the system is product of coating the sample before scanning.

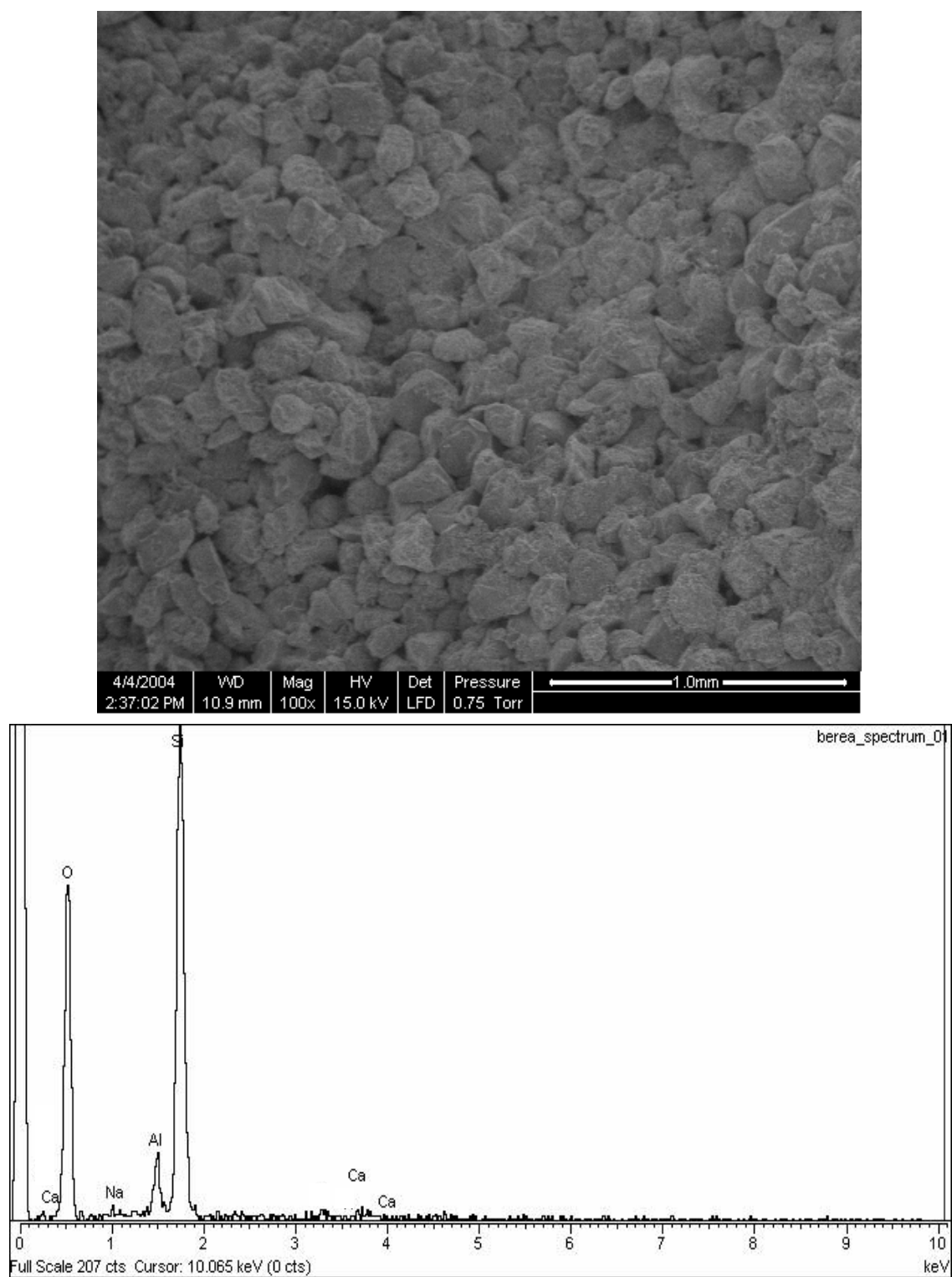


Figure 5.2: Berea Sandstone. Image of a region of 7 mm-square.

Si: Silica, Ca: Calcium, Na: Sodium, Al: Gold, and O: Oxygen.

Figure 5.3 (top) shows a typical quartz grain. The composition graph confirms the presence of silica. At this location other minerals were detected.

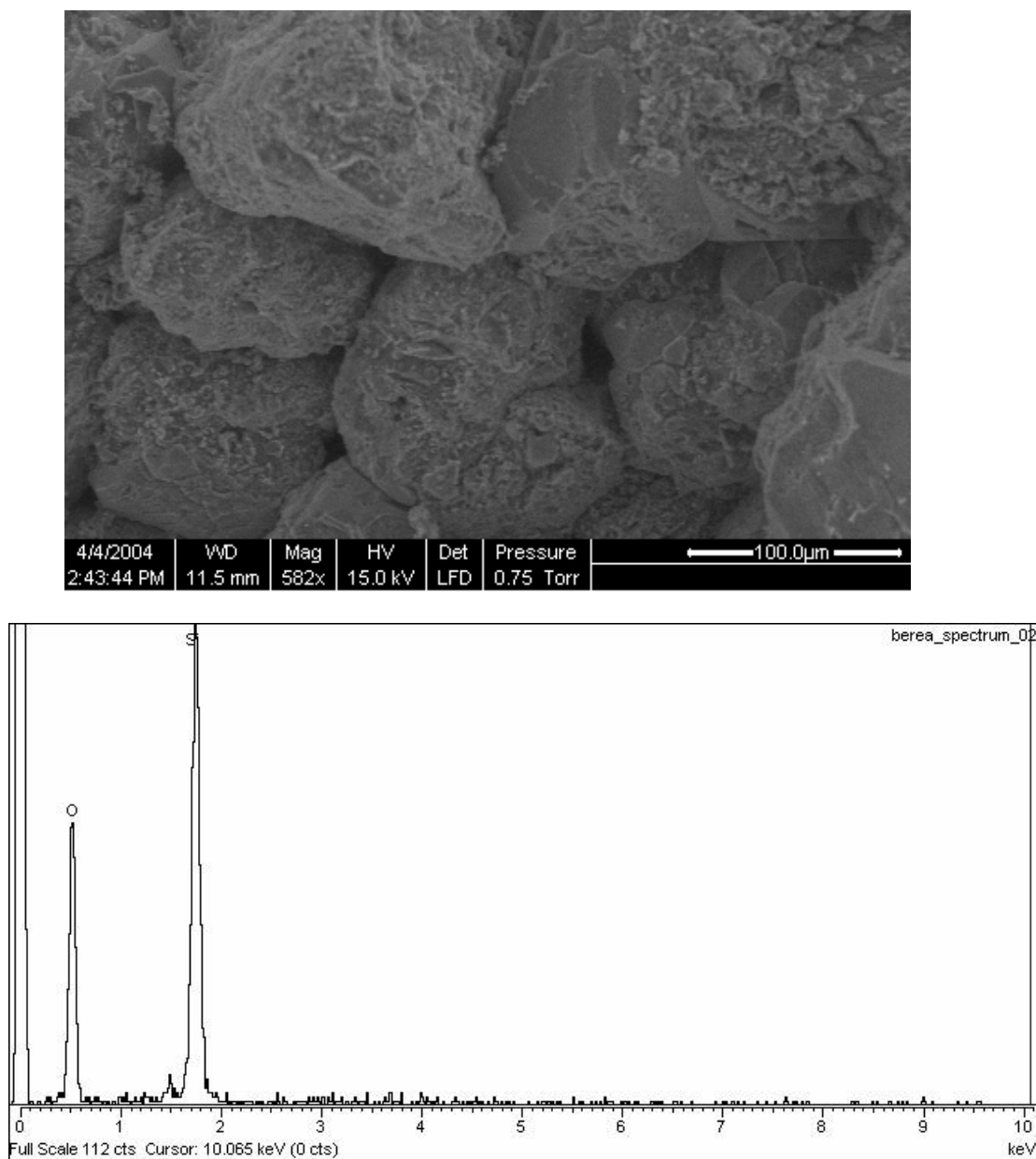


Figure 5.3: Berea sandstone image, 0.1mm-square.

Si: Silica, Ca: Calcium, Na: Sodium, Al: Gold, and O: Oxygen.

Figure 5.4 shows a possible clay (kaolinite) conglomerate, the right part of Figure 5.4 presents zooms of 100 and 50 microns.

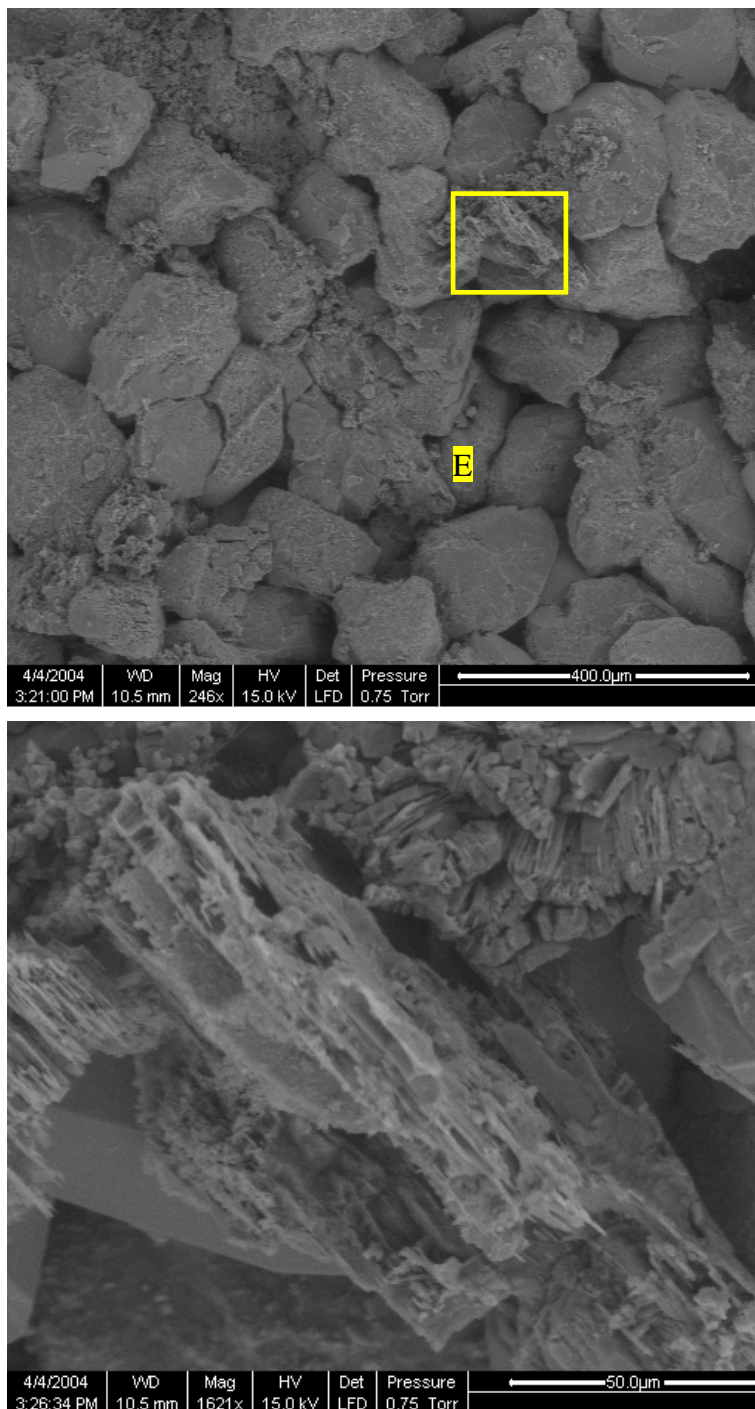


Figure 5.4: Increased magnification SEM image showing kaolinite clay.

A composition graph of Figure 5.4 is given in Figure 5.5.

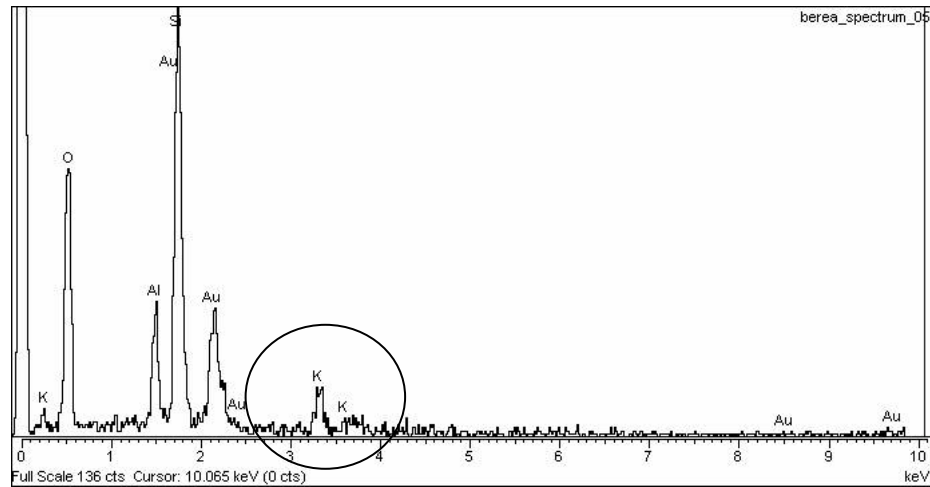


Figure 5.5: Mineral composition of section E marked on Figure 5.4.

After obtaining the compositional graph from region E, the presence of potassium is confirmed. This type of clay, usually called kaolinite, is one of the minerals responsible of reducing the permeability in the system when fresh water or brine with percentage lower than the critical salt concentration is injected into the system.

5.2 Fracture characterization

The scanned Berea sandstone cores had a diameter 25.0 mm and lengths between 64 mm and 70 mm. The core shown in Figure 5.6 was loaded into a core holder in a flexible sleeve with opposing shims of 0.4 mm, creating an axial shift. Then, the sample was placed into the scanner and 2250 slices were acquired covering the entire length of the sample. One of these slices is shown in Figure 5.6a. Once the slices were obtained they were rotated with an angle between 15 and 17 degrees. This rotation allows a better manipulation of the data in the x-y plane, Figure 5.6b. The slices were rotated during the sinogram reconstruction process, thus avoiding the introduction of any artifacts. After rotating the slices they were cut to eliminate the area beyond the edges of the core. The center of each image was identified and then, using the known radius the slices were cut, and all external pixels were arbitrarily changed to a fixed value (mask), Figure 5.6c. A final step consists in reducing the cut and masked images to a rectangular shape that contains only the fracture, eliminating most of the matrix region.

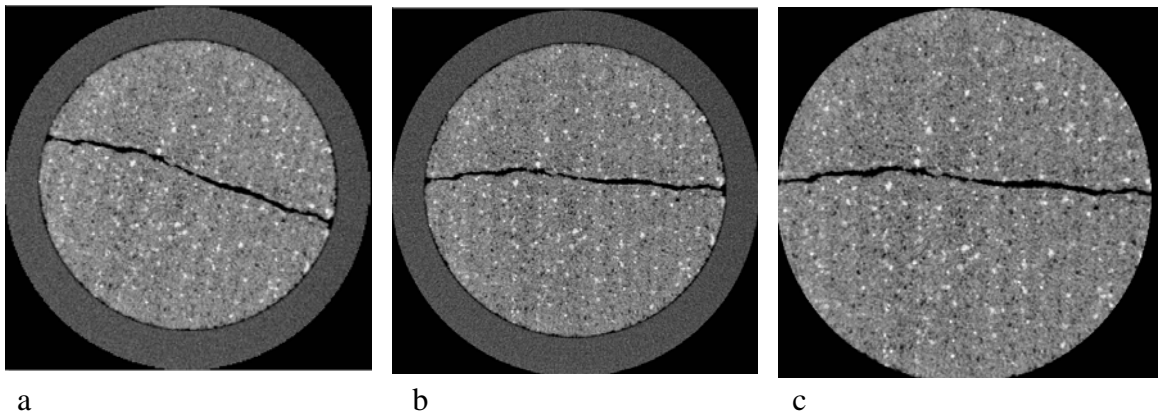


Figure 5.6: A single CT slice at various stages of processing. a: original. b: rotated. c: cut and masked.

The cropping process reduces the size of the images and makes all future manipulations more efficient than if the original size is used. For this study an original matrix of 1024x1024x410 (core BS1) or 1024x1024x2250 (core BS2) was reduced to a size of 800x100x410 and 850x120x2203 respectively. Figure 5.7 shows a photograph of the one inch core before scanning (left). The final rectangle (800x100) in photograph 5.7 (right) contains the extracted fracture.

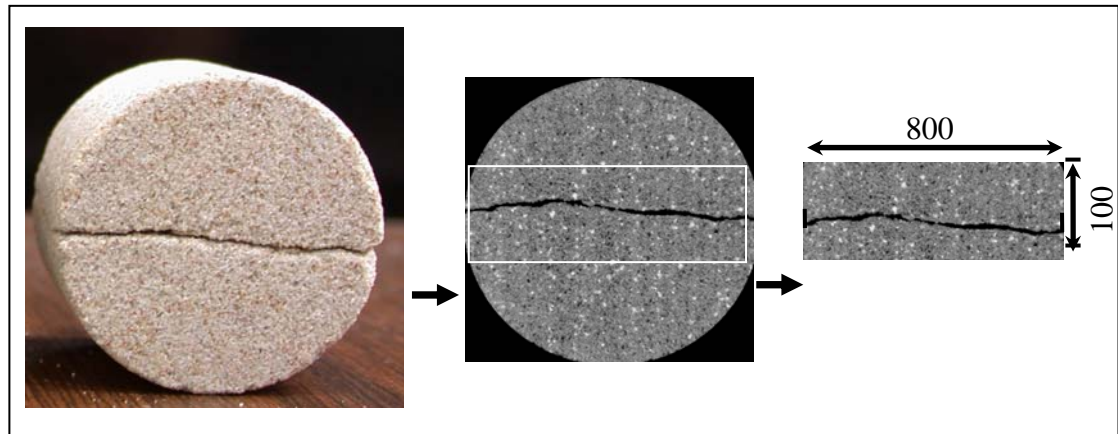


Figure 5.7: Original core before and after scanning and extracting a region that contains the fracture.

Figure 5.8 shows 6 stages of a preliminary experiment at a fixed location in the core. From left to right the confining pressure increases. The applied confining pressures are, 100, 500, 1000, 1500, 2000 and 2500 psig, reducing the fracture aperture. The white circles in Figure 5.8 highlight the formation of a new asperity (fracture aperture closure) during the increase in confining pressure from 100 to 2500 psig. This set of data (1024x1024) is the base for extracting the fracture in order to quantify the confining pressure stress effect in three dimensions.

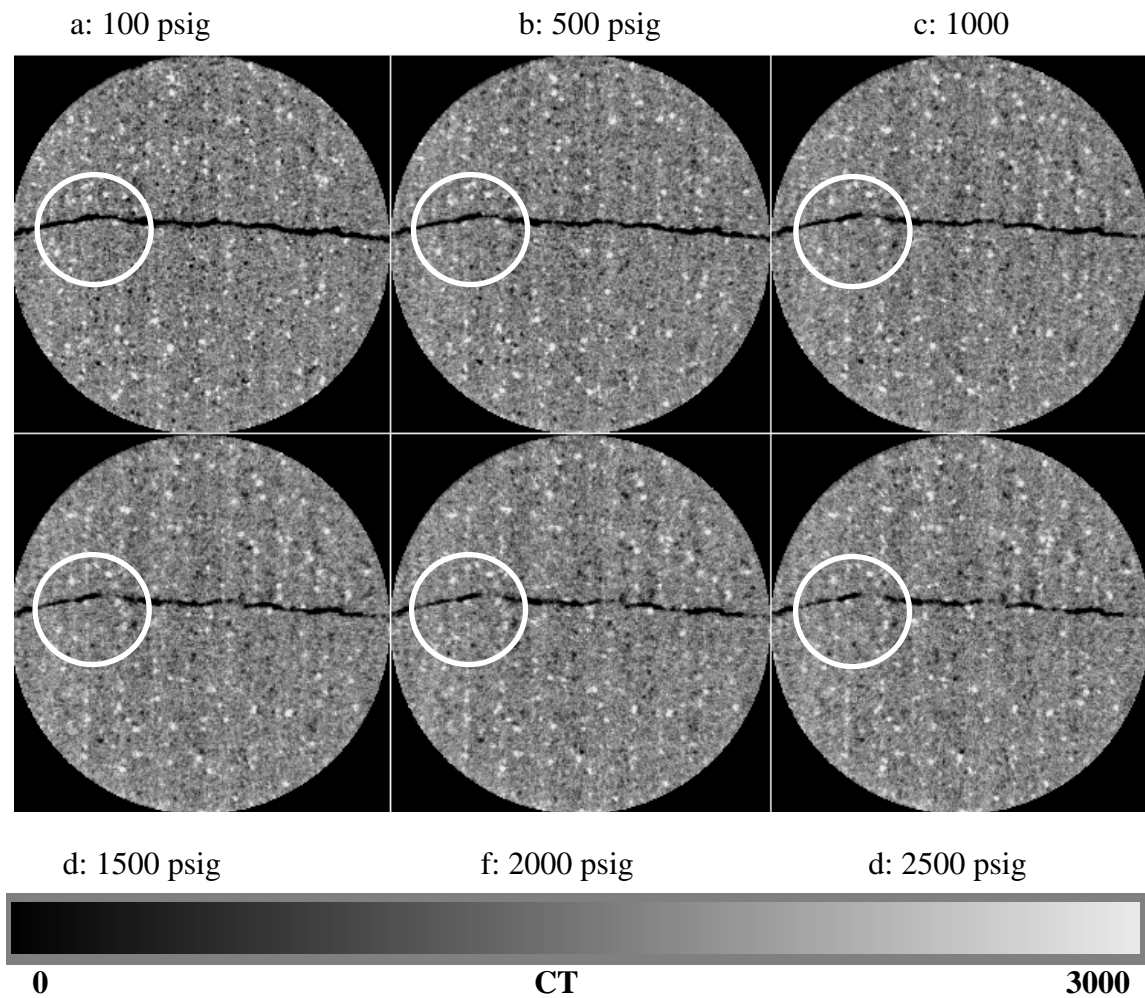


Figure 5.8: CT image at the same location for increasing confining pressure Slice 140.

Figure 5.9 shows CT profiles for different confining pressure values at the same location in the CT slice at the top. The CT profiles highlight an axial displacement of the core as a consequence of the expansion of the aluminum core holder. The axial displacement can be corrected by mapping some characteristic points that are present along the core. For this experiment a maximum axial displacement of (0.1 mm) was estimated between confining pressures of 100 to 2500 psig.

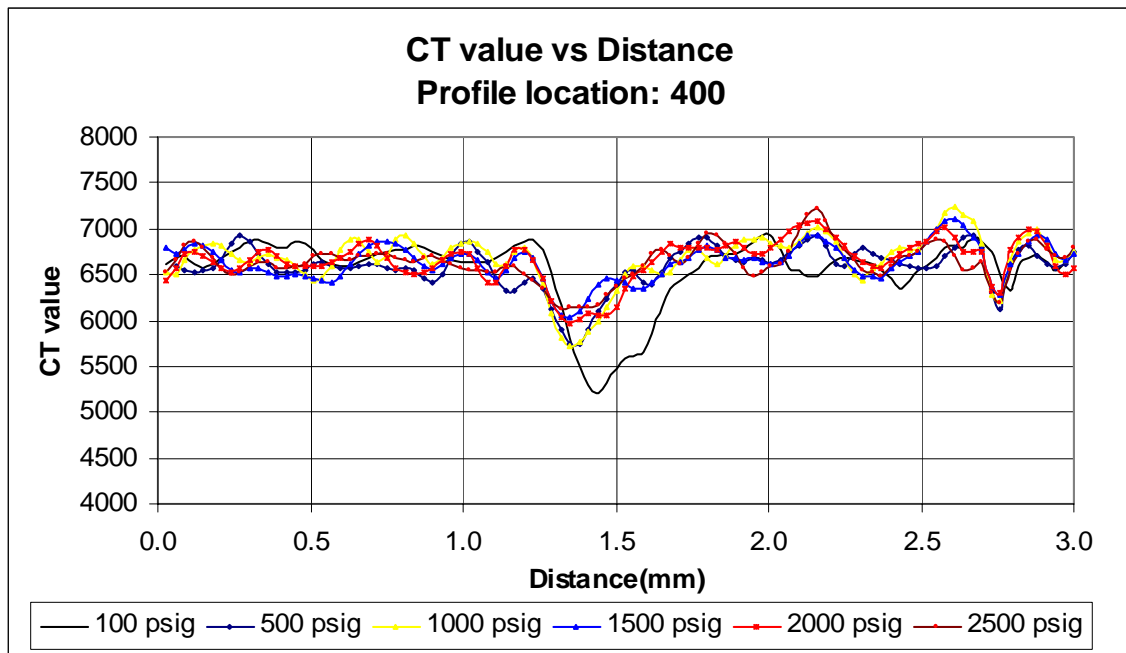
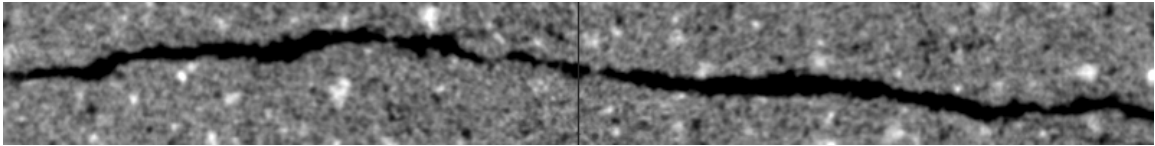


Figure 5.9: Aperture profiles as a function of confining pressure at the same location in the sample.

Figure 5.10 shows the fracture aperture (dry scans) in a two dimensional (24,000 x 3,000 microns) plane for different confining pressure from 100 to 2500 psig. This sequence of images corresponds to slice number 101 at 3636 microns from the top of the core. The white squares highlight areas where new asperities formed in response to an increase in radial stress.

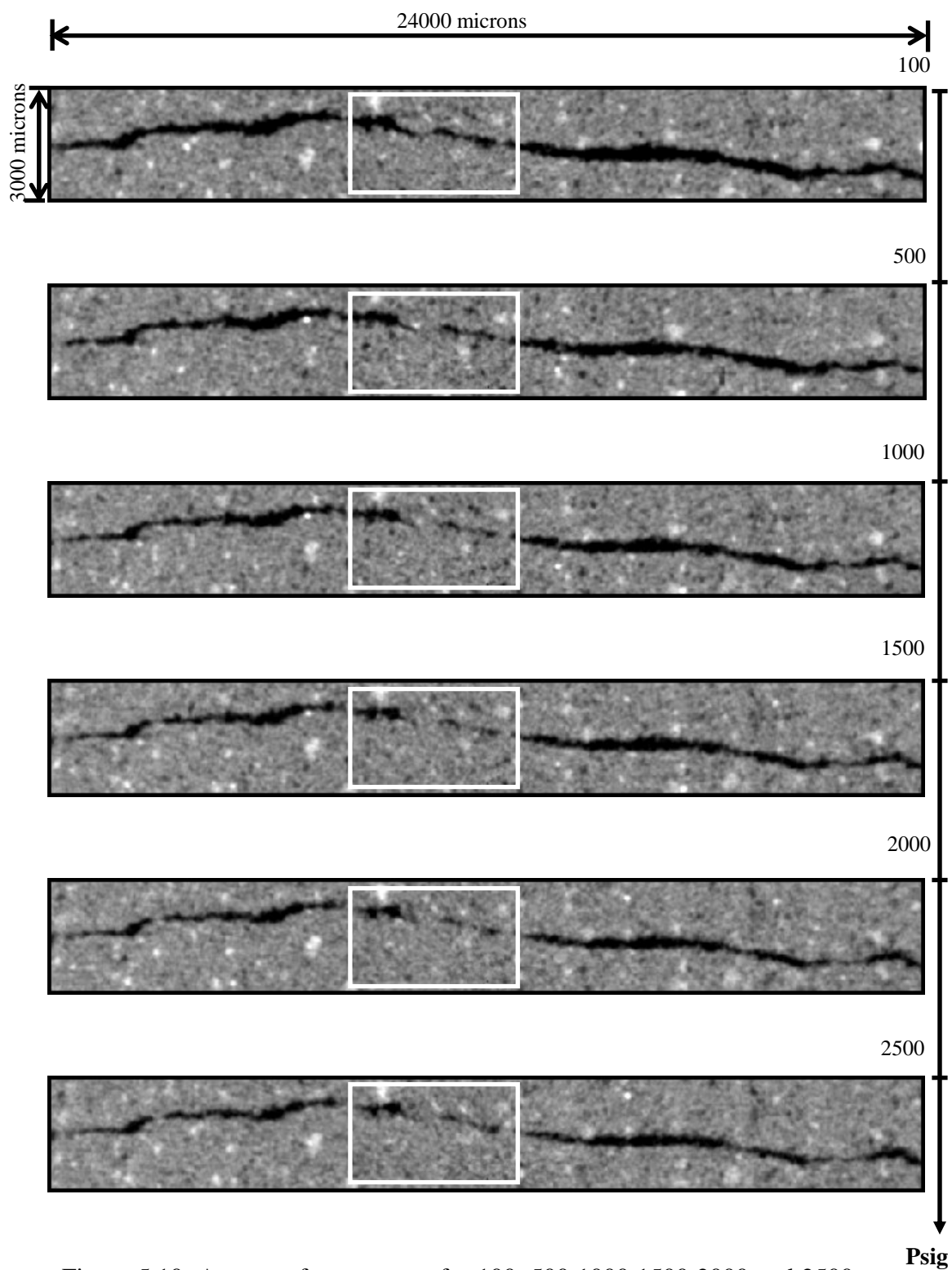


Figure 5.10: Aperture fracture map for 100, 500 1000 1500 2000 and 2500 psig confining pressure.

Figures 5.11a and 5.11c show two different CT profiles for two different locations (4,200 and 19,800 microns). The initial condition (100 psig), and the final condition (2,500 psig) represent the maximum change in confining pressure. The fracture aperture exchange is represented by a drastic reduction in the CT values. The red circles in Figure 5.11b and 5.11c highlight the closure of the fracture (local asperities) in the axial direction. Figure 5.11b also shows how the flow channels are reduced as a consequence of the stress applied to the core.

The presence of new asperities (contact points) creates pipe-flow channels (Figure 5.11b). These channels appeared in the two dimensional plane (x-y) and need to be mapped in the axial direction in order to verify and quantify their influence on the fluid flow.

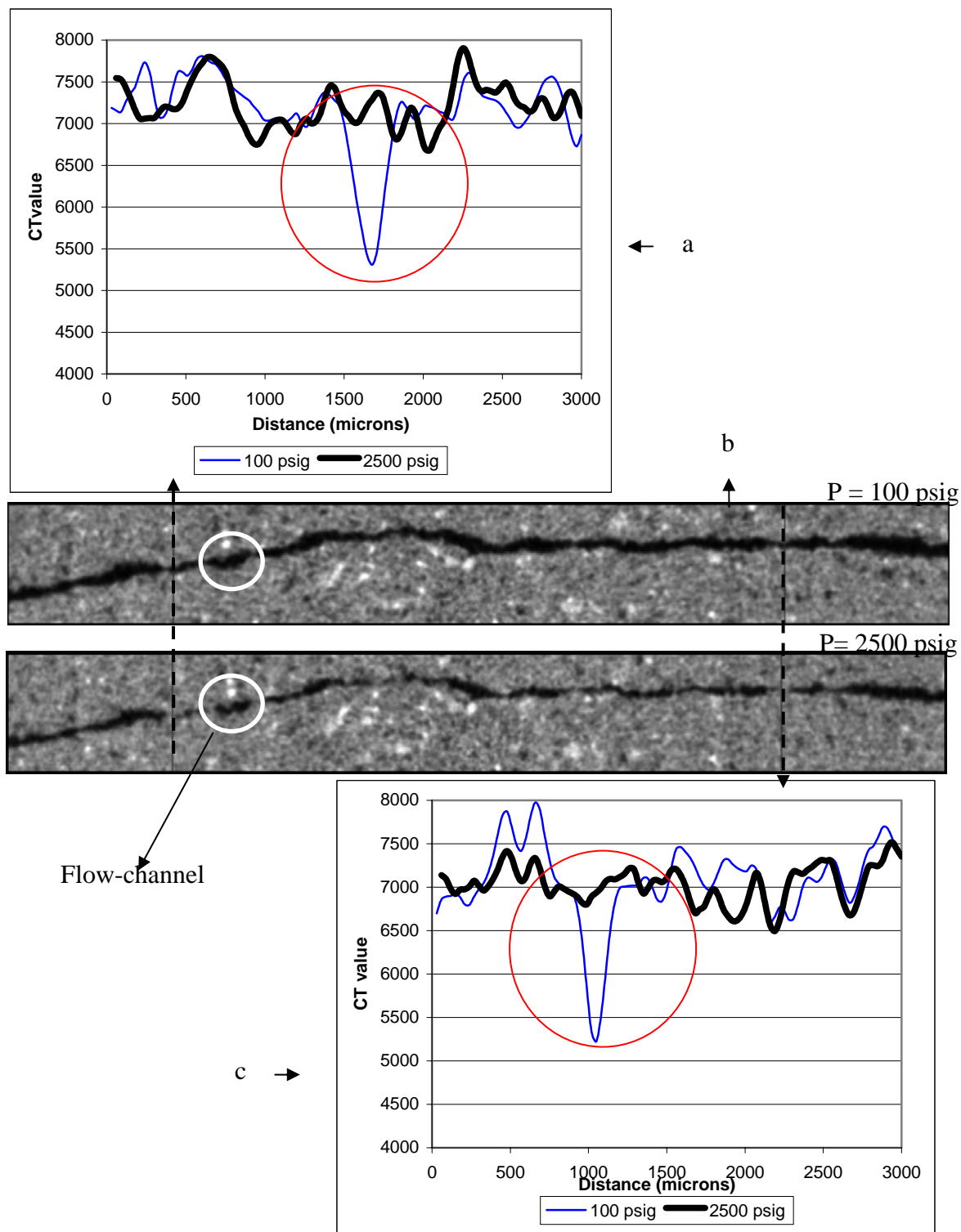


Figure 5.11: a: CT profile at $x = 140$ b: images for 100 and 2500 psig confining pressure c: CT profile at $x = 660$.

Figures 5.12a Figure 5.12d show CT profiles for Figure 5.12b, demonstrating the creation of an asperity by the increase in the confining pressure. The CT profiles show an increment in the CT value from 5000 to 6500 (matrix value). The increase in CT value represents a decrease in fracture conductivity. Figure 5.12c shows a zoom from a secondary fracture at 100 and 2500 psig. The increase in stress closes the fracture and reduces its permeability. This aperture reduction is shown in CT profiles for two of the confining pressure stages, 500 and 2500 psig.

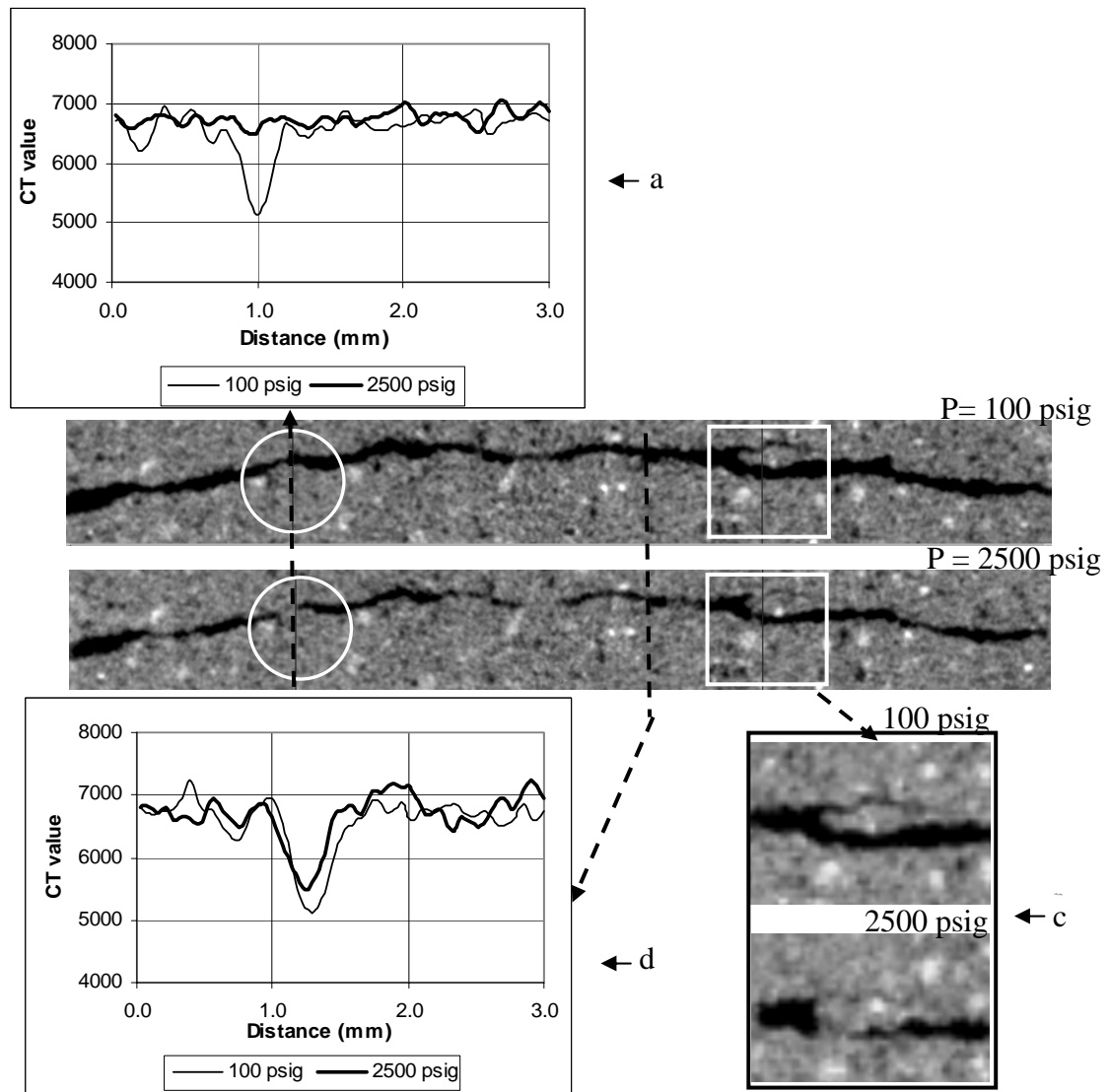


Figure 5.12: CT profiles at different locations (100 psig and 2500 psig confining pressure).

After the original CT image volume scans were reduced to boxes (800x100x410 or 850x120x2204) that contain the fracture, the fracture was characterized by mapping the void space in the sample. Fracture aperture maps and fracture volumes were computed. This process was applied to different confining pressures. Figure 5.13 shows two three-dimensional renditions of the fracture (in red) surrounded by the matrix. Multiple bedding planes can also be observed.

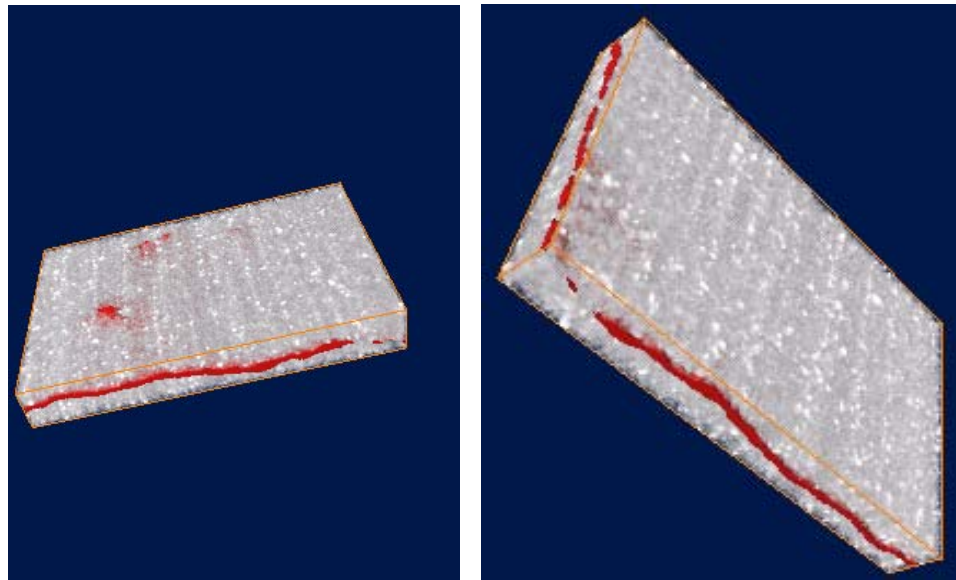


Figure 5.13: Fracture aperture surrounded by matrix.

Figure 5.14 presents an iso-surface of the fracture at 100 psig confining pressure (left) and at 2500 psig (right). The increased black regions in Figure 5.14 (right) remarks the increment in the area of asperities due to the increase in confining pressure. In order to differentiate the fracture from the matrix a threshold must be applied.

The threshold value was selected carefully by visual examination of the data. The dark color in Figure 5.14 represents the asperities. These asperities are fracture contact points and are responsible for the reduction of the conductivity of the fracture.

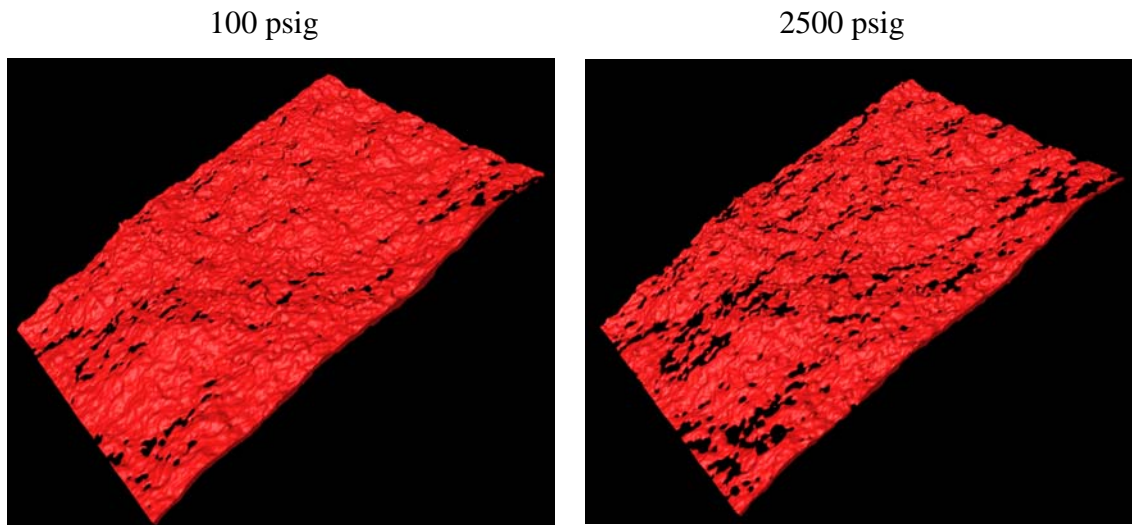


Figure 5.14: Three-dimensional images of the fracture under 100 and 2500 psig confining pressures.

Figure 5.15 shows a three-dimensional rendition of the fracture volume for the 100 psig (left) and 2500 psig (right). A coronal slice ($Y = 50$) shows the undulation of the fracture aperture along the core, emphasizing of the non uniform propagation (wave) of the fracture during the fracturing process. Figure 5.15 also highlights an increment in area of the walls of the fractures after increasing the radial stress.

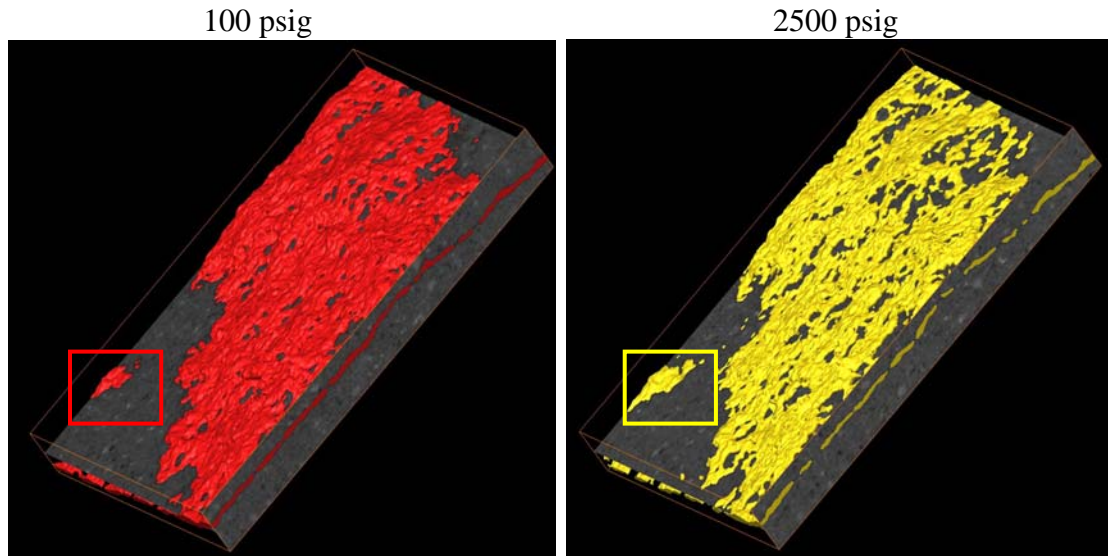


Figure 5.15: Fracture aperture volume with coronal slice planes.

Once the fracture aperture was partitioned (binary) only fracture and solid phases are left in the system. Figure 5.16 shows a schematic representation of the fracture, which is the base for the computation of fracture aperture. The zeros represent the matrix and the ones the fracture aperture.

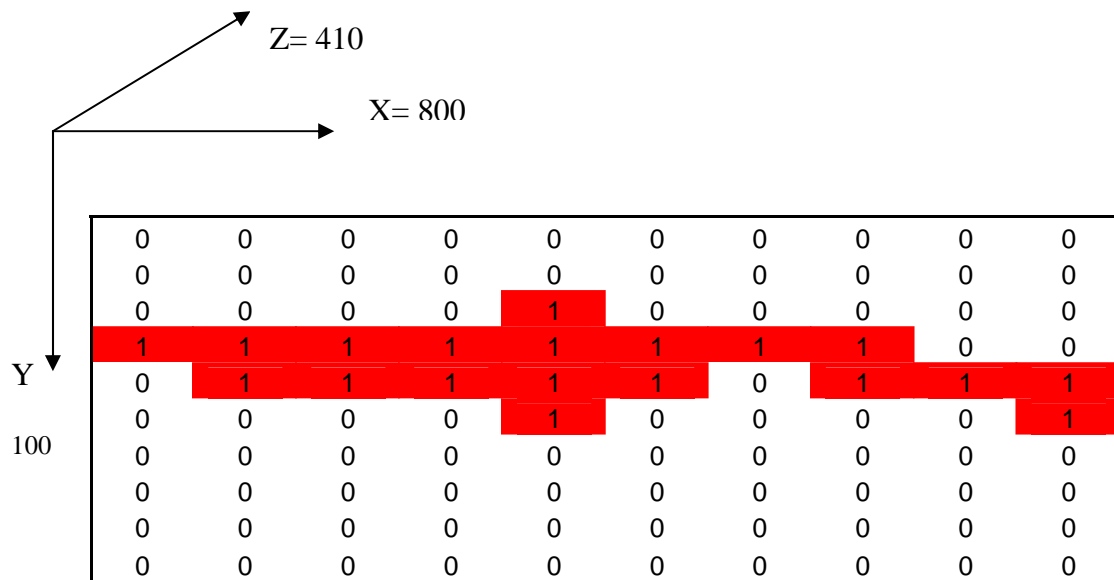


Figure 5.16: Cartoon of the three-dimensional (binary) fracture aperture array.

The Y-direction dimension was 30 microns and is taken to be orthogonal to the fracture and is used in calculating fracture aperture. Figure 5.17 presents 2D fracture aperture maps at 100 psig and 2500 psig.

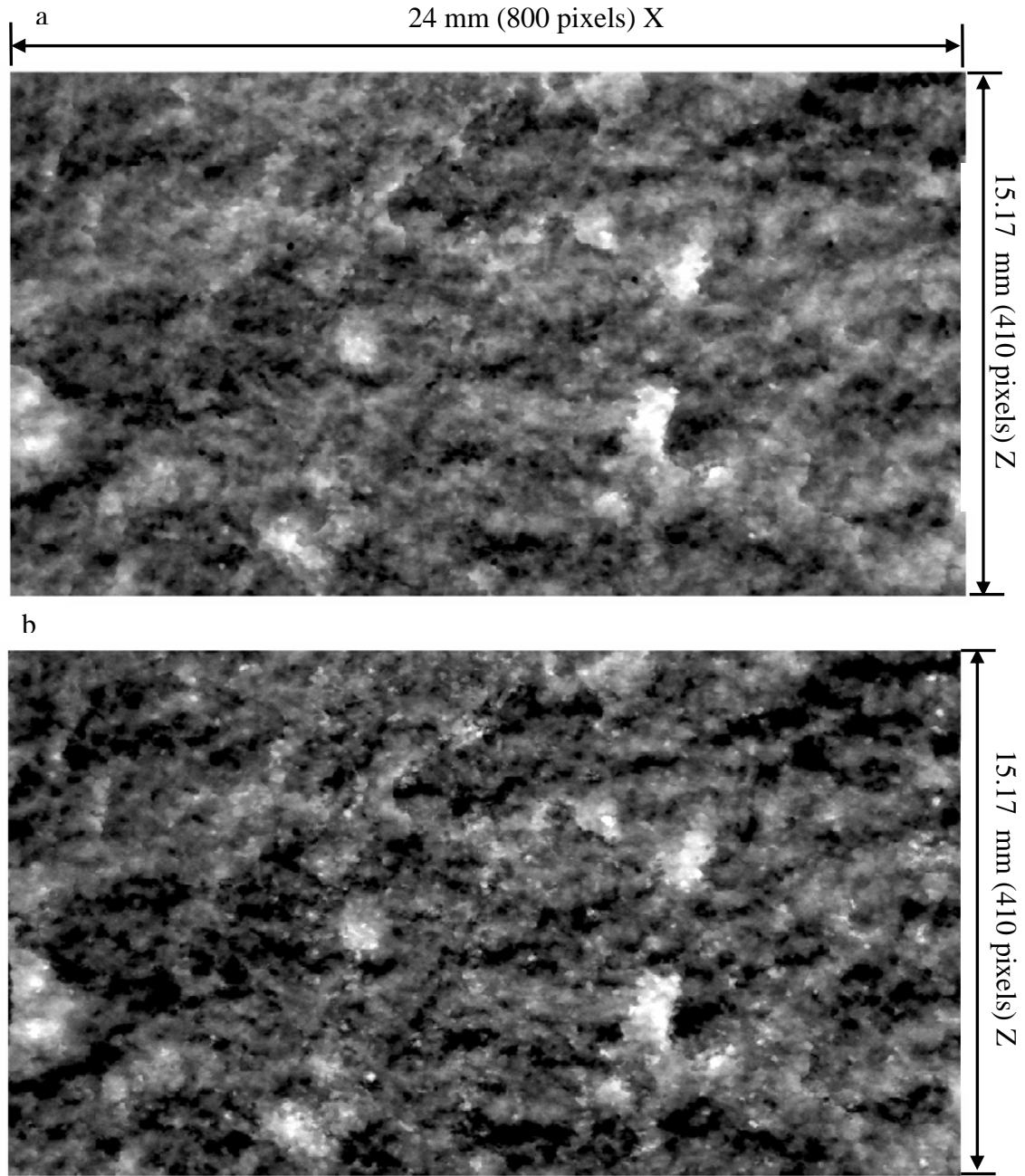


Figure 5.17: Two dimensional fracture aperture maps. a: 100 psig. b: 2500 psig.

The light color highlights high porosity areas (high fracture aperture). The top image corresponds to 100 psig while bottom to 2500 psig. Figure 5.18 highlights the increment in the number of asperities, where red color corresponds to places with zero fracture aperture (less than 30 microns or 1 voxel).

The computed fracture aperture volume was 99.4 cubic millimeters with 1.58 % of the area occupied by asperities at 100 psig, and 83.2 cubic millimeters with 5.69 % asperities for the case of 2500 psig. Figure 5.19 shows the fracture aperture probability distribution (2500 psig) with a maximum probability value of 11.23 % for fracture aperture in the range of 210 to 240 microns. The average fracture aperture was 273 microns for the 100 psig confining pressure and 229 microns for the 2500 psig confining pressure, an over reduction of 15%.

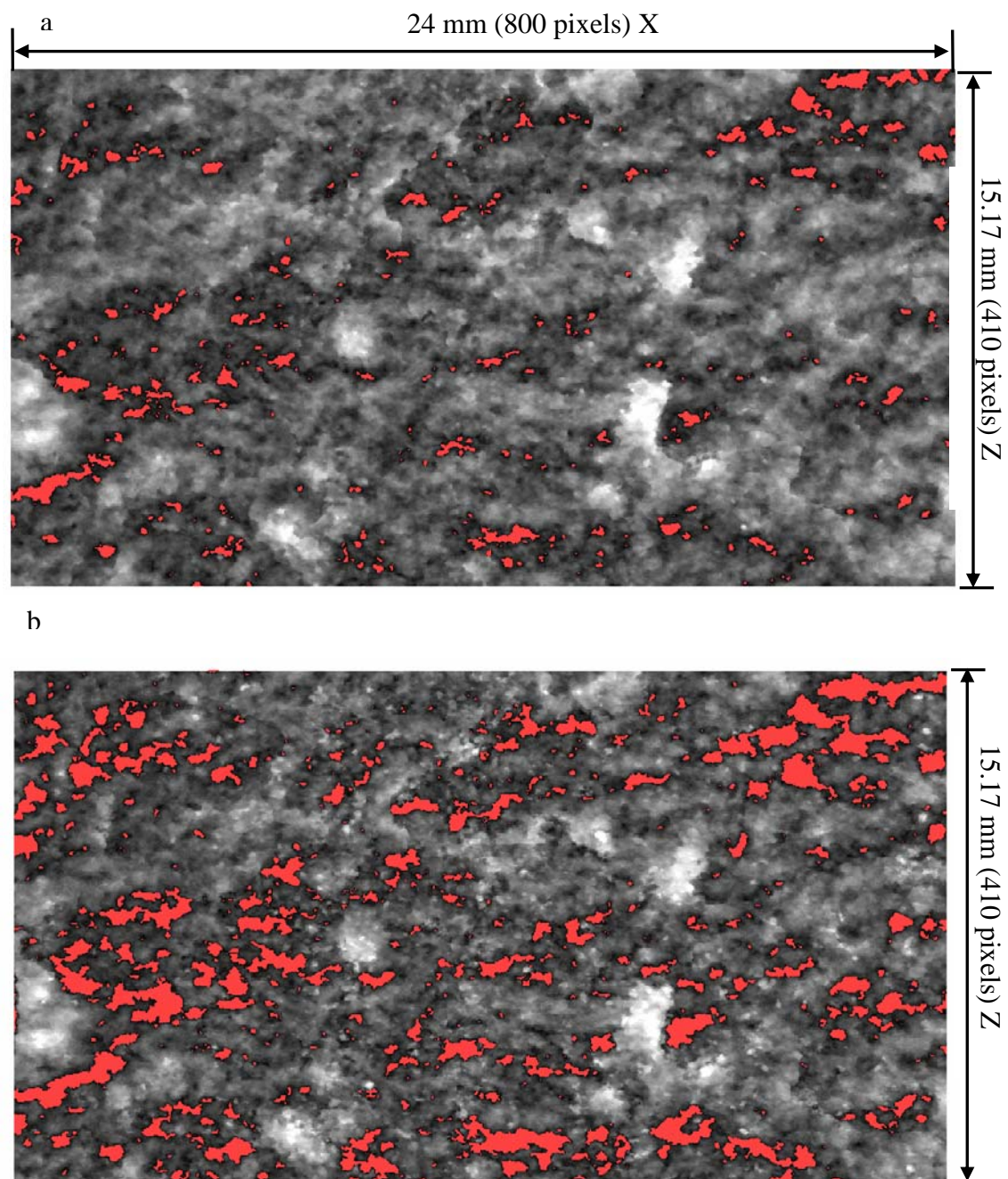


Figure 5.18: Two dimensional asperities maps.

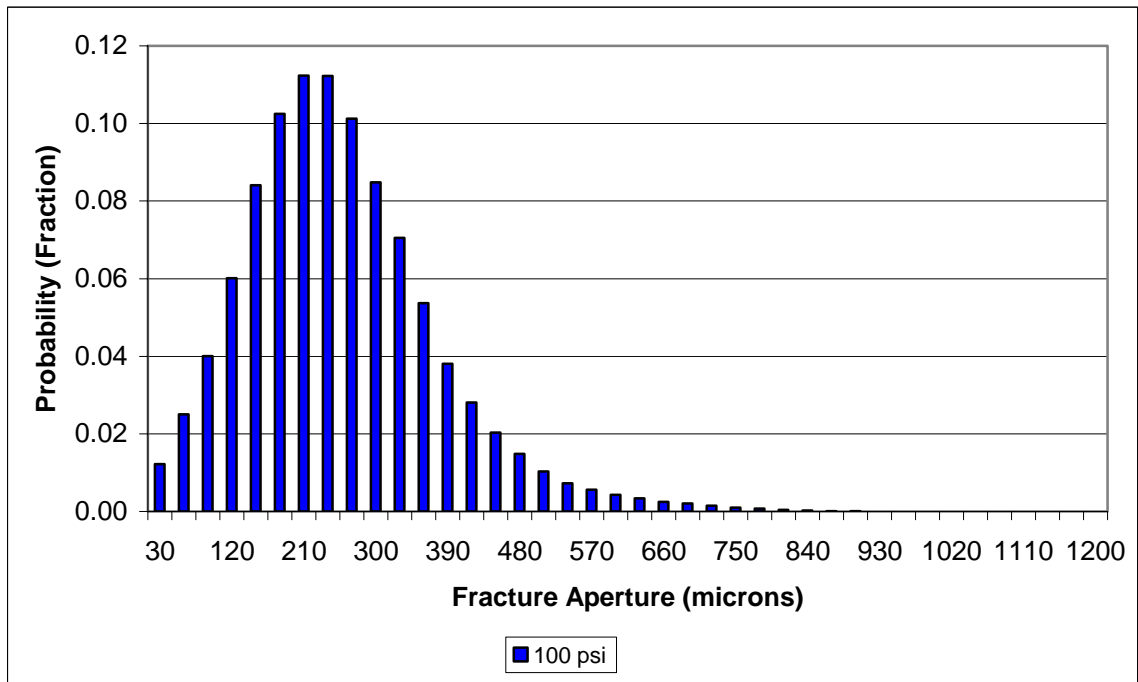


Figure 5.19: Probability plot from the fracture aperture.

Figure 5.20 shows the probability density function against the fracture aperture (2500 psig). Earlier studies, [Gale (1987), Pyrak-Nolte *et al.* (1987)] have suggested lognormal or gamma functions for fracture aperture distributions, highlighting the importance of the tail of such distributions that represents channel flow. Therefore, it is extremely important to characterize the fracture aperture not only based on the fracture porosity but also based on the interconnectivity of the fracture and the possibility of having flow channels.

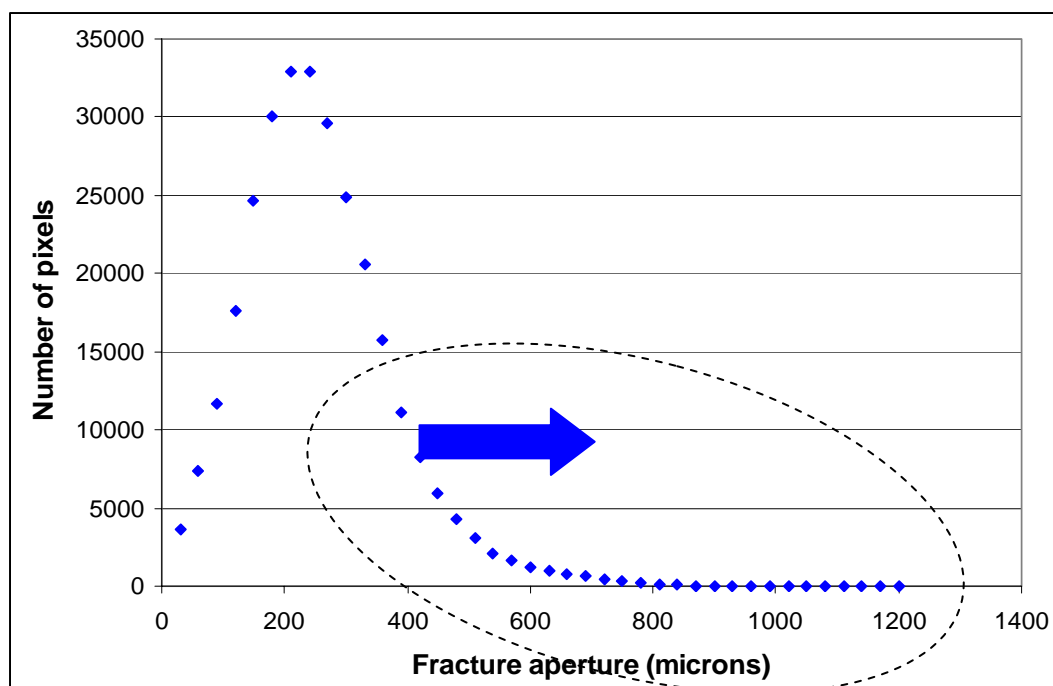


Figure 5.20: Fracture aperture distribution (2500 psig).

Figure 5.21 presents the fracture aperture distribution for the 100 and 2500 psig. The 2500 psig curve is axially displaced (down) and shifted to the left indicating the reduction of fracture aperture.

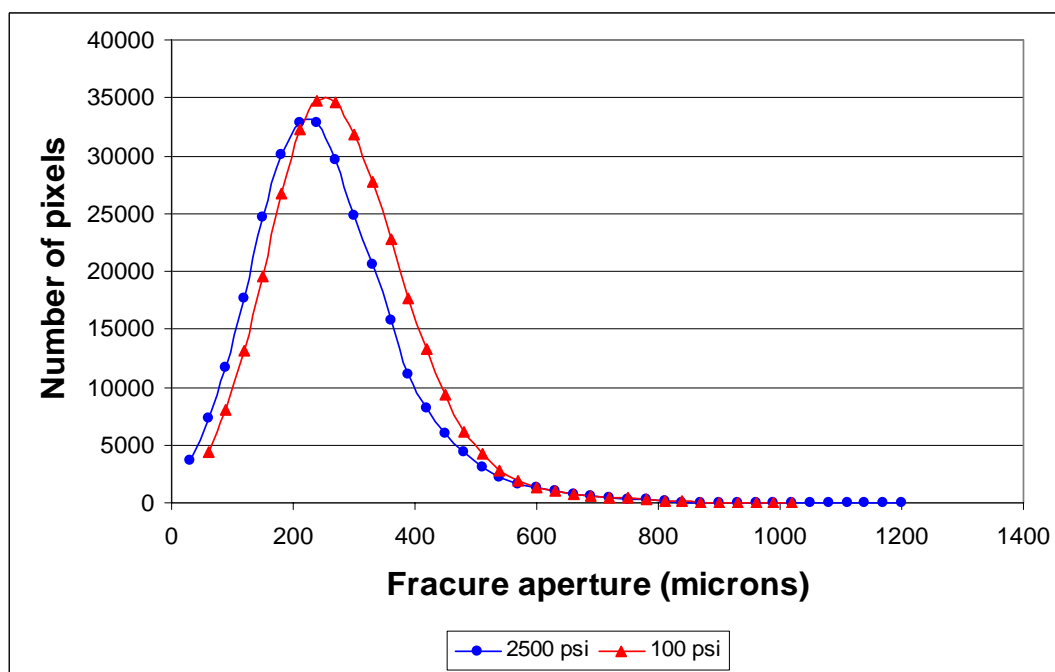


Figure 5.21: Fracture aperture distributions for 100 and 2500 psig.

Using the fracture aperture distribution Zimmerman *et al.* (1991) suggested that the roughness of the fracture can be described or represented by the ratio of the standard deviation and the mechanical aperture of the fracture aperture distribution:

$$\text{Roughness Factor} = \frac{\sigma_m}{a_m} \quad (5.1)$$

Where σ_m represents the standard deviation and a_m the mechanical aperture.

A perfect parallel model has uniform fracture aperture and therefore a zero standard deviation, leading to a zero roughness factor. For the 100 psig and 2500 psig confining pressure the roughness factors were calculated. Table 5.1 shows the computed values, where the 2500 psig shows a higher deviation from the zero indicating an increase in roughness in the fracture as a consequence of the increase in the area of the asperities and the reduction in the average fracture aperture. Figure 5.22 presents a volume fracture aperture map. The black color represents no flow (asperities) and the red color represents open fracture (potential flow paths

Table 5.1: Roughness factor values

Confining Pressure (psi)	a_m (microns)	σ_m (microns)	Roughness Factor
100	281	281	1.06
2500	351	256	1.32

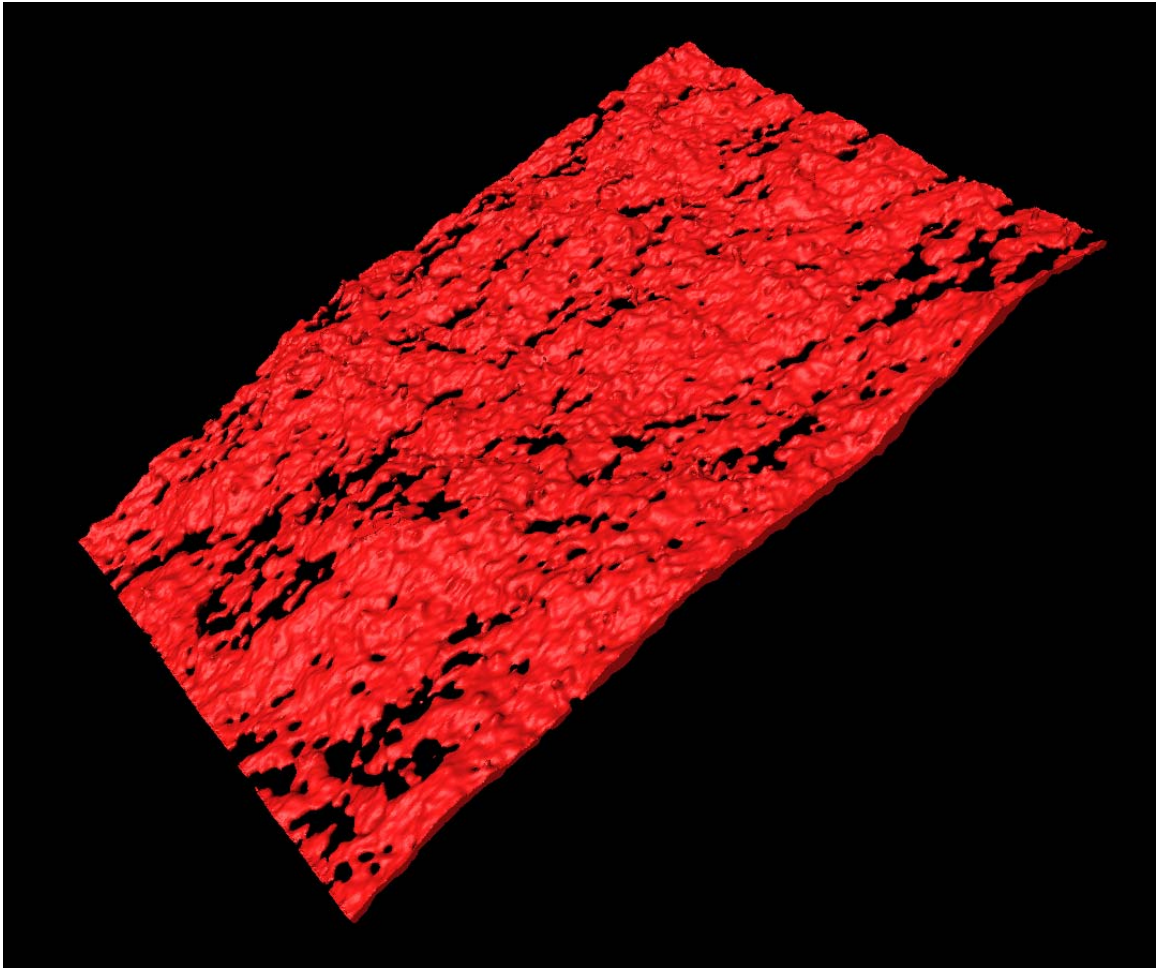


Figure 5.22: Three dimensional representation of fracture aperture at 2500 psig.

In order to analyze the conductivity of the fracture the tail of the fracture was extracted from the fracture aperture data. Figure 5.23 shows potential flow paths in the fracture, where the yellow regions highlight regions where the fracture aperture is greater than 360 (12 pixels) microns. These regions correspond to the tail of the fracture distribution shown in Figure 5.20.

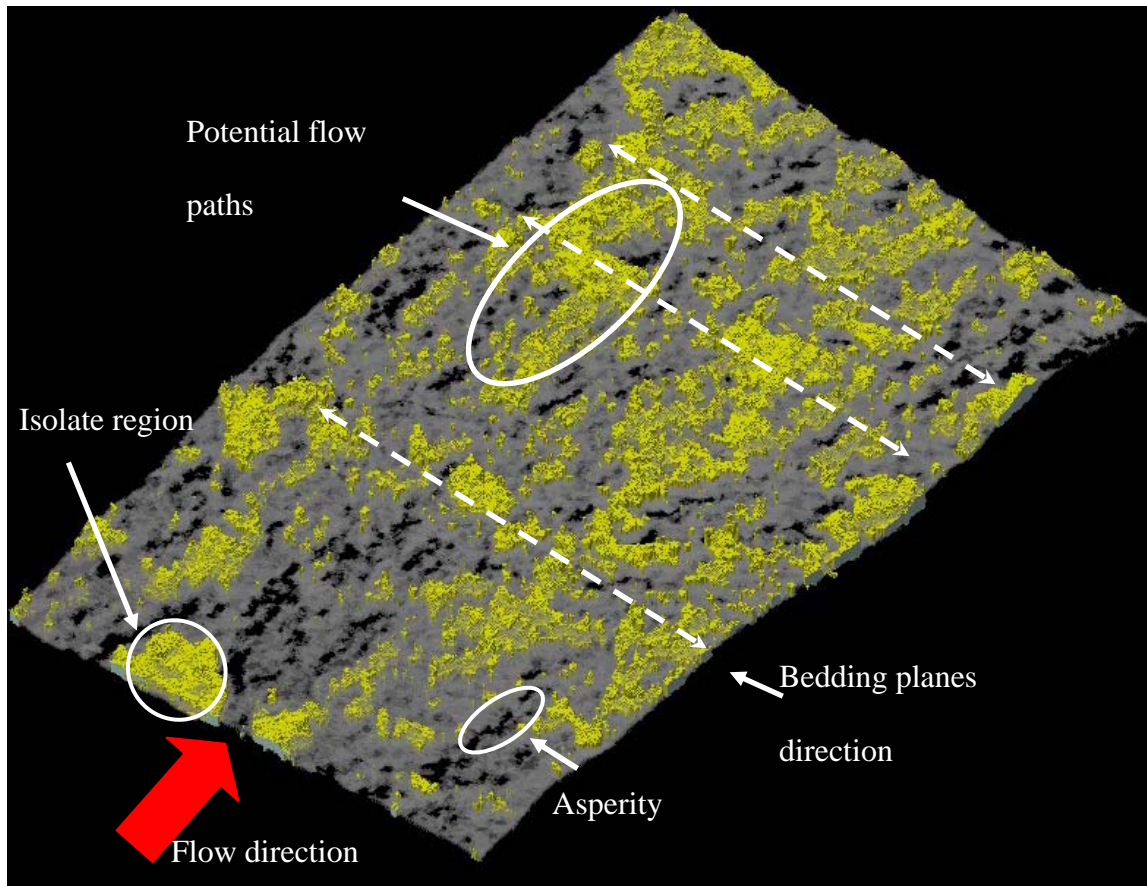


Figure 5.23: Fracture aperture distribution 360 microns thickness or more.

From Figure 5.23 it is also possible to identify isolated regions (white circle on Figure 5.23) that do not contribute to the fluid flow. Few flow channels in the bedding plane direction (perpendicular to fracture plane) can be observed.

5.2.1 Structure Model Index (SMI)

A Structure Model Index has been used to characterize the fracture aperture. Hildebrand *et al.* (1997) defined a morphometric parameter called Structure Model Index (SMI). The SMI parameter is used to quantify the characteristics form of a three-dimensional structure in terms of the amount of plates and rod composing the structure. This technique is base on the differential analysis of the triangulate surface and was implemented in bones for finding the deterioration of cancellous bone structure due to diseases. The SMI index parameter varies from 0, 3, and 4 corresponding to objects that have the shapes of plates, rods, and spheres, respectively. The Structure Model Index is given by Equation 5.2:

$$SMI = 6 \left[\frac{S'V(r)}{S(r)^2} \right] \quad (5.2)$$

Where $S' = \frac{\partial S}{\partial r}$, (r) represents the normal direction to the surface of the fracture and S' is the derivative of the surface area with respect to the orthogonal direction (r). V and S represent the fracture volume and surface area respectively. S' is computed by creating a displacement of the original surface incrementally by a factor Δr and evaluating the new surface are at the $r + \Delta r$ position. Equation 5.3 shows the numerical computation of S':

$$S' = \frac{\partial S}{\partial r} = \frac{S(r + \Delta r) - S(r)}{\Delta r} \quad (5.3)$$

Hildebrand and Rueggeger suggested a Δr value between 0.001 and 0.1 of the element edge voxel. The displacement used in this work corresponds to a ratio of 0.01 times the voxel size ($\Delta x = \Delta y$) for a Δr equal to 0.00026 mm.

Table 5.2 highlights the numerical computation of the Structure Model Index for Core BS2 at two different confining pressures, 500 and 2500 psig. The increase of the SMI highlights the closure and deformation of the fracture, where new non connected channels have been created.

Table 5.2: SMI parameters for 500 and 2500 psig.

Pressure (psig)	<i>Coefficients</i>						SMI
	So (r) (mm ²)	S1(r+Δr) (mm ²)	Vo (mm ³)	V1 (mm ³)	Δr (mm)	S'	
Fracture 500	4216.78	4219.03	373	374	0.00026	8654.6	1.090567
Fracture 2500	3777.83	3780.92	278	279	0.00026	11884.6	1.388956

Figure 5.24 shows the SMI coefficient for a series of changes in confining pressure from 100 to 2500 psig (core BS1). At low pressure a significant SMI increment is observed (~0.37). However, when the confining pressure goes up the SMI is asymptotic to a value of 2.5. This behavior is consequence of the small reduction of the volume fracture related to the changes in surface area, consequence of the induced asperities in the system.

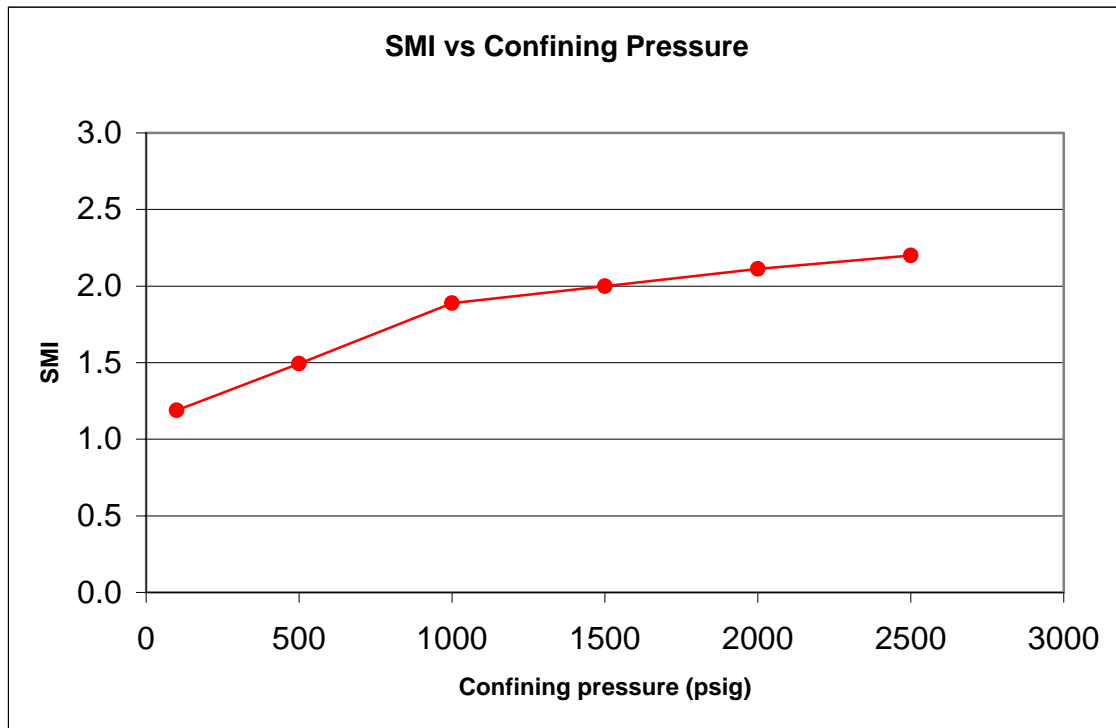


Figure 5.24: Structure model index for different confining pressure.

5.2.2 Connectivity density coefficient (EPC)

The Euler-Poincaré coefficient (EPC) was computed for the fracture structure. This coefficient is a measure of the connectivity density (connections per unit volume). The Euler-Poincaré characteristic of a three-dimensional structure is a topological invariant, which reports the number of particles of a structure plus the number of enclosed cavities minus the connectivity. This technique has been used for the quantification of connectivity in bones and is summarized by Odgaard *et al.* (1993) This method uses the number of voxels faces, edges, and corners associated with a three dimensional object that is composed of voxels.

Prior to computing the EPC, the fracture was segmented by applying a threshold (2400). A binary system was created, where the number one was assigned to the fracture pore space and the number zero to the matrix volume. The dimensions (X, Y and, Z) of the entire sample containing the fracture were 20.8 x 3.12 x 63.49 mm or 800x120x2048 (voxel size), where the voxel sizes were $dx = dy = 0.026$ mm and $dz = 0.031$ mm. The three dimensional fracture volume sub-divided (gridding) in the x and z direction, keeping the aperture direction of the fracture (y) constant and equal to 3.12 mm (120 voxels). Once the fracture was sub-divided into different blocks an EPC was computed for each block. Figure 5.25 shows the dry fracture at 2500 psig (left) and the subdivision where the fracture sample was divides into four equal sub-blocks (2x2 case). Other subdivisions included were 16 blocks (4x4), 64 blocks (8x8), and 256 blocks (16x16).

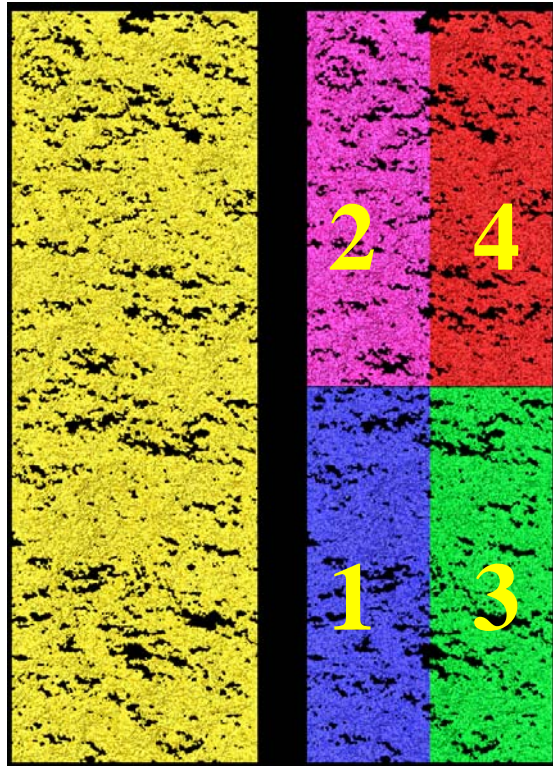


Figure 5.25: Fracture sub-division scheme into 4 blocks (2x2).

Table 5.3 highlights the dimension of each block during the fracture refining process. The EPC and SMI results are summarized in Table 5.4.

Table 5.3: Summary of the segmentation process and block dimensions

Grid	Total blocks	dx (mm)	dy (mm)	dz (mm)	Voxels
1x1	1	20.800	3.120	63.488	800x120x2048
2x2	4	10.400	3.120	31.744	400x120x1024
4x4	16	5.200	3.120	15.872	200x120x512
8x8	64	2.600	3.120	7.936	100x120x256
16x16	256	1.300	3.120	3.968	50x120x128

Table 5.4: Summary of SMI and Euler-Poincaré values (Averages)

	500 psig		2500 psig	
	Euler-Poincaré	SMI	Euler-Poincaré	SMI
1x1	0.325	1.963	0.432	2.275
2x2	0.323	2.423	0.431	2.482
4x4	0.323	2.334	0.430	2.371
8x8	0.322	1.554	0.429	1.769
16x16	0.315	1.288	0.425	1.593

An increase in the Euler-Poincaré number for the change in confining pressure was observed. This increase in connection density is a consequence of creating new asperities. Figure 5.26 shows the distribution of Euler-Poincaré values for the 16x16 case at 500 psig. The computed average value for this case was 0.3157.

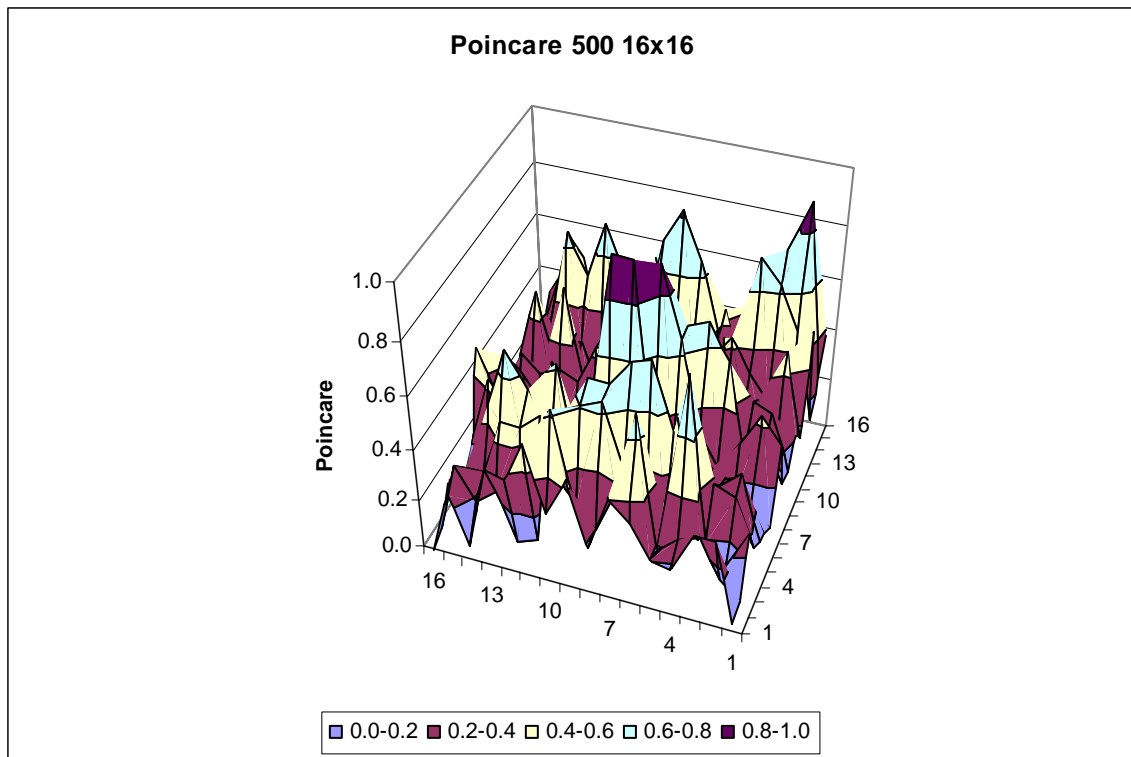


Figure 5.26: Euler-Poincaré distribution for the 16x16 case at 500 psig.

Figure 5.27 presents the corresponding Euler-Poincaré graph for the 2,500 psig case (16x16) where the average value was 0.4256.

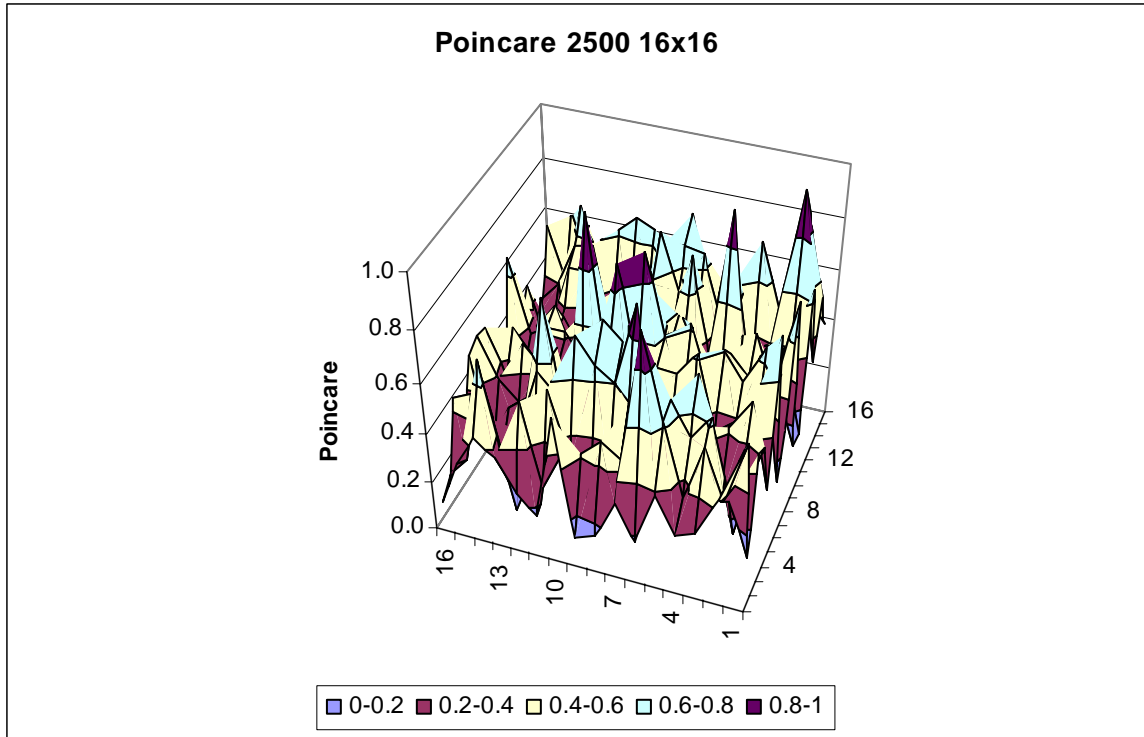


Figure 5.27: Euler-Poincaré distribution for the 16x16 case at 2500 psig.

The connectivity changes in the fracture are quantified by variations in connectivity densities (EPC) and for changes in the fracture structure (SMI). Figure 5.28 shows the SMI changes in the 16x16 case at 2500 psig, where a SMI average was equal to 1.288 for 500 psig and 1.593 for 2500 psig. Both method, EPC and SMI show agreement from the structural and connectivity point of view, highlighting regions with significant structural changes for both cases, 500 and 2500 psig.

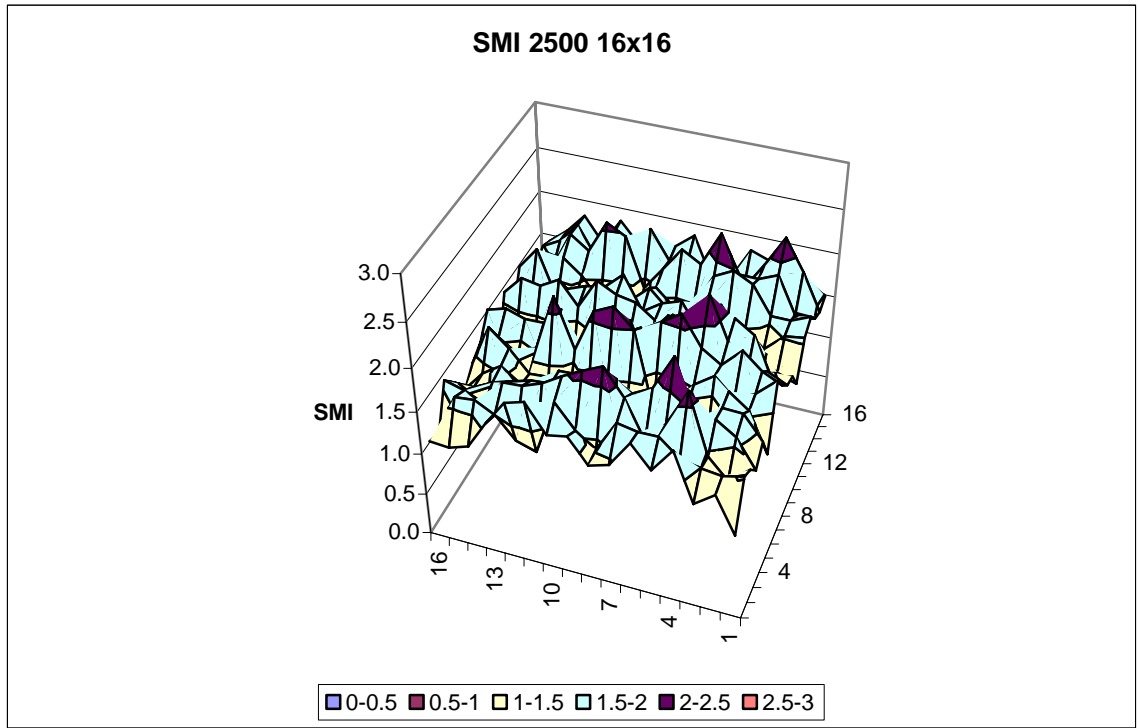


Figure 5.28: SMI distribution for the 16x16 case at 2500 psig.

A clear application of the EPC would be to identify fracture characteristic that can be used to simulate flow conditions in micro fractured models. Figure 5.29 shows blocks 135 and 241 for the 256 (16x16) case. They were identified as the maximum and minimum Euler-Poincaré number at 500 psig. The block on the Figure 5.29 (a) has a 0 EPC while the one on the right, Figure 5.29 (b), has an EPC of 0.947. The block of low EPC value has a smaller volume (1.77 mm^3) than the one of high Euler-Poincaré (1.69 mm^3). As has been proved previously, an increase in confining pressure creates more asperities that can be correlated with a high EPC (high connectivity density).

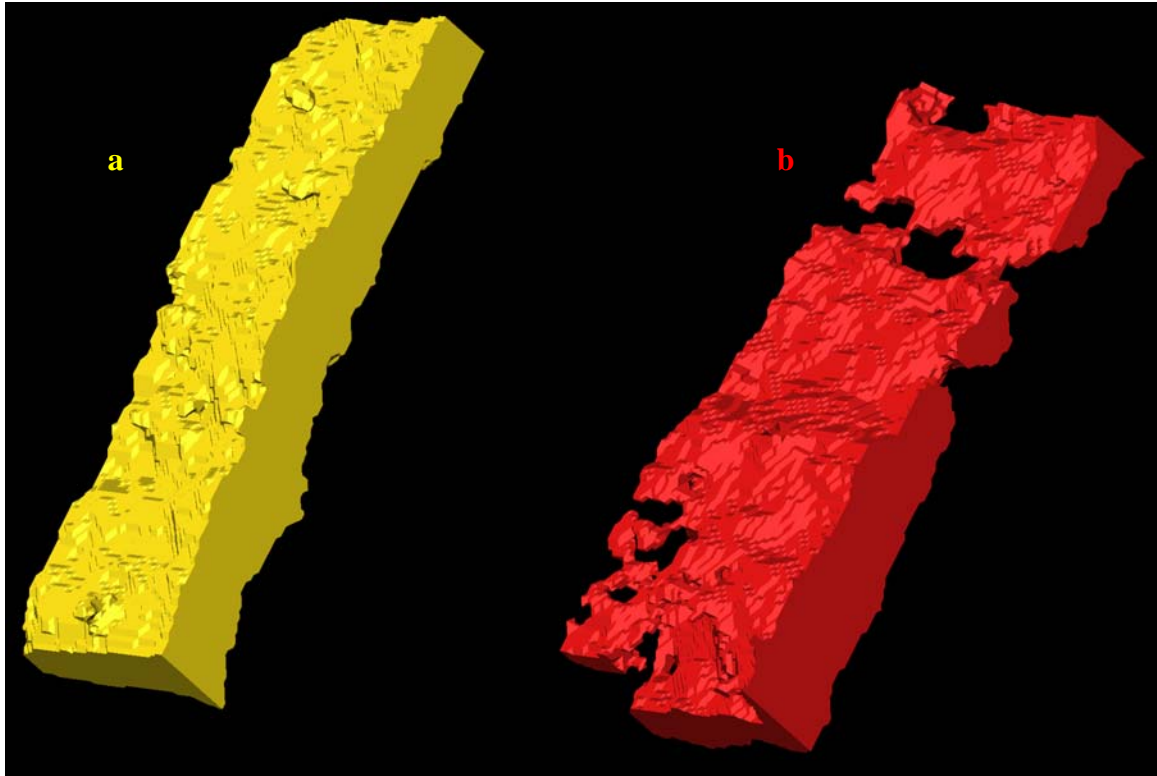


Figure 5.29: SMI distribution for the 16x16 case at 2500 psig. The width is 3.120 mm and the length is 3.968 mm.

So far, the effect of confining pressure has been addressed by using the Euler-Poincaré and the Structure Model Index. The EPC and SMI parameters were computed for the entire fracture. However, a segmentation process over the fracture intends to find the minimum representative volume in which the SMI and EPC are stable. Individual EPC and SMI values will help to find specific changes in the fracture that can correlate the fluid flow patterns in the fracture. Figure 5.30 shows the Euler-Poincaré for the 4 cases, 2x2, 4x4, 8x8 and 16x16 where the average is slightly decreasing when the segmentation increases. The Euler-Poincaré value for the entire fracture was 0.4321 at 2500 psig.

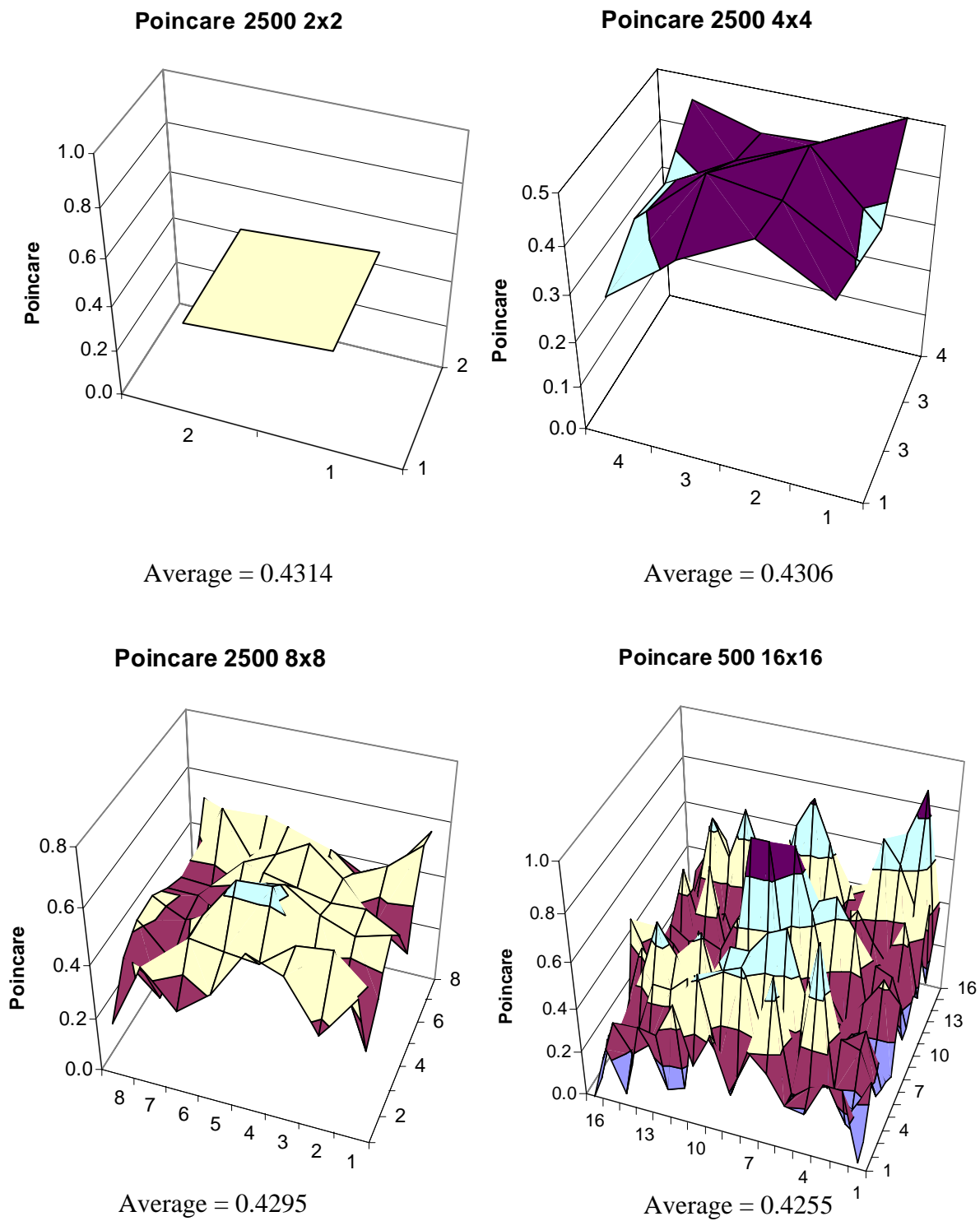


Figure 5.30: EPC distribution for the 2x2, 4x4, 8x8 and 16x16 case at 2500 psig.

The average value for the Euler Poincaré does not significantly change for the given refining process, 2x2, 4x4, 8x8 or 16x16. Figure 5.31 show the average values for those grid blocks at 500 and 2500 psig.

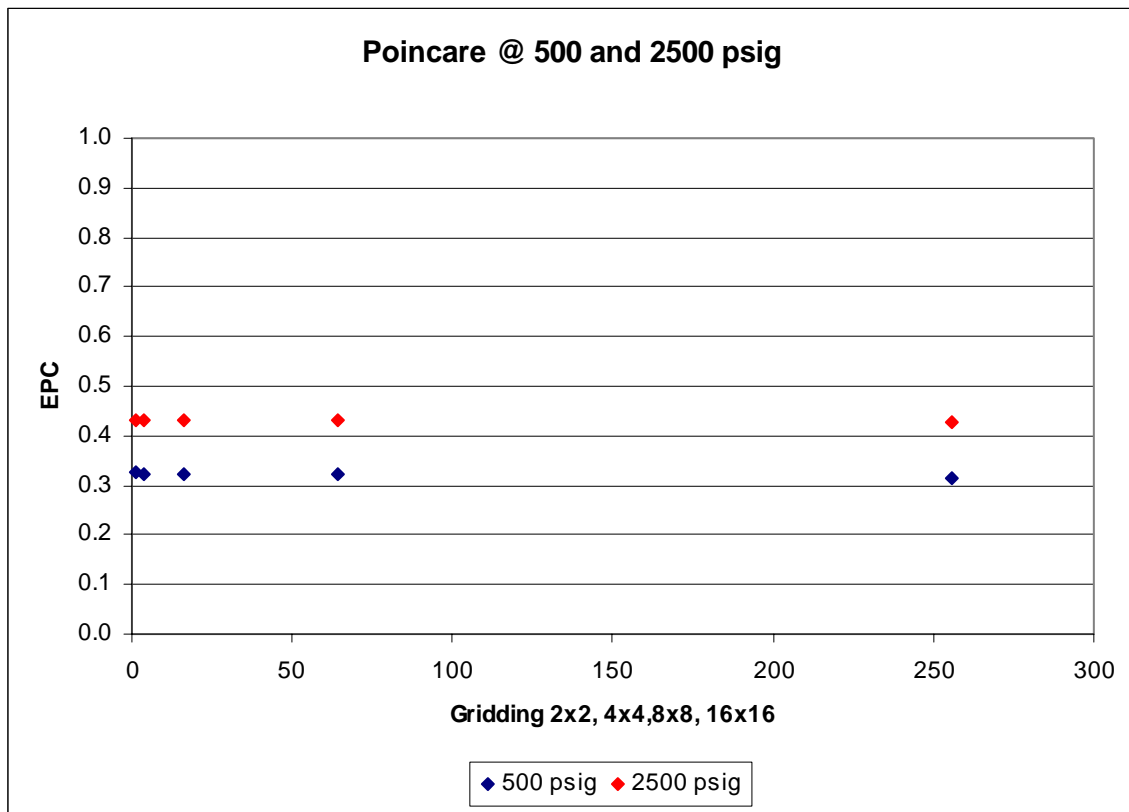


Figure 5.31: EPC average values for the 2x2, 4x4, 8x8 and 16x16 case at 500 and 2500 psig.

The SMI average values seem to be more sensitive to the segmentation process. Figure 5.32 shows the SMI behavior with respect to the segmentation process.

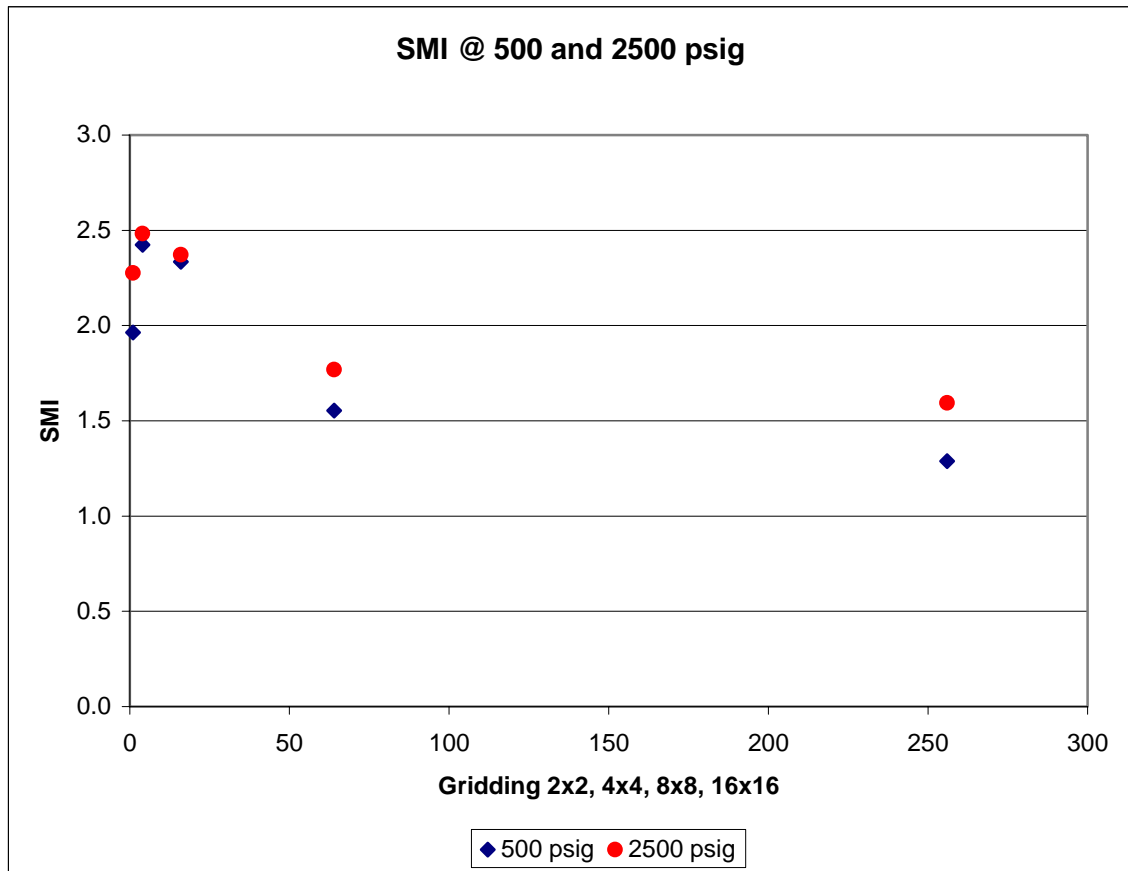


Figure 5.32: SMI average values for the 2x2, 4x4, 8x8 and 16x16 case at 500 and 2500 psig.

The SMI values of the confining pressure of 2500 are (red points) are higher than the ones computed from the 500 psig, highlighting a more rod type of structure. However, as the fracture is segmented, the SMI shows an increase in its values at the beginning of the segmentation process (2x2), followed by a monotonic decrease. Oscillations of the SMI average value would compromise the utilization of individual SMI for a general fracture characterization.

5.3 Fluid flow experiments

All the flow experiments were performed using a Berea sandstone core. The measured absolute permeability, matrix flow, was on the order of 100 mD (using water with 7% by weight KCl). The cores were fractured as described in Chapter 4. After creating the tensile fracture, the two halves of the fracture were shifted axially by 200, 300 and 400 microns in order to create new asperities in the system. Different total liquid flow rate, 3, 6, 9 and 12 cc/min were tested. Based on the average fracture aperture and the pressure drop obtained, all cores were shifted by 400 microns and a total flow rate of 12 cc/min was used. Different fractional flow values were chosen to evaluate the effect of multiphase flow on rocks with single fractures where most of the flow is expected to be in the fracture.

The injection of the two phases (Brine and Kerosene) into the fracture was performed using the end plugs described previously. The pressure drop in the fracture was measured at the faces of the fracture using two pressure ports, one for each flow distributor. A high-accuracy digital pressure transducer with a range from 0-18 psig was used.

Table 5.5 shows the different flow rates for liquids and the fractional flow values used to create changes in the overall pressure drop of the system. The fractional flow is defined as the ratio of water flow rate divided by the total liquid flow rate, see Equation 5.4.

$$f_w = \frac{q_w}{q_w + q_o} \quad (5.4)$$

Where q_w represents the water flow rate and q_o the oil flow rate (kerosene).

The changes in pressure drop are a consequence of the difference in relative permeability, saturation history, and different viscosities and interfacial tensions.

Table 5.5: Liquid flow rates and fractional flow

q_w (cc/min)	q_o (cc/min)	q_t (cc/min)	f_w
12.0	0.0	12	1.00
11.0	1.0	12	0.92
10.0	2.0	12	0.83
9.0	3.0	12	0.75
8.0	4.0	12	0.67
7.0	5.0	12	0.58
6.0	6.0	12	0.50
5.0	7.0	12	0.42
4.0	8.0	12	0.33
3.0	9.0	12	0.25
2.0	10.0	12	0.17
1.0	11.0	12	0.08
0.0	12.0	12	0.00

5.3.1 Core # 1

Figure 5.33 presents the pressure drop along the fracture after changing the confining pressure from 800 to 1000 psig at the fixed injection rate. The pressure drop in the system at 1000 psig shows a higher value than in 800 psig. This is a consequence of the closure of the fracture due to the increase in confining pressure. This behavior (aperture closure) with increase in confining pressure was mechanically confirmed in the previous section by using CT.

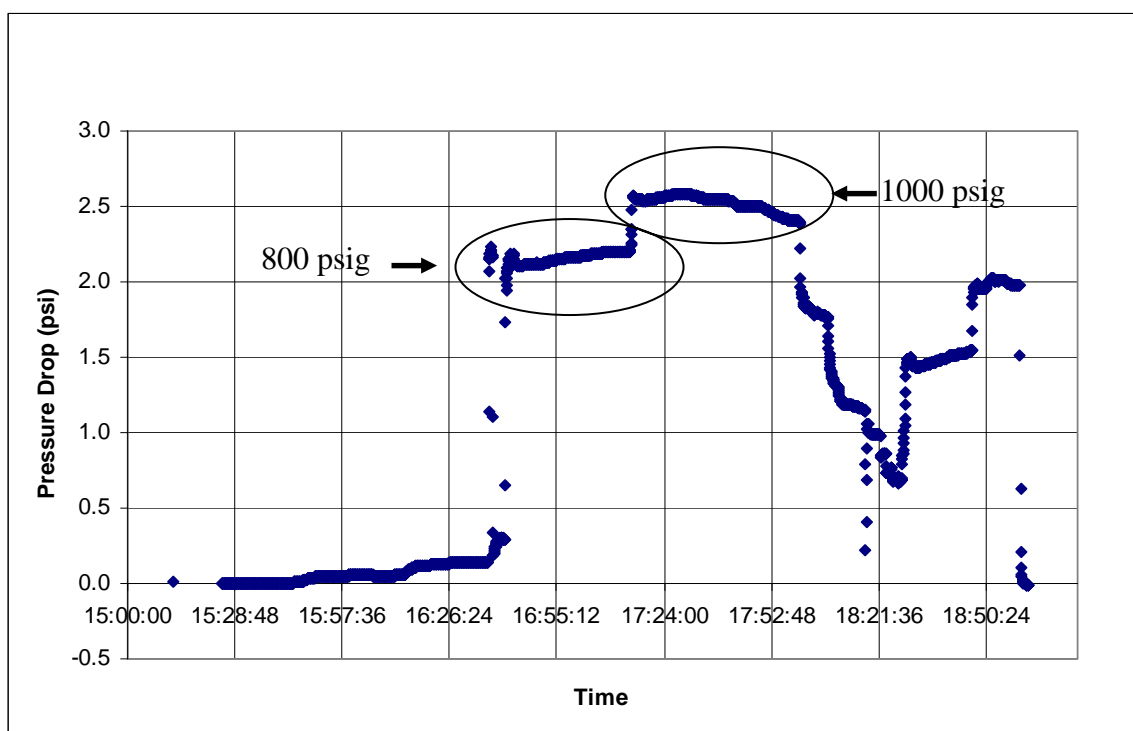


Figure 5.33: Changes along pressure drop for different confining pressure at fixed injection rate.

Figure 5.34 shows the changes in the pressure drop (confining pressure of 800 psig) in the fracture for different fractional flows, from 1 to 0. A global maximum value of 2.2 psi in the system is observed for a fractional flow of 33%. A similar graph for a confining pressure of 1000 psig is shown in Figure 5.35 with a maximum pressure drop for a fractional flow of 0.4.

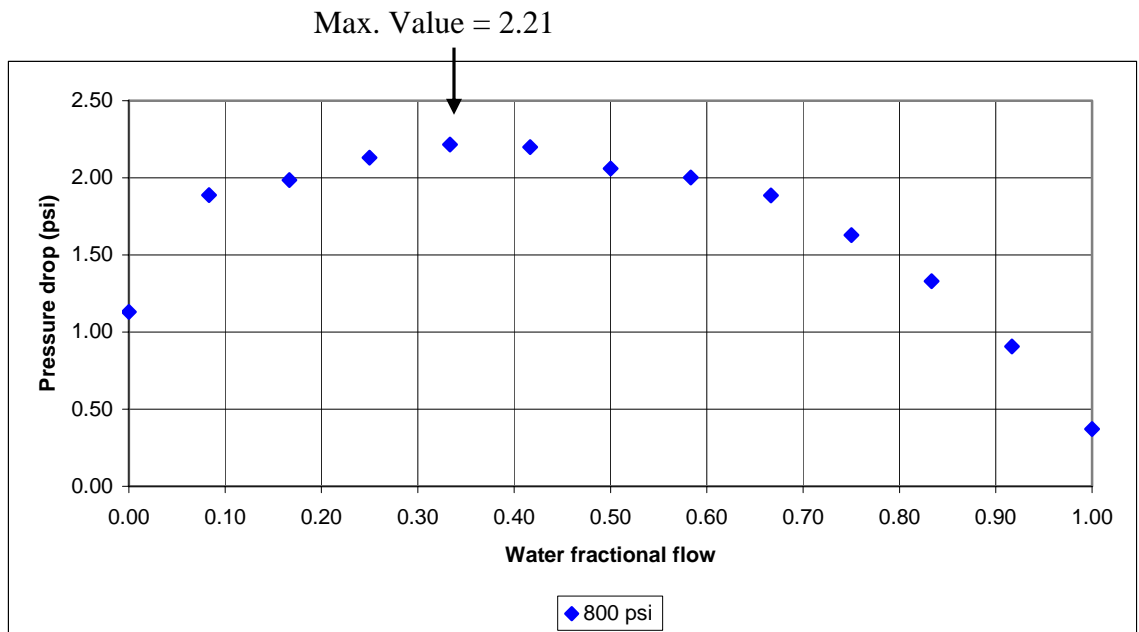


Figure 5.34: Pressure drop along the fracture for different fractional flow values.

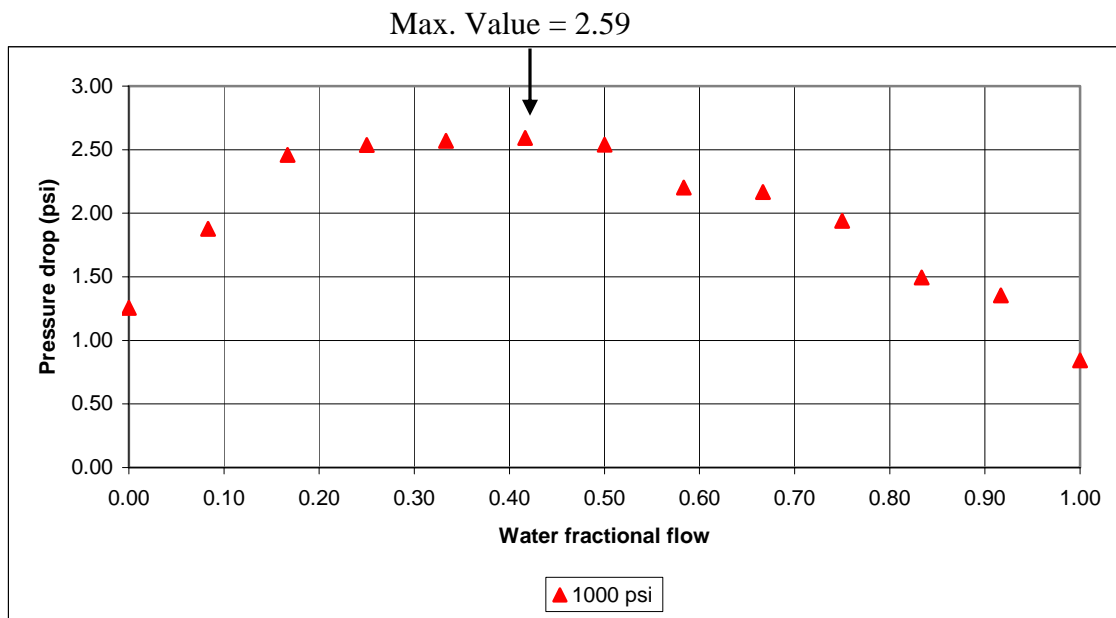


Figure 5.35: Pressure drop along the fracture vs fractional flow, 1000 psig confining pressure.

Figure 5.36 shows two pressure drop curves for two different confining pressures, 800 and 1000 psig. The difference between the two curves (Y axis) is due to the closure of the fracture aperture. For the two cases, 800 psig and 1000 psig confining pressure, a minimum pressure drop is observed for a fractional flow of 1.0. The fact that in both cases a higher pressure drop is observed for a $fw = 0.0$ than for $fw = 1.0$ would probably correspond not only to the viscosity ratios but also to the wettability of the system, the water being the wetting phase in this experiment.

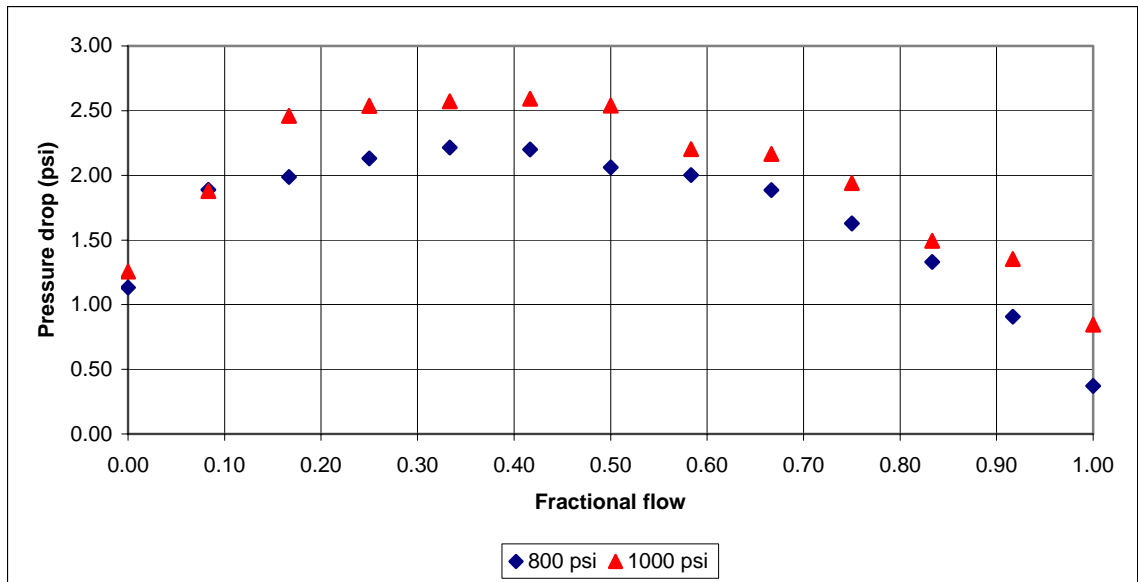


Figure 5.36: Pressure drop in the fracture vs fractional flow for 800 and 1000 psig.

5.3.2 Core # 2

To analyze the fracture topology (variability) effects, a second Berea Sandstone core was used for a fluid injection experiments. Different fractional flow conditions were applied from 0.0 to 1.0 and from 1.0 to 0.0. Figure 5.37 shows saturation dependency on the flow paths. At fractional flow lower than 0.5, hysteresis seems to be less than at high fractional flow values. Figure 5.38 presents a second set of fractional flow tests for the same rock sample, showing a consistency (repeatability) in the flow paths.

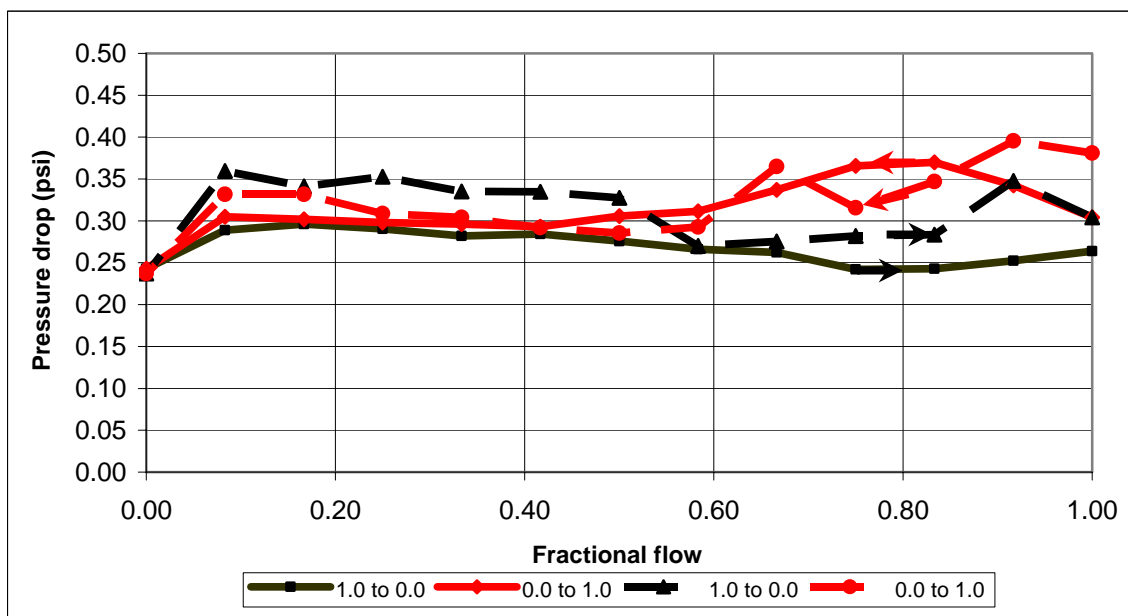


Figure 5.37: Pressure drop in the fracture vs fractional flow for 200 psig. Set # 1.

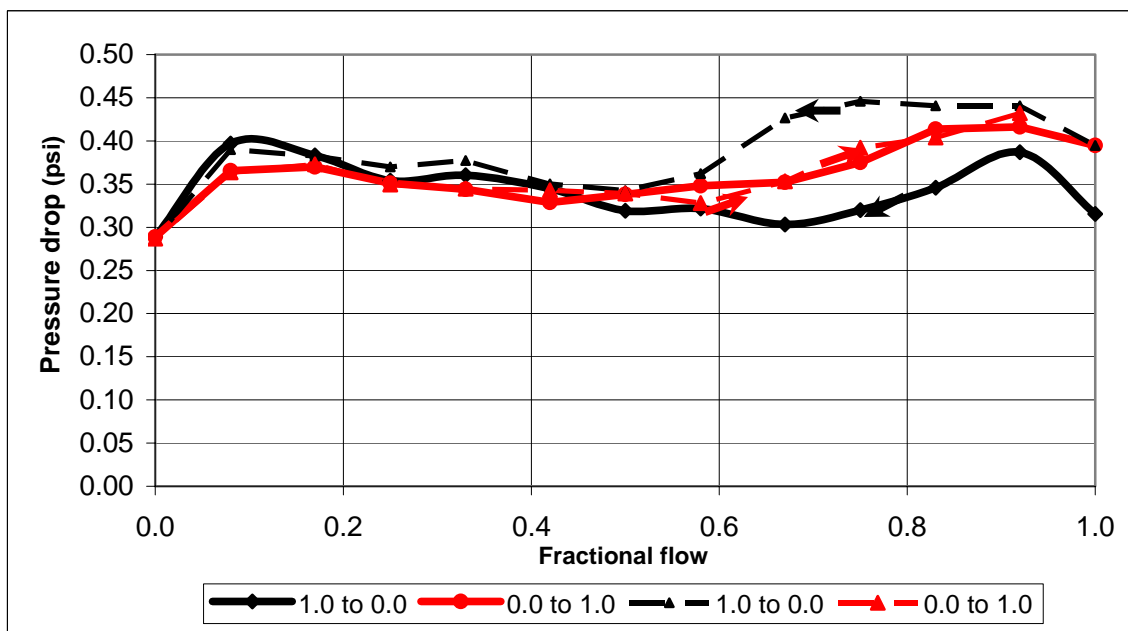


Figure 5.38: Pressure drop in the fracture vs fractional flow for 200 psig. Set # 2.

In order to maintain two phase flow injection into the fracture, the end points were not taken into consideration. The fractional flow changes were done after injecting 120 cc (10 min). However, in some cases the volume was higher (240 cc) based on the equilibrium of the pressure drop in the system.

5.3.3 Core # 3

Figure 5.39 shows the fractional flow behavior for another Berea Sandstone core. The pressure drop along the core presents a different shape than previous experiment. Figure 5.35 also highlights a critical point, at fractional flow equal to 0.5, where the pressure drop behavior increases as the fractional flow increases.

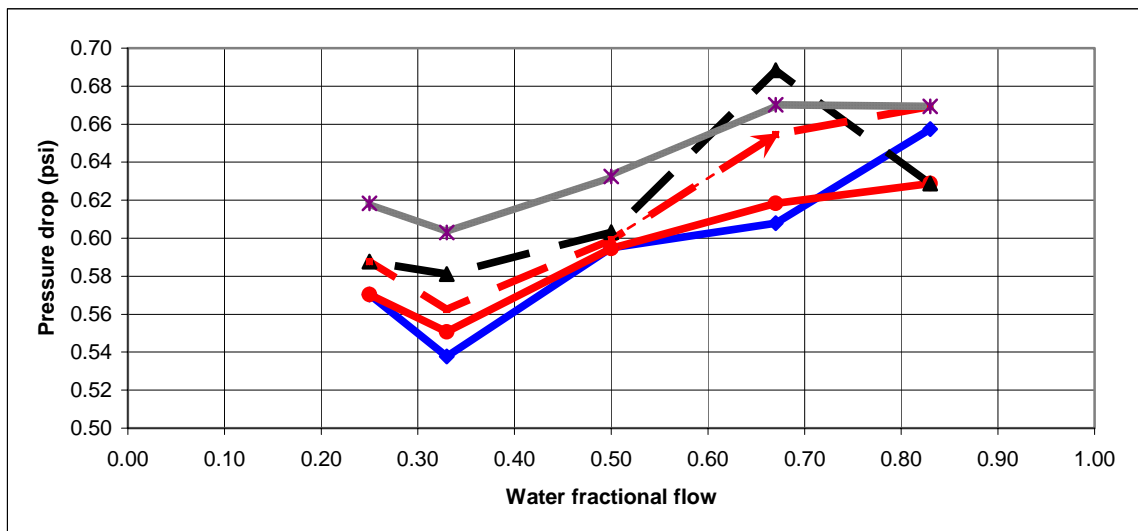


Figure 5.39: Pressure drop in the fracture vs fractional flow for a confining pressure equal to 800 psig.

Figure 5.40 shows the pressure drop in the fracture for the section of fractional flow from 0.25 to 0.5. A very repeatable behavior is observed for this section. The section of fractional flow from 0.5 to 0.83 presents a non repeatable behavior shown in Figure 5.41.

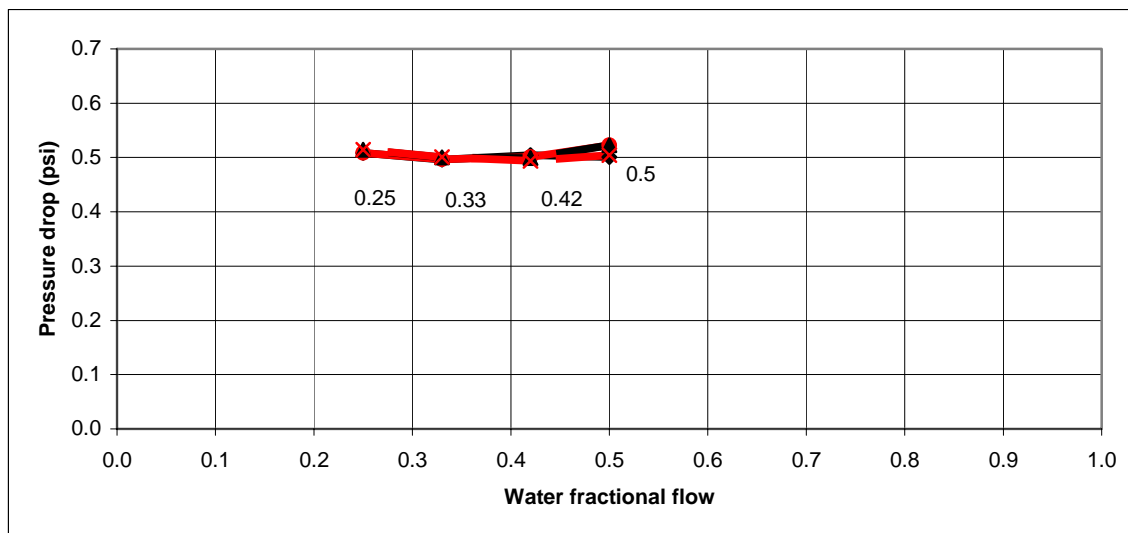


Figure 5.40: Fractional flow range: 0.25-0.50. 800 psig confining pressure.

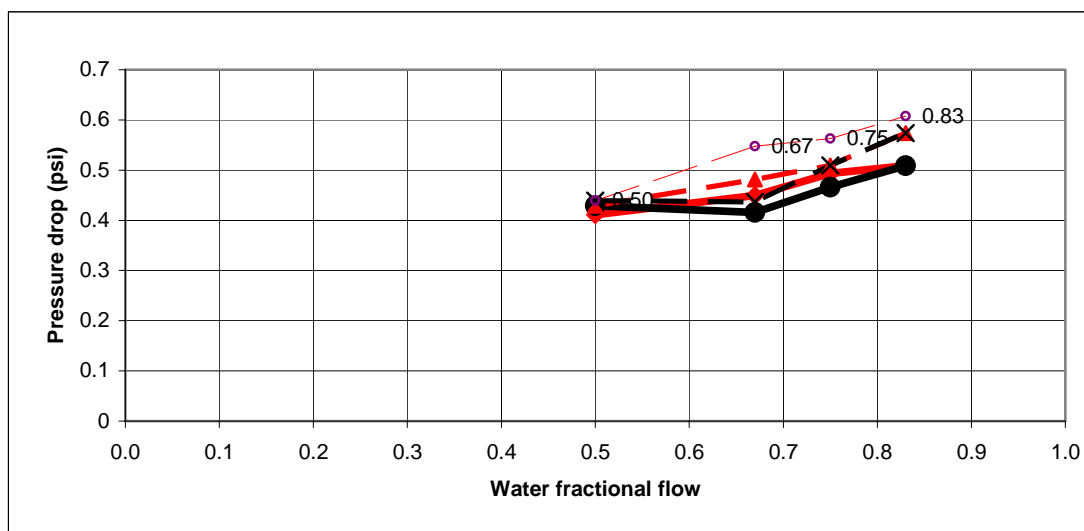


Figure 5.41: Fractional flow range: 0.50-0.83. 800 psig confining pressure.

5.3.4 Core # 4

The core (4) used for fluid flow shows different flow behavior under 500 psig confining pressure. With the increase in the fractional flow of water the pressure drop decreases. The confining pressure for this experiment is different from previous experiments (500 psig). Figure 5.42 shows the pressure drop in the fracture for different fractional flow at 500 psig confining pressure. The fracture topology for this core seems to be different from other cores as a consequence of the change in confining pressure, having an important effect on the flow patterns. So far, the flow analyses have been performed with no CT information. In future experiments CT that will be acquired to create saturation maps that will lead to explain the observations and hypotheses pretended in this study.

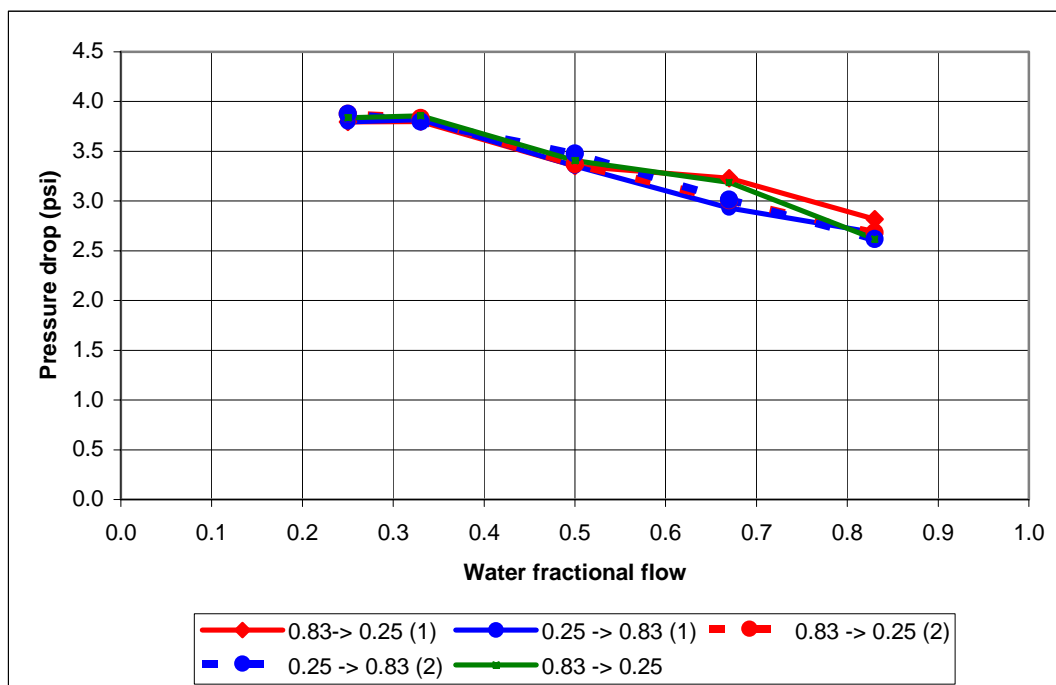


Figure 5.42: Pressure drop in the fracture vs fractional flow for 500 psig. Core # 4.

5.4 Multi-phase flow injection with CT data

A Berea sandstone core with a 2.5 cm diameter and 7 cm in length was used, where the bedding planes were axial and perpendicular to the fracture. Figure 5.43 (top) presents the final cropping for the matrix and fracture. A second reduction in size is necessary, given the computational memory need to analyze and manipulate the data. Figure 5.42 (bottom) shows the reduction to a rectangle of $x=22.1$, $y=3.12$ and $x=68.3$ mm in size.

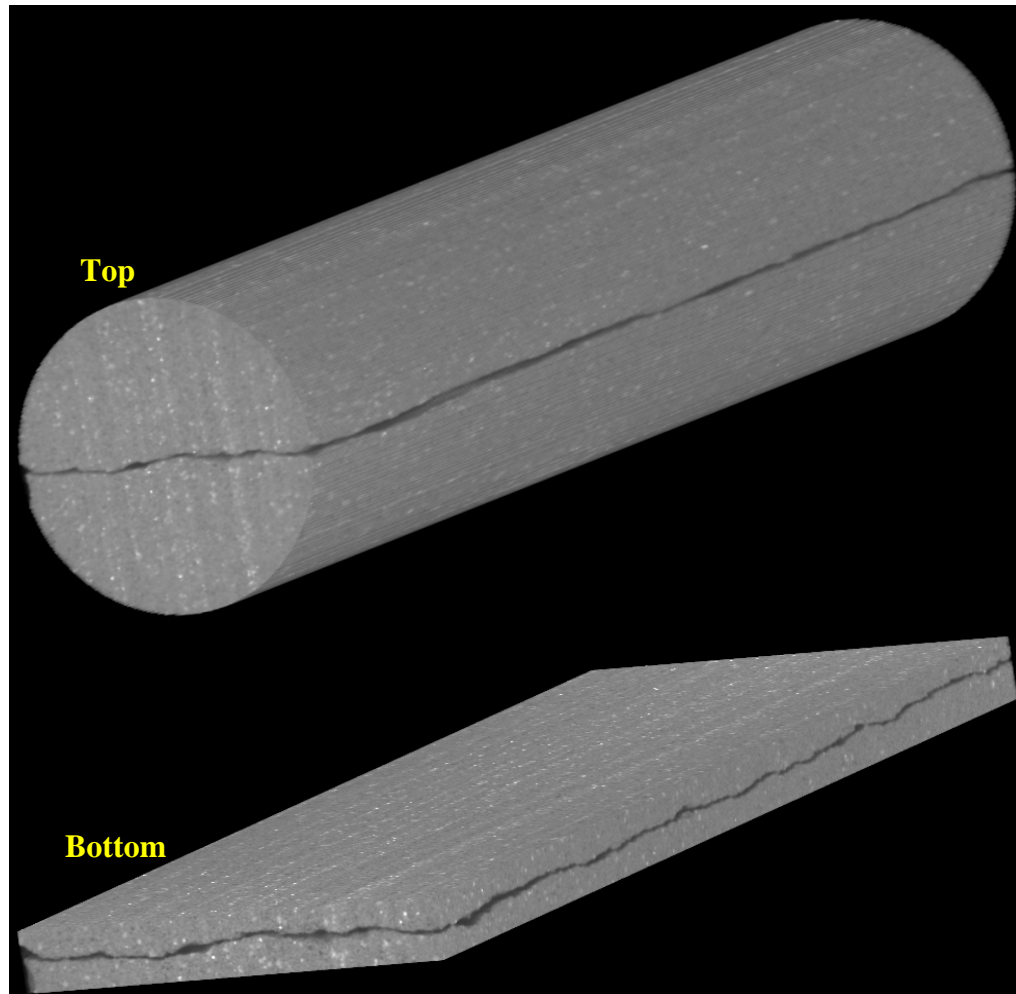


Figure 5.43: Fractured core (top), matrix reduction (bottom).

After vacuum-saturating the sample the absolute permeability to water was measured. Water was injected at different flow rates. Figure 5.44 shows the pressure drop along the fracture as a function of water injection rates.

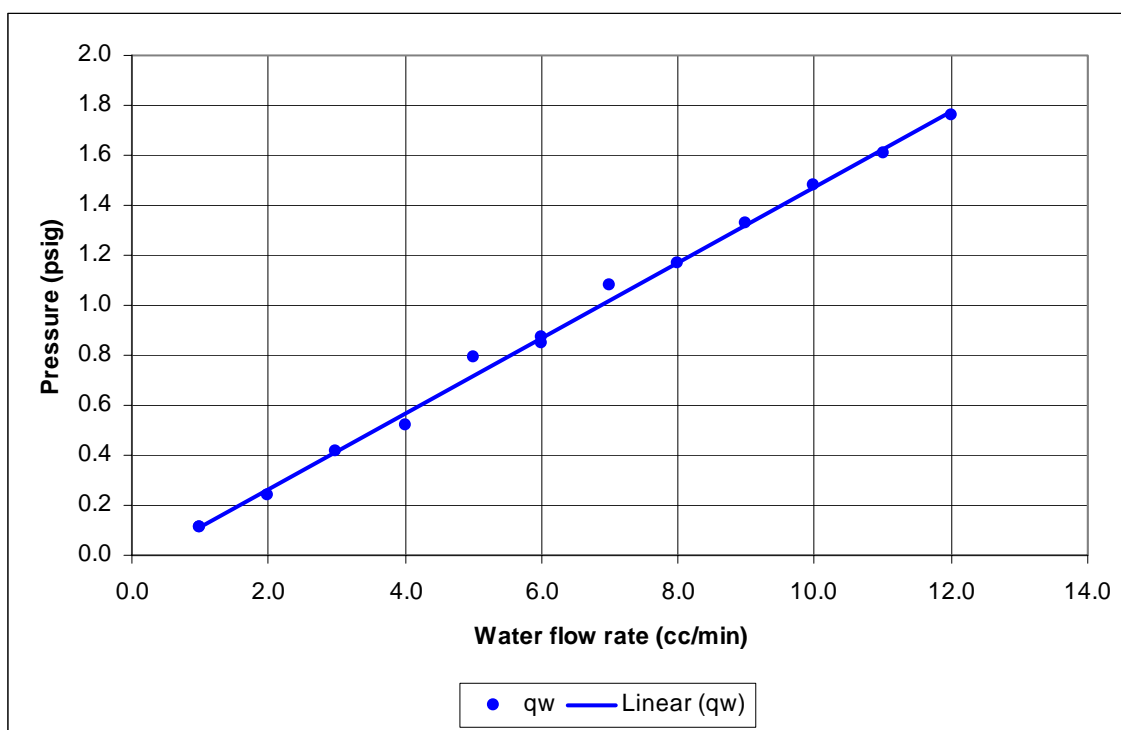


Figure 5.44: Pressure drop in the fracture for water injection.

A comparison of the viscosities of water and oil showed similarities in the order of magnitude for both fluids. Oil viscosity was 0.953 cP and water viscosity was 1.006 cP.

The parallel plate approximation, Witherspoon *et al.* (1980) has been used to determine the pressure drop along fracture during single phase flow. The cubic law equation is:

$$Q = \frac{\Delta p}{12\mu L} b^3 W \quad (5.5)$$

where μ is the dynamic viscosity of the fluid [$\text{ML}^{-1}\text{T}^{-1}$], L is length of the sample [L], W is the diameter of the sample [L], Q is the flow rate [L^3T^{-1}], Δp is the differential pressure [$\text{ML}^{-2}\text{T}^{-1}$], and b [L] is the equivalent hydraulic aperture of the fracture.

Equation 5.5 was used to predict the pressure drop along the fracture using the fracture average aperture obtained by CT data (0.264 mm). The computed pressure drop for a flow rate of 12 cc/min was equal to 0.0622 psi. The pressure drop along the fracture measured experimentally was 2.31 psi. The considerable difference between the estimated cubic law and the measured value (ratio of 37) is due the complicated topology of the fracture.

Figure 5.45 highlights the pressure drop in the fracture for different flow conditions. The 100 % water flow is shown by the blue circles. Oil was injected into the sample driving the water saturation to its residual value, S_{wirr} . At this condition a set of measurements were made shown by the red diamonds. Kerosene viscosity is close to water viscosity ($\mu_{wNai} = 1.006$ cP, $\mu_{Kero} = 0.953$ cP) resulting in a similar response to the 100 % water-saturated sample with a $k_{ro}(S_{wir}) = 0.62$. The water flow at residual oil saturation (green triangles) shows a reduction in water permeability, where $k_{rw}(S_{or}) = 0.306$.

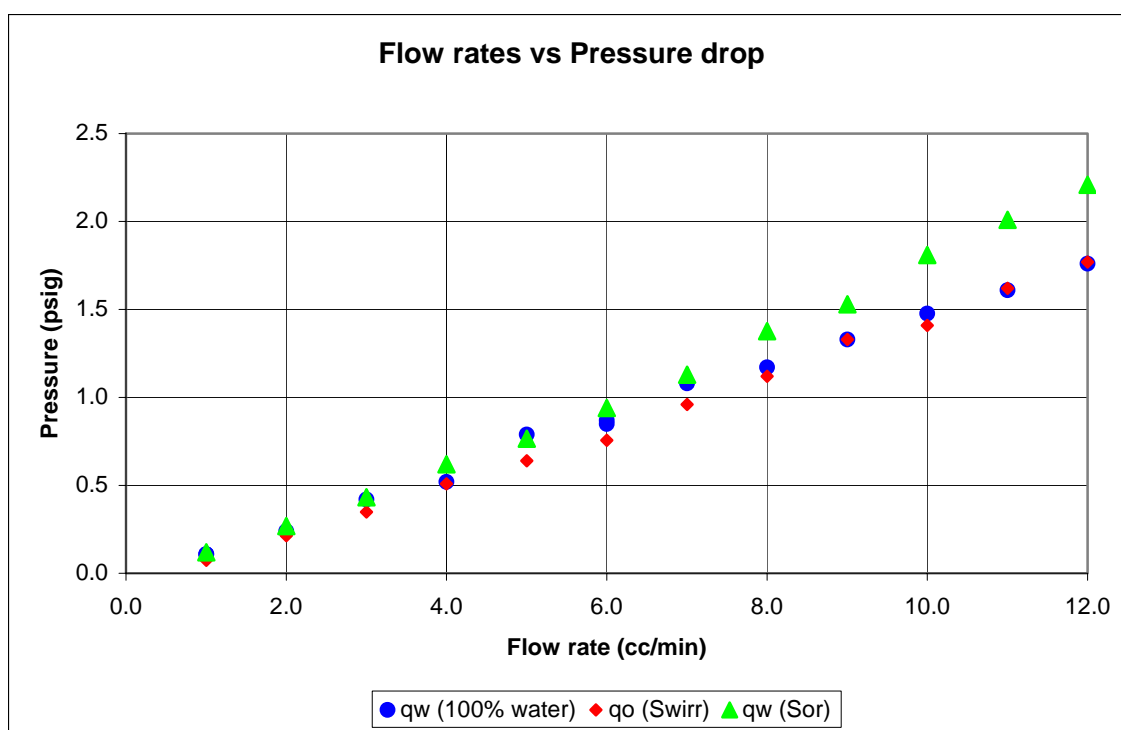


Figure 5.45: Water pressure drop in the fracture for different saturation conditions.

The relative permeabilities for the oil and water at S_{wirr} and S_{or} and of an intermediate point, were the core was under two phase flow ($f_w = 0.66$) are shown in Figure 5.46 shows.

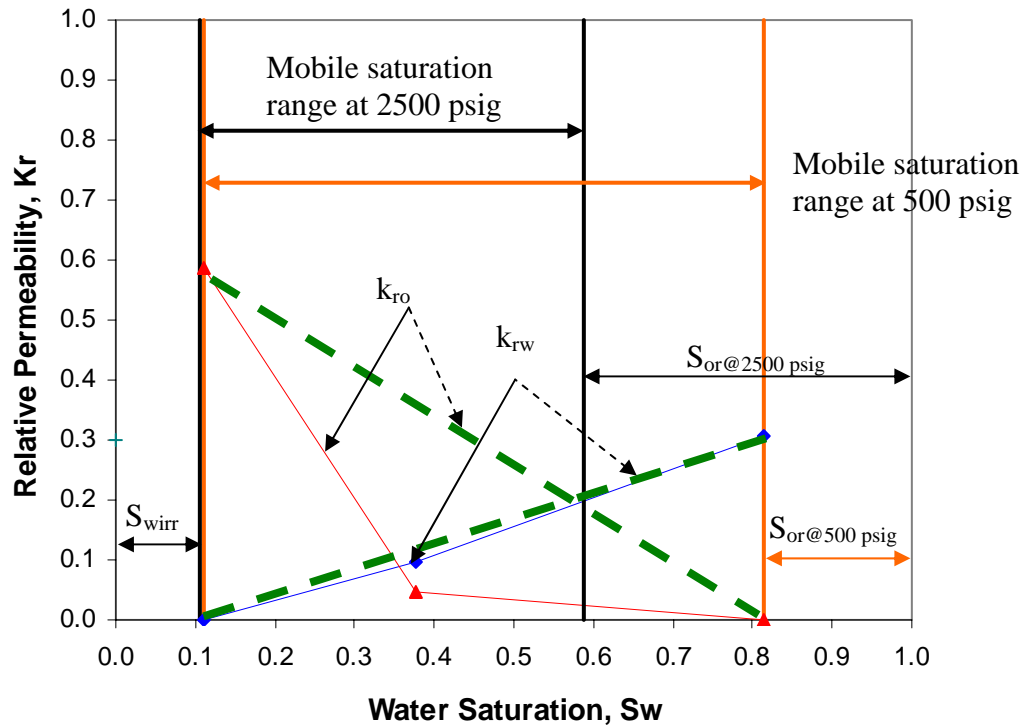


Figure 5.46: Relative permeabilities curve for a fractured system at 500 psig.

The green dash lines represent the x-shaped curves for relative permeabilities for oil and water, usually used for fractured systems. The blue and red lines represent the experimental relative permeability, for water and oil respectively. A significant deviation from the straight line is observed for the k_{ro} curve. The x-shaped curves over estimate the permeability of the non-wetting phase. The mobile range at this low press (500 psig) is about 70%. At 2500 confining pressure the mobile range saturation range was reduced to 48%.

To characterize and quantify the fracture volume a segmentation process is required. Figure 5.47 shows the changes of the fracture volume for different thresholds. For the dry fracture a threshold of 2400 was selected for a fracture volume of 0.376 cc (at 500 psig) where the change in volume with threshold is not highly stiff.

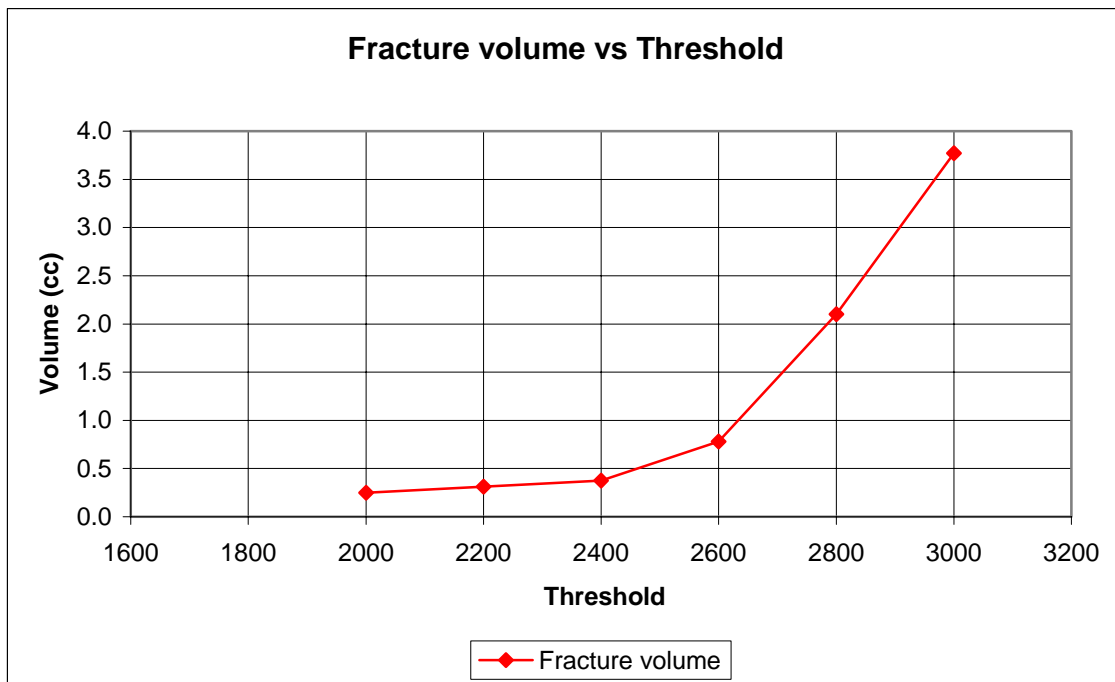


Figure 5.47: Fracture volume for different threshold numbers.

Figure 5.48 shows the results for the three dimensional fracture aperture with a fracture volume of 375.8 mm³. The black area represents the asperities (contact joints) in the system.

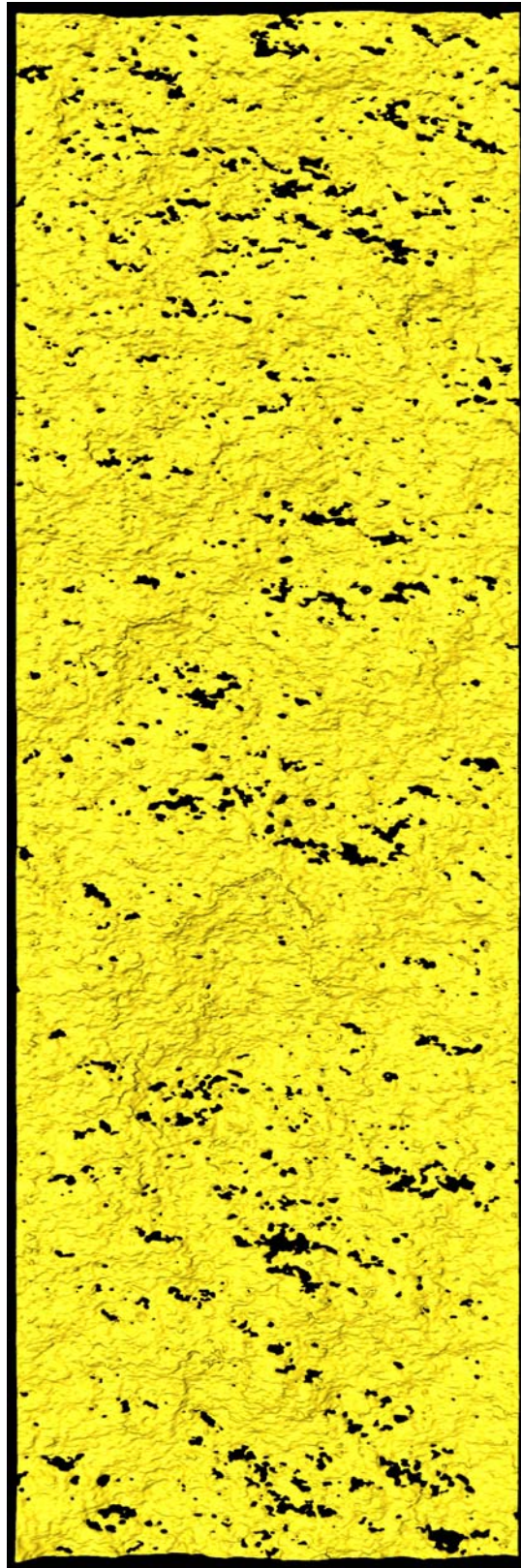


Figure 5.48: Three dimensional rendition of fracture asperities.

Figure 5.49 shows the fracture at residual water saturation, where the oil occupies most of the fracture volume. From left to right, dry fracture, oil phase and water phase are presented. The computed fracture residual water saturation ($S_{wirr,f}$) was 11%.

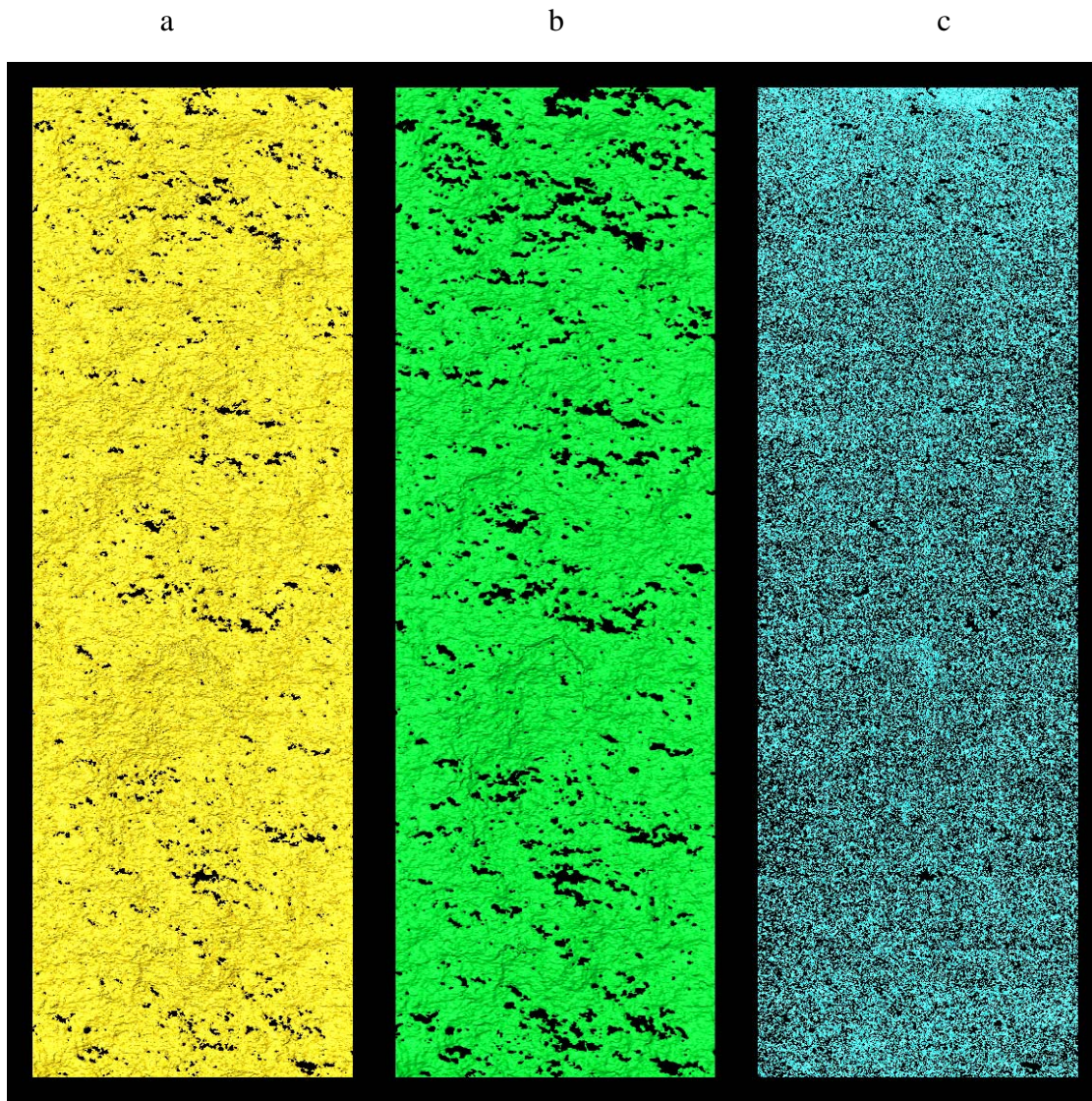


Figure 5.49: Fluids distribution maps: a: dry. b: oil. c: water at residual water saturation state.

After reaching and scanning the system at S_{wirr} the core was re-flooded with water to reach the residual oil saturation. Hundreds of fracture pore volumes were injected. At residual oil saturation the fluid saturations were computed: The corresponding saturations were $S_{or}=0.186$ and $S_w=0.814$. Figure 5.50 shows three dimensional rendition of the fracture. Fracture at dry condition (left), at residual oil (center) and the water (right) distribution. The oil is in discontinues isolated ganglias, and the water is the continuous phase.

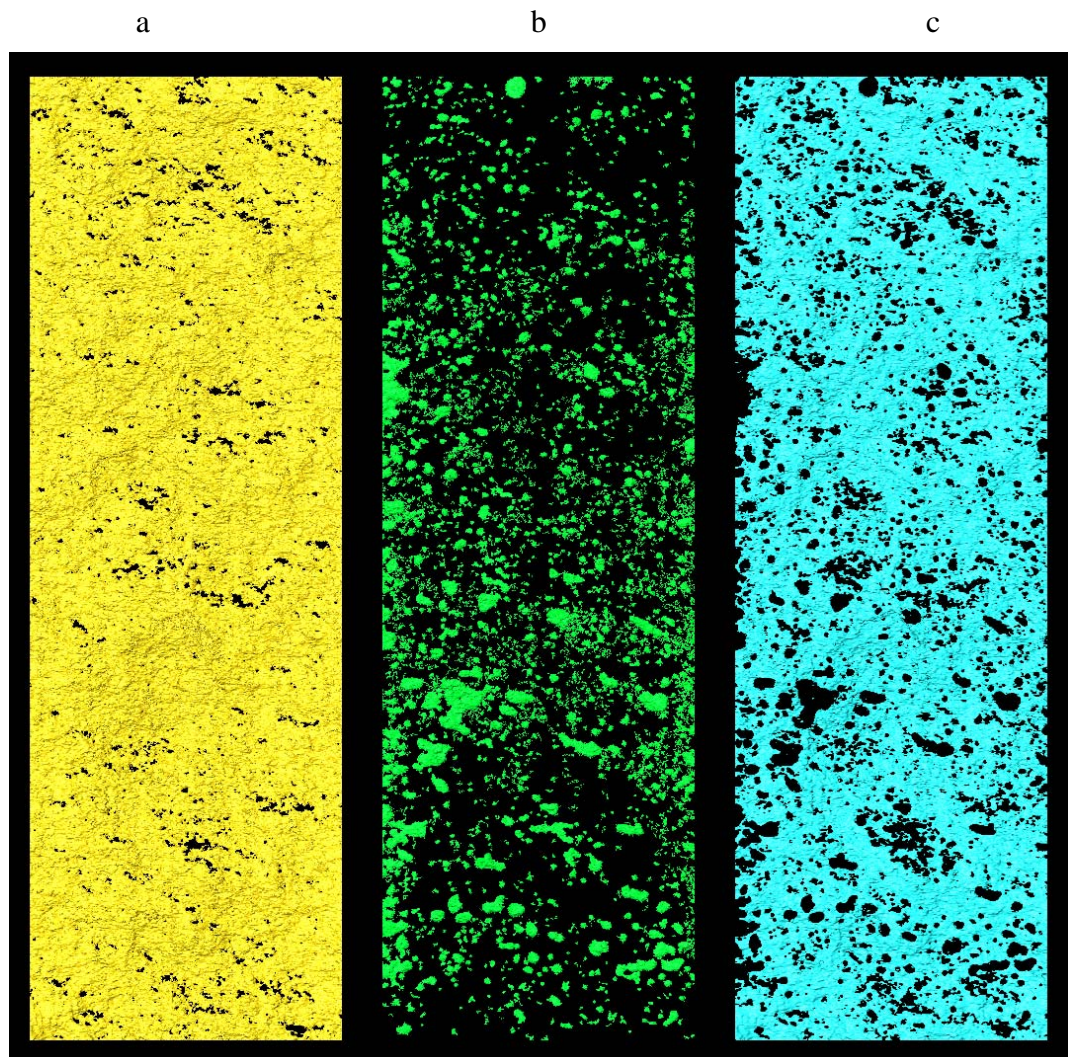


Figure 5.50: Fluids distribution maps: a: dry. b: Residual oil. c: Water

5.4.1 Fractional flow

After reaching residual oil saturation, different fractional flow injection sequences were done in order to establish possible trends. Figure 5.51 shows the pressure drop against fractional flow diagrams. The first path of fractional flow was done starting at fractional flow (water) equal 1.0 moving towards fractional flow equal zero. The total flow rate of 12 cc/min was used for the first flow test. The four traverses of the fractional flow range exhibit increase in pressure drop per a fixes f_w value. This indicates a strong dependency of the conductivity of the fracture on drainage or imbibition process and a changing saturation distribution with time.

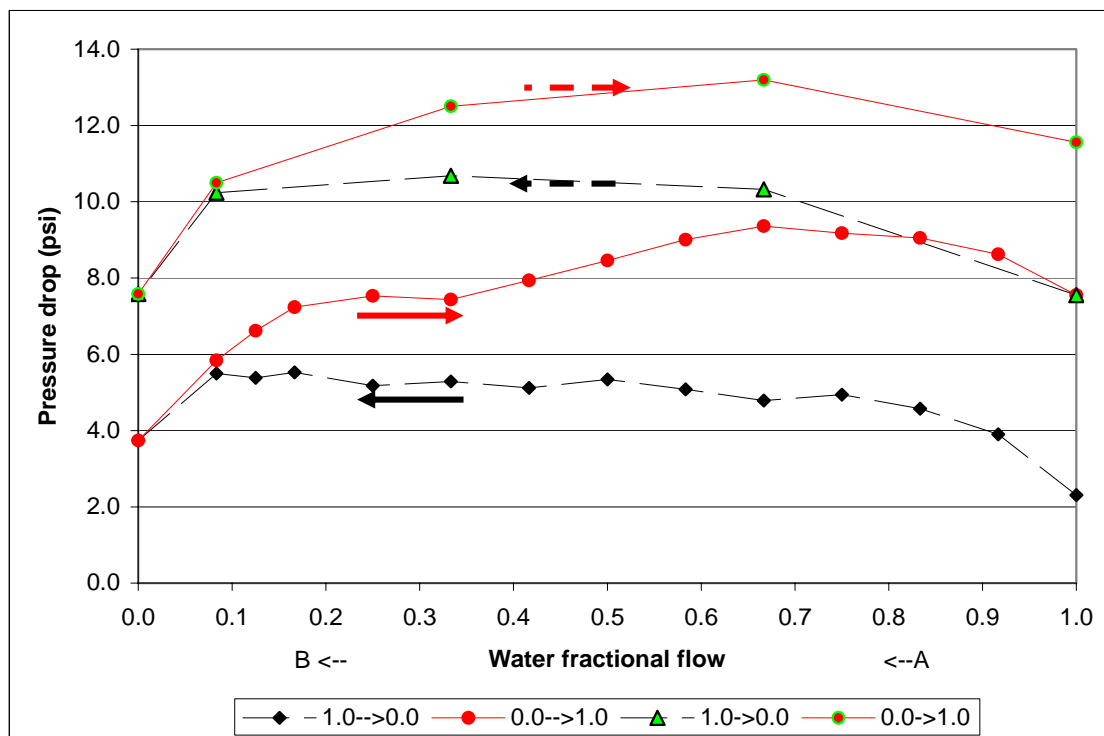


Figure 5.51: Pressure drop as function of fractional flow: two drainage and imbibitions cycles.

Figure 5.52 shows different loops where the flow injection was stopped as consequence of the high pressure drop. The maximum allowable pressure drop was 18 psig. A build up in pressure drop in the fracture was consecutively observed for different fractional flows (bottom to top). However, when the flow was reversed (top-bottom) the pressure drop in the fracture dropped to its original value. When the flow direction was reestablished (bottom-top) a new build up was produced. Scans of the injection and production ends showed that there was no buildup of water or oil and that the end connectors were not responsible for the cyclic nature of the pressure drop along the fracture. The entire fracture was scanned at low pressure drop and high pressure drop in order to find the fluids saturation under both conditions. Figure 5.53 shows in a three-dimensional reconstruction of the oil and water in the fracture for the low pressure drop condition.

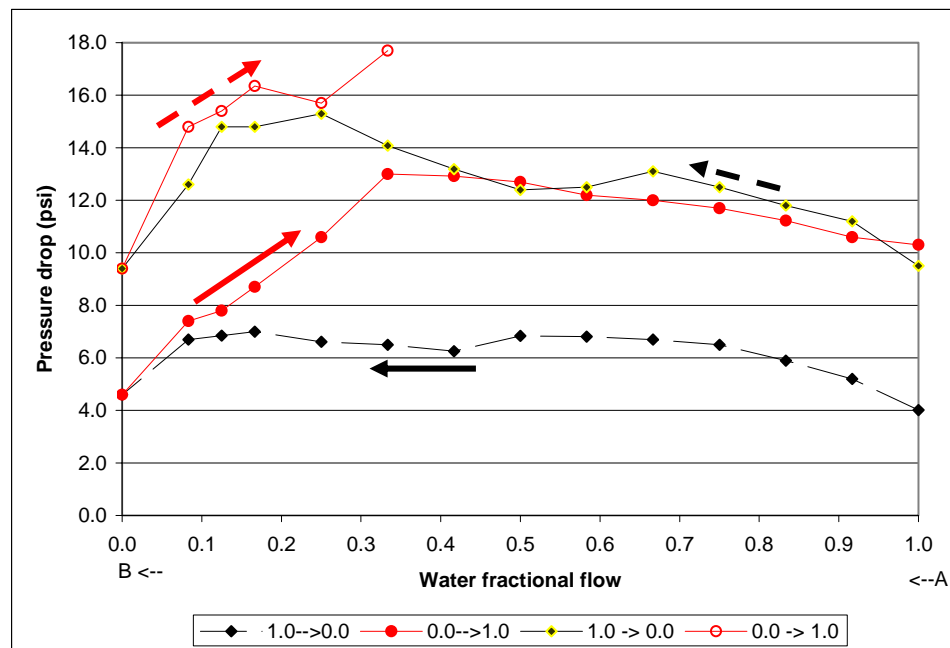


Figure 5.52: Pressure drop in the fracture for different fractional flow. $q_{\text{total}} = 12 \text{ cc/min}$.

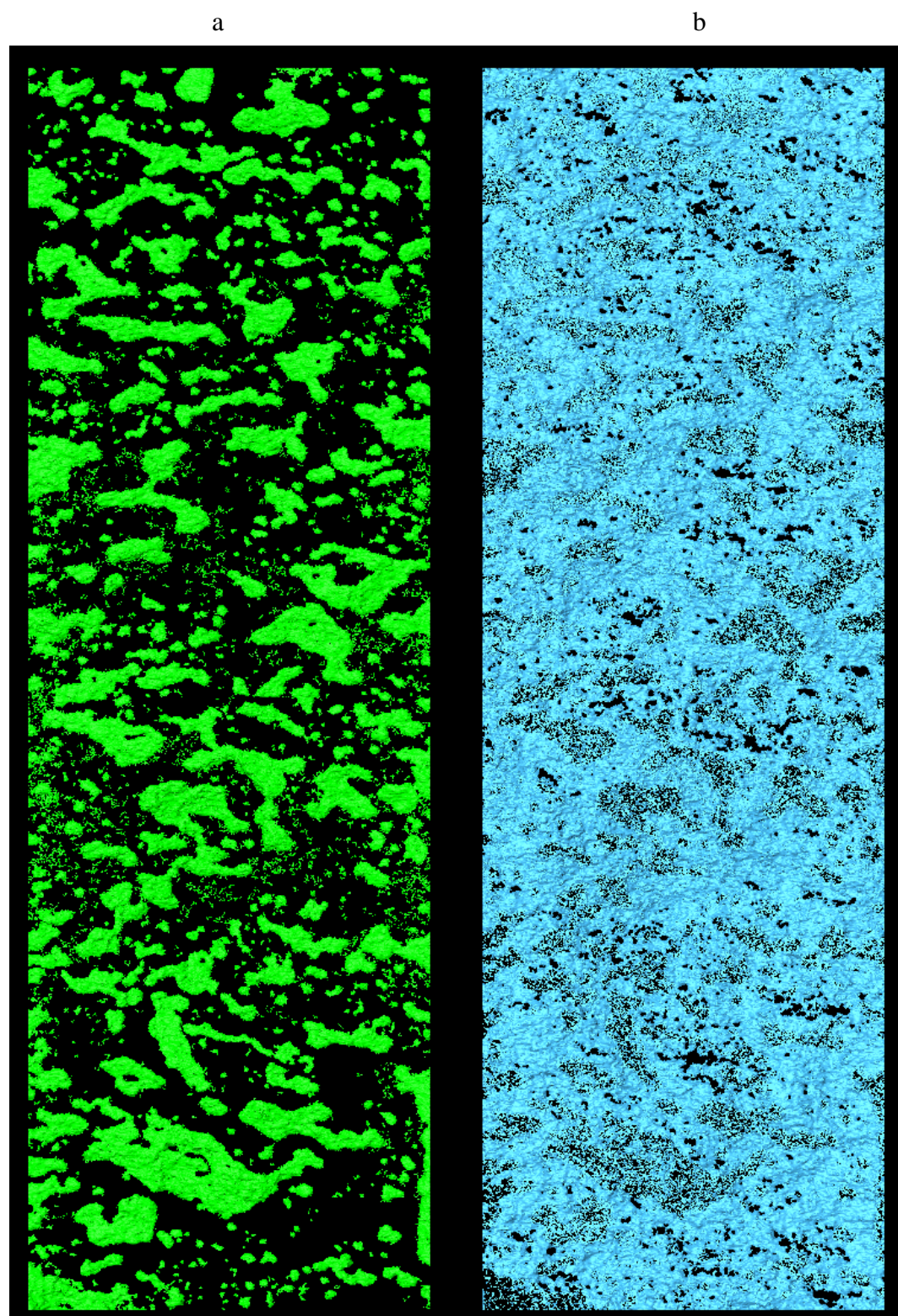


Figure 5.53: Fluids distribution in the fracture at low pressure drop. a: Oil b: water.

The over all fluid saturations were 38.6 (S_{of}) and 61.4% (S_{wf}) for oil and water respectively. An average saturation profile along the fracture is shown in Figure 5.54. The total volume of oil in the system for the low pressure drop was 145 mm³. The minimum and maximum oil saturation (cross sectional) values in the fracture were 13.1% and 63.3%, respectively. Different non-connected oil regions are shown in Figure 5.55, where it is also highlighted the largest oil globule with a value of 9.3 mm³.

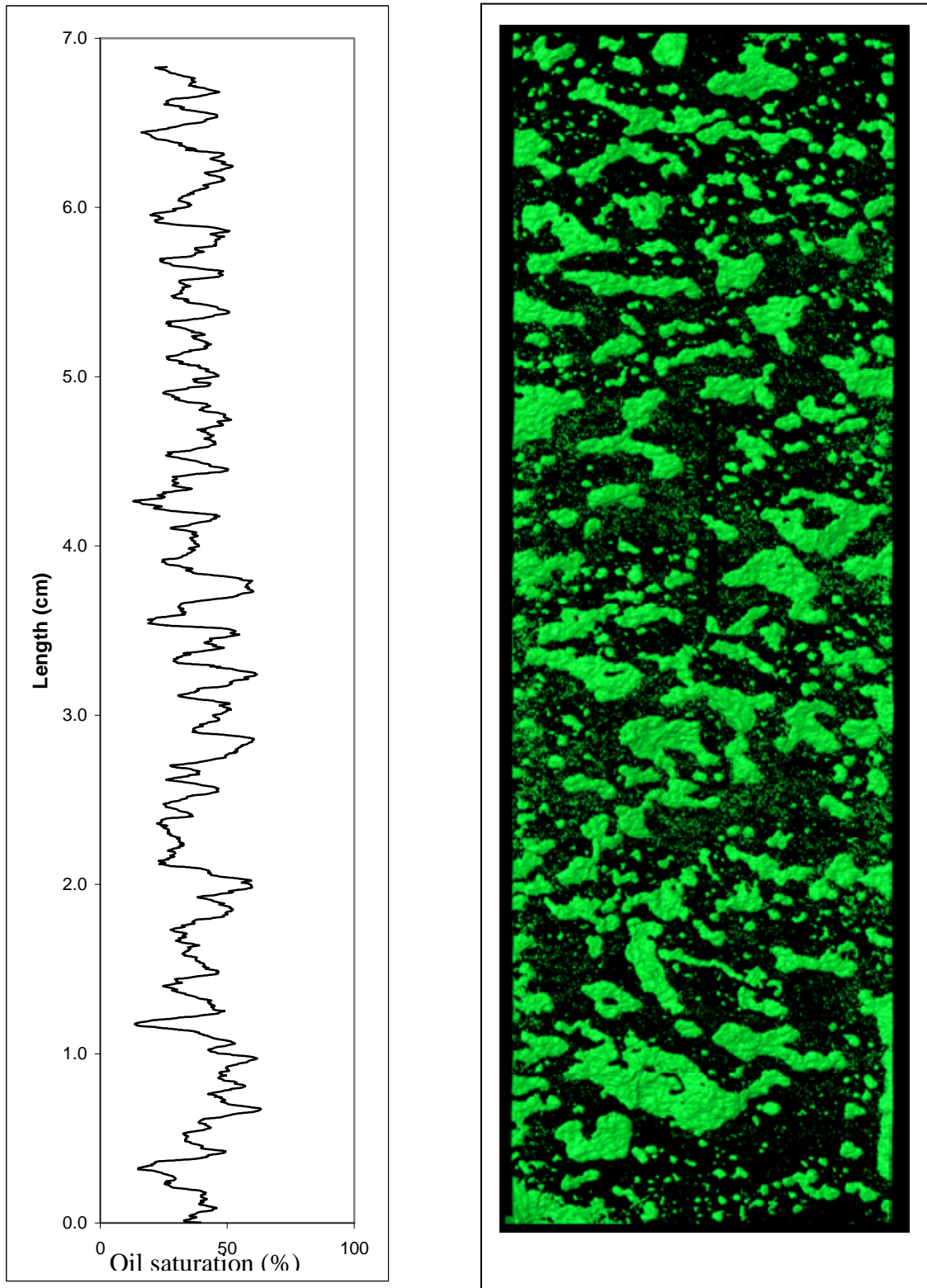


Figure 5.54: Oil saturation profile for the low pressure drop condition (left). Three-dimensional distribution of oil in the fracture (right).

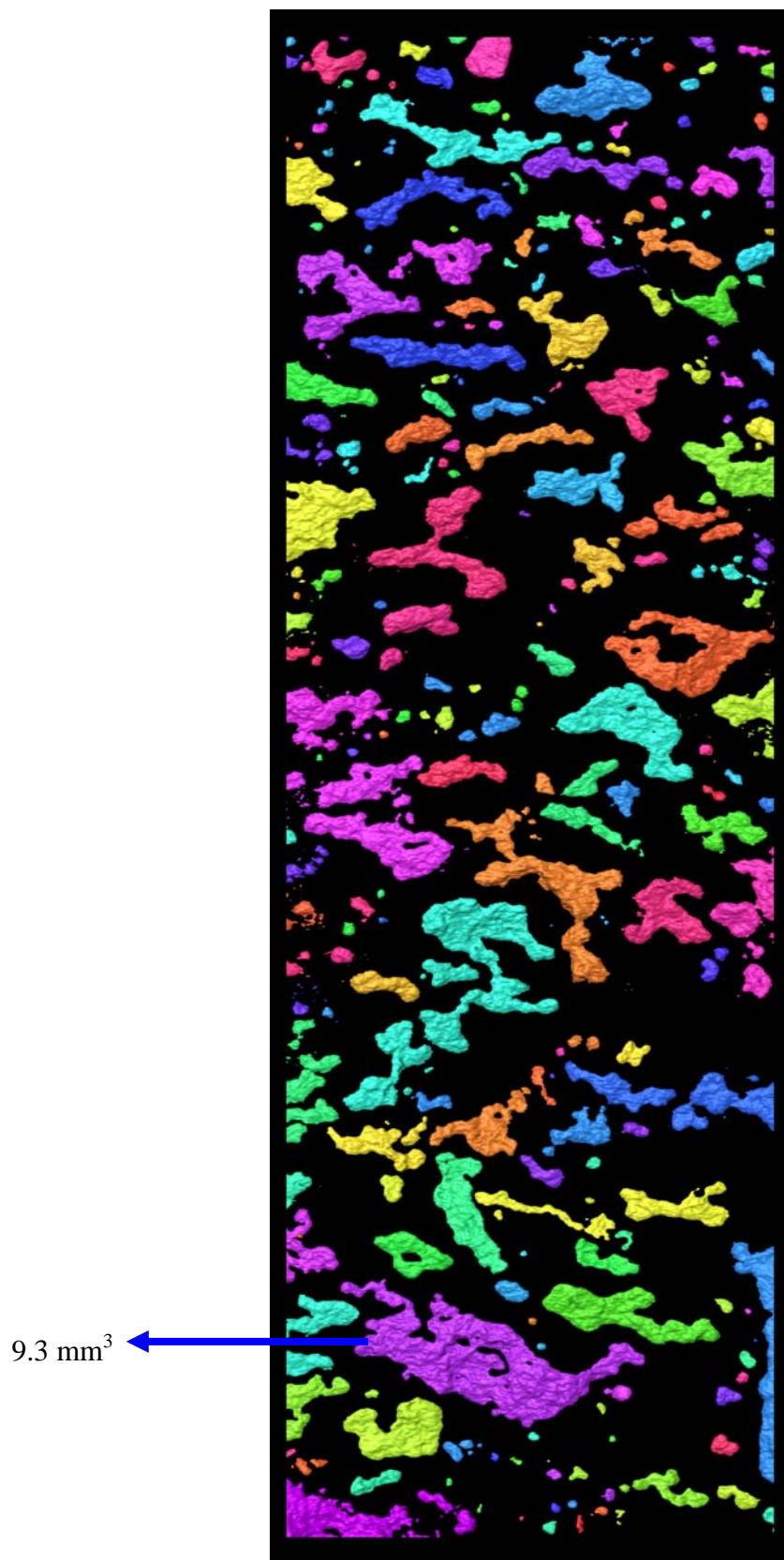


Figure 5.55: Disconnected oil globules in the fracture at low pressure drop condition.

A total of 240 independent oil bodies were identified. Figure 5.56 presents the distribution of the oil bodies, where the left part of the graph is affected by the limitation of the x-ray system to detect small volumes at the current resolution (26 microns). Most of the oil ganglias fall in the range between 0.01 and 0.09 mm³.

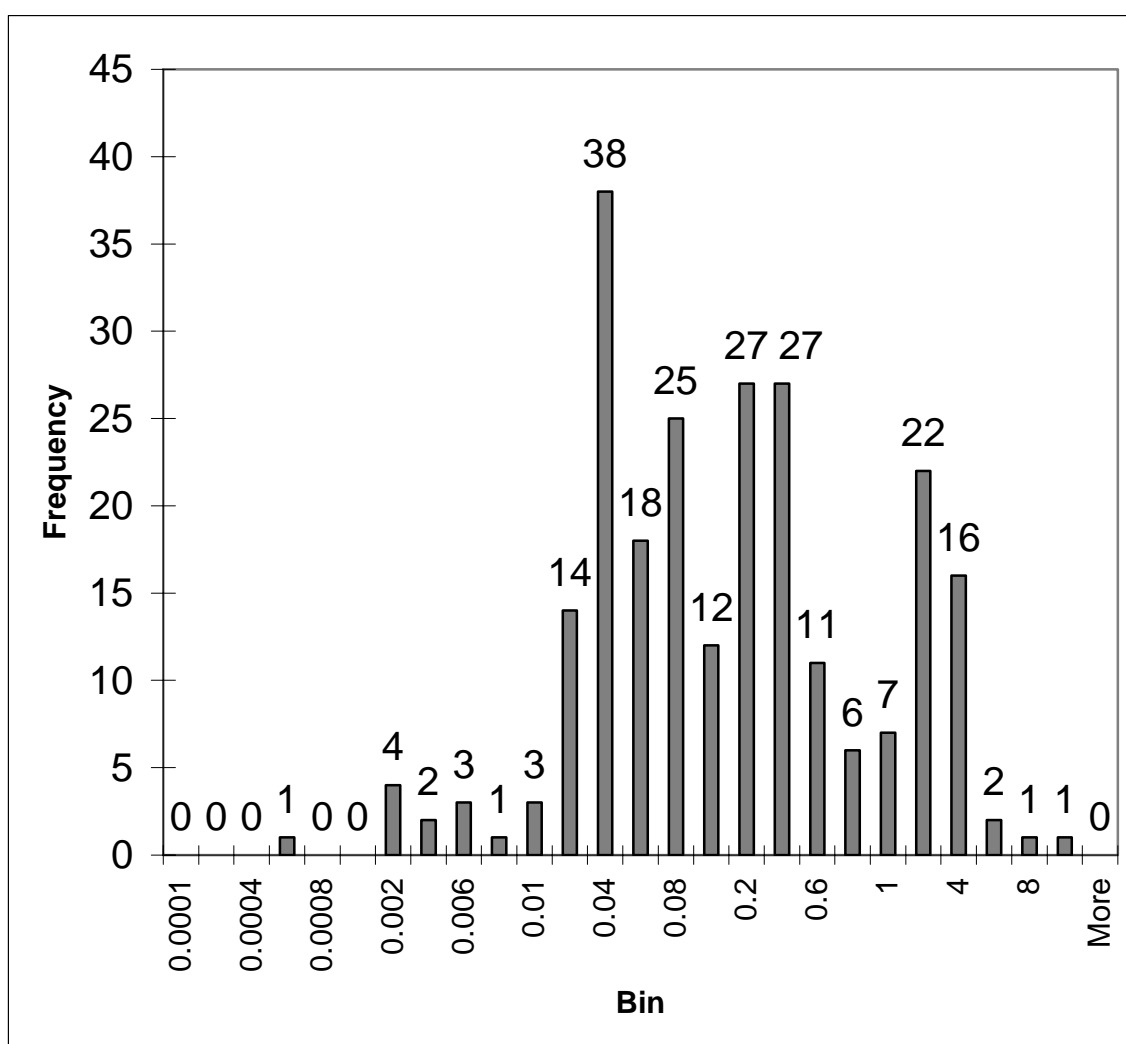


Figure 5.56: Oil feducias distribution at low pressure drop.

The saturation structure during the two-phase flow was not always stable. Figure 5.57 shows a sudden change in pressure drop that occurred at the end of an imbibition cycle during a steady injection. This significant loose in pressure drop could be produced by the displacement of oil globules (snap-off) in the fracture, and it was not possible to document it given that the CT time acquisition is longer than time in which this event occurred.

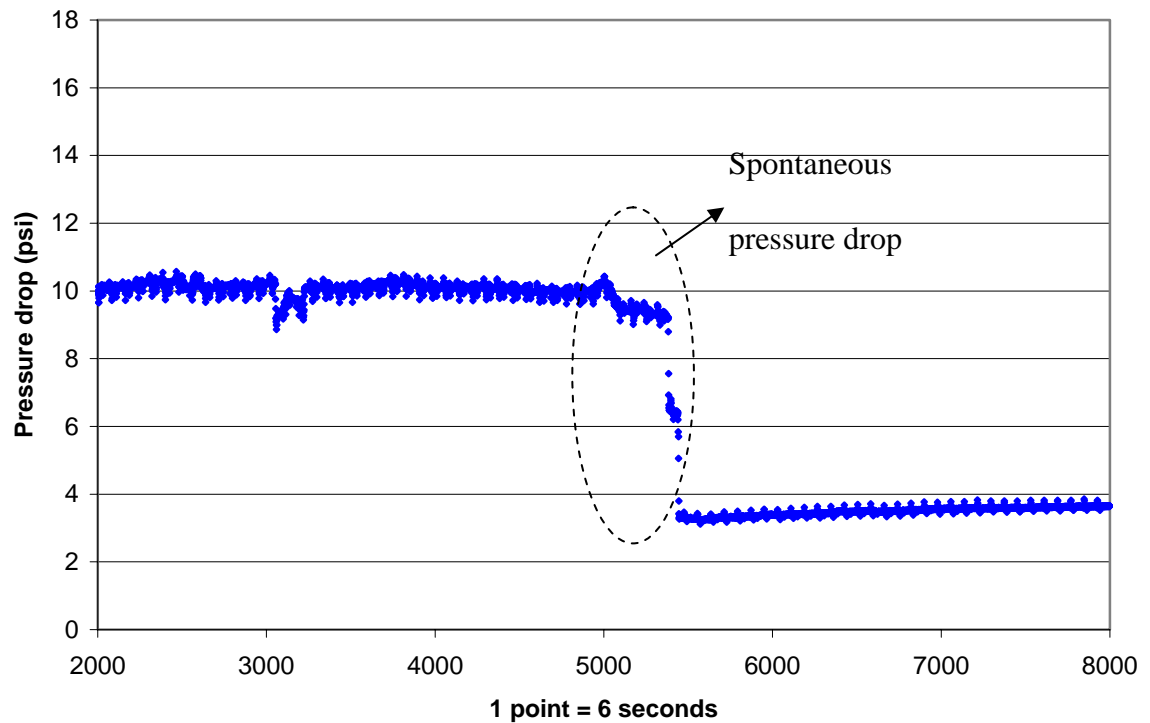


Figure 5.57: Fracture pressure drop during different fractional flows including a spontaneous pressure change.

Figure 5.58 shows the saturation profile (left) for the fracture at high pressure drop after different fractional flow cycles. The right part of Figure 5.58 shows a three dimensional image of how the oil is distributed in the fracture. The volume of oil in the fracture is equal to 0.142 cc, and is similar to the value computed in the low pressure drop system (0.145 cc).

The over all computed fluid saturation were 37.8 (S_{of}) and 62.2% (S_{wf}) for oil and water respectively. Table 5.6 shows a comparison of the fracture saturation for both cases, low and high pressure drop. The volumes of oil and water in the fracture are similar. However, there are few regions where the non-wetting phase (oil) seems to have a higher local saturation.

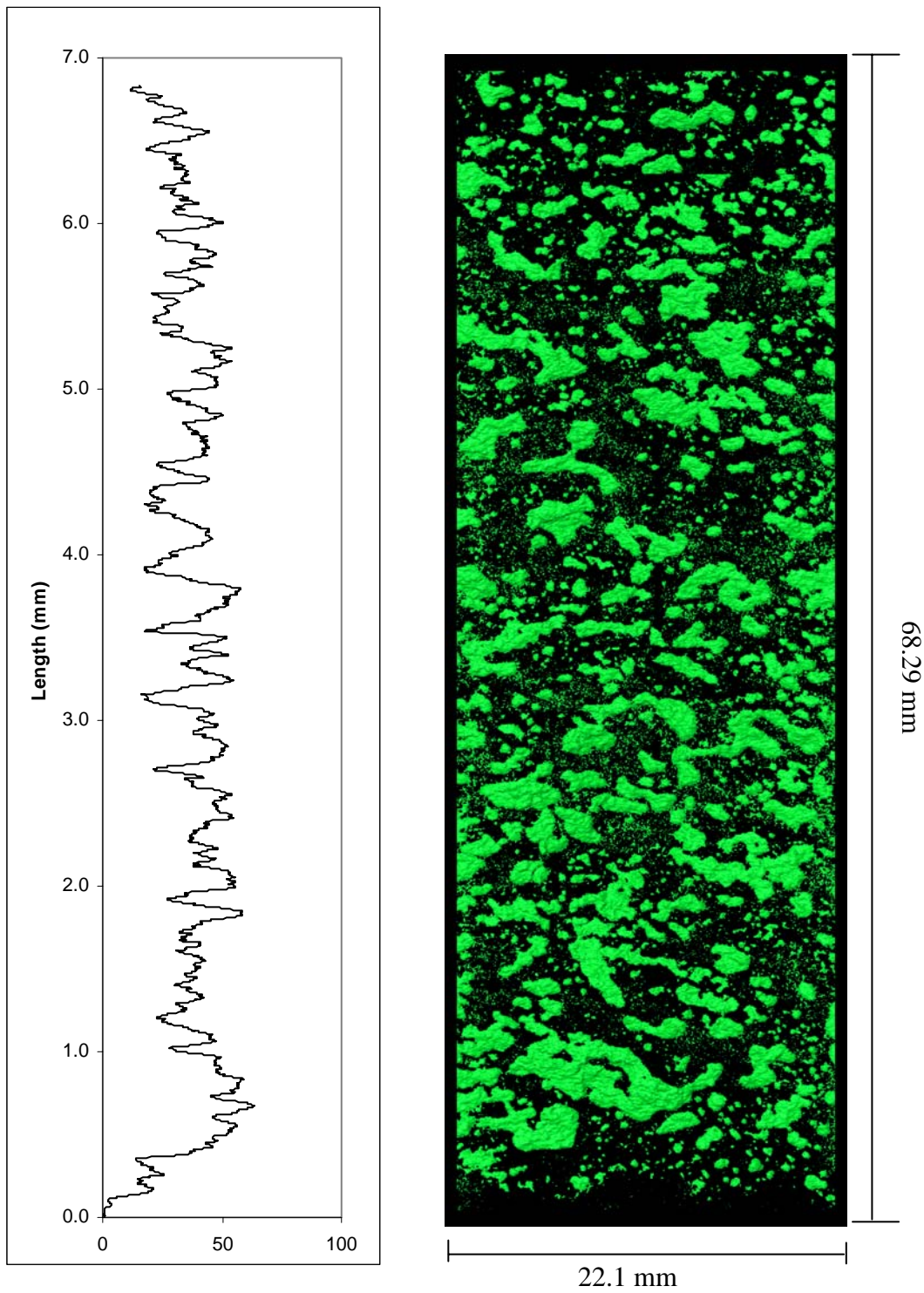


Figure 5.58: Oil saturation profile for the high pressure drop condition (left). Three-dimensional distribution of oil in the fracture (right).

Table 5.6: Fluid fracture saturation comparison at high and low pressure

Pressure drop Δp	Sof (%)	Swf (%)
Low	38.6	61.4
Hi	37.8	62.2

Figure 5.59 shows the large oil globule at the two pressure drop conditions. This figure shows that although the overall saturation is about the same (Table 5.6) the distribution of the fluids is significantly different. The red ellipse highlights a specific region for comparison. The yellow connected oil globule on the left (high pressure drop) is much smaller in the low pressure drop case. This “yellow” globule impedes fluid flow and increases the pressure drop along the fracture.

Figure 5.60 shows a section, between 2 and 3 cm (axially) along the fracture where the oil saturation of the high pressure drop case is significant higher than the low pressure drop case.

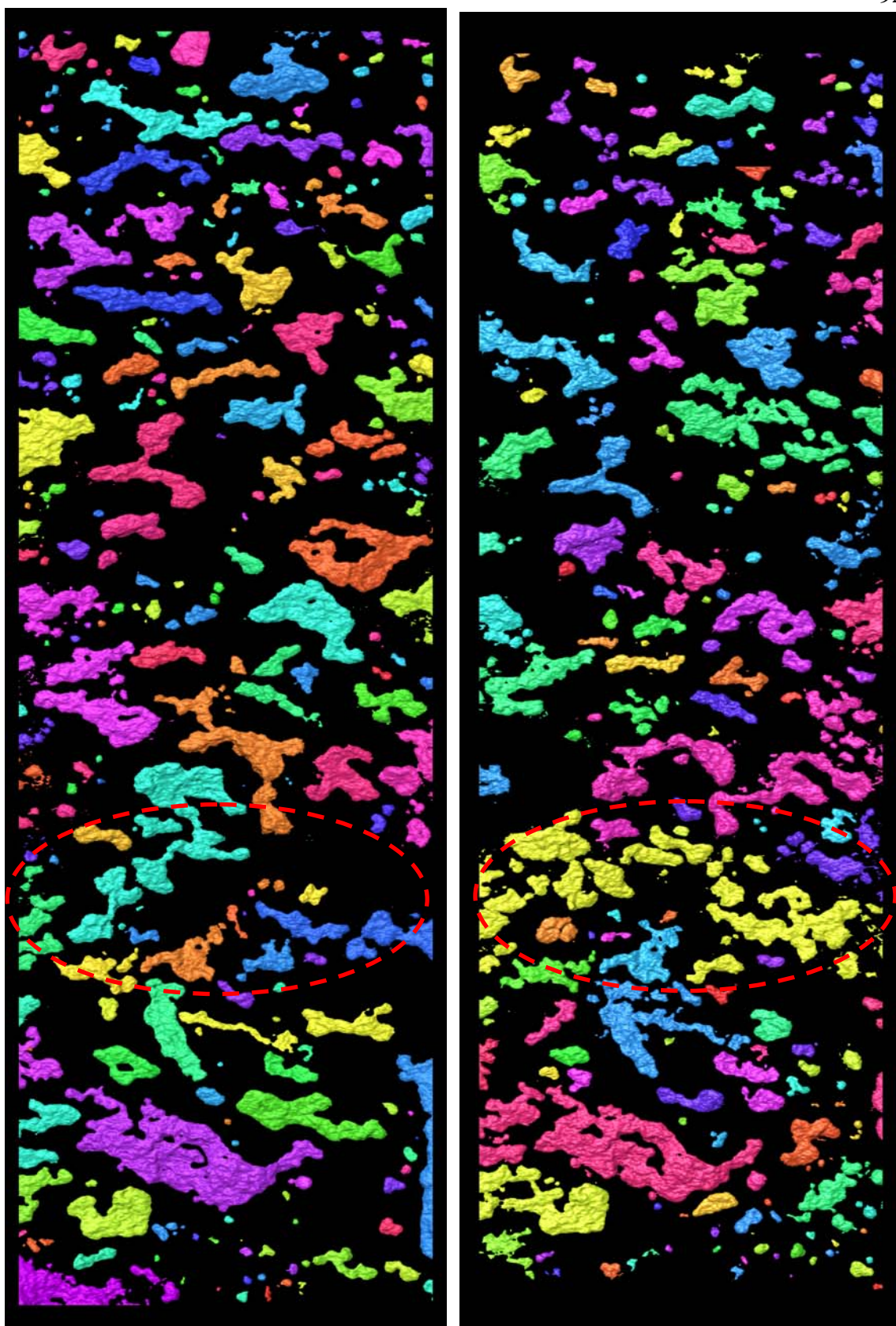


Figure 5.59: Oil distribution in the fracture. Left: Low pressure drop. Right: high pressure drop.

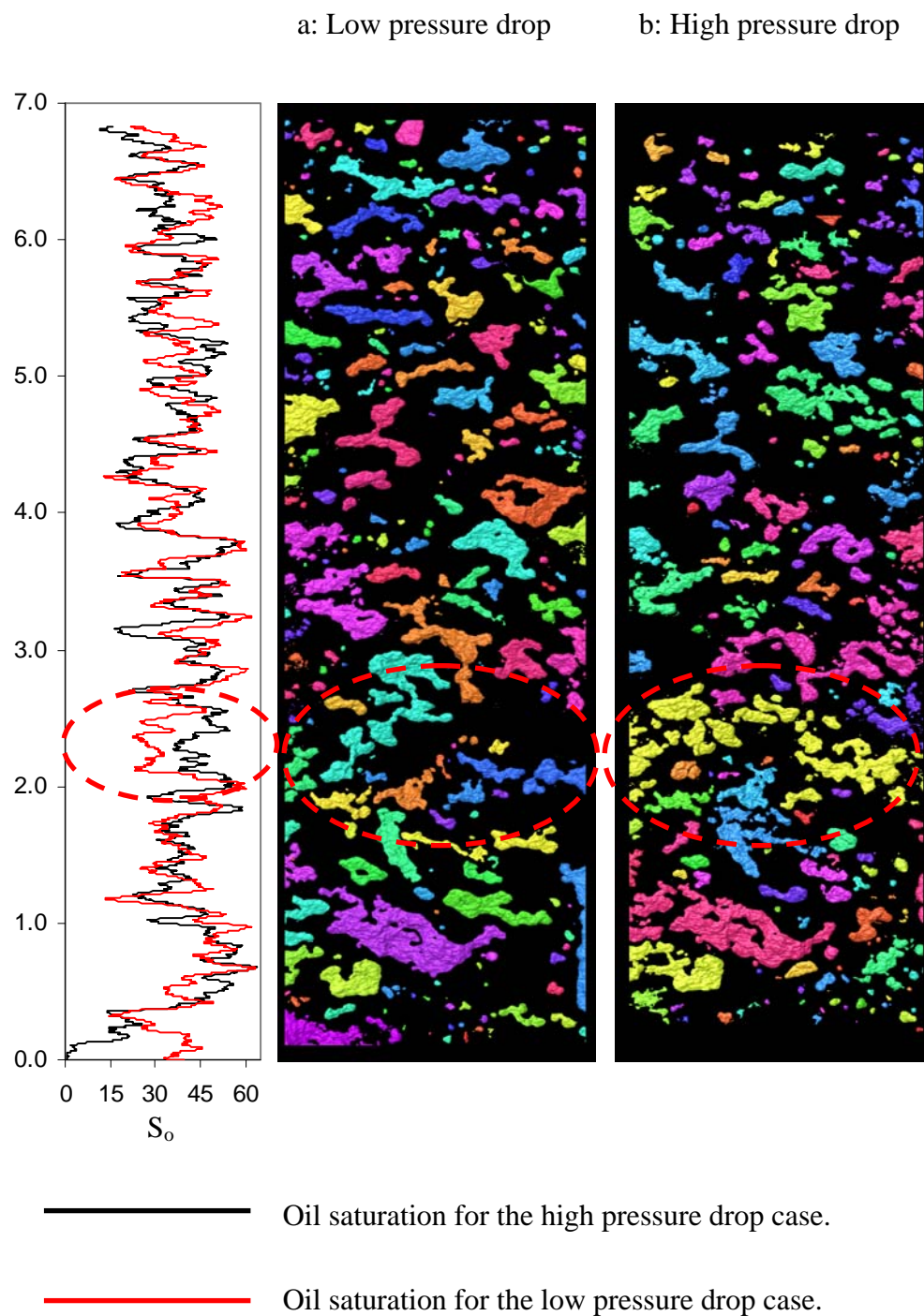


Figure 5.60: Oil distribution low pressure drop (a). Oil distribution high pressure drop (b).

The previous figures demonstrate that the over all fluid saturations in the fracture are almost identical for high and low pressure drop. However, it is the distribution of the non wetting phase (oil) that creates a difference in the pressure drop. The low conductivity of flow in the fracture forces the fluids to flow through the matrix, thus, increasing the pressure drop of the system. In order to analyze and compare the fracture conductivity over the Berea sandstone a non-fractured “neighbor” core was used to inject fluids and compare the pressure drops. Figure 5.61 shows the pressure drop for a fracture and a un-fracture core for different flow rates. A significant pressure drop in the presence of residual oil shows the impact of the non wetting phase.

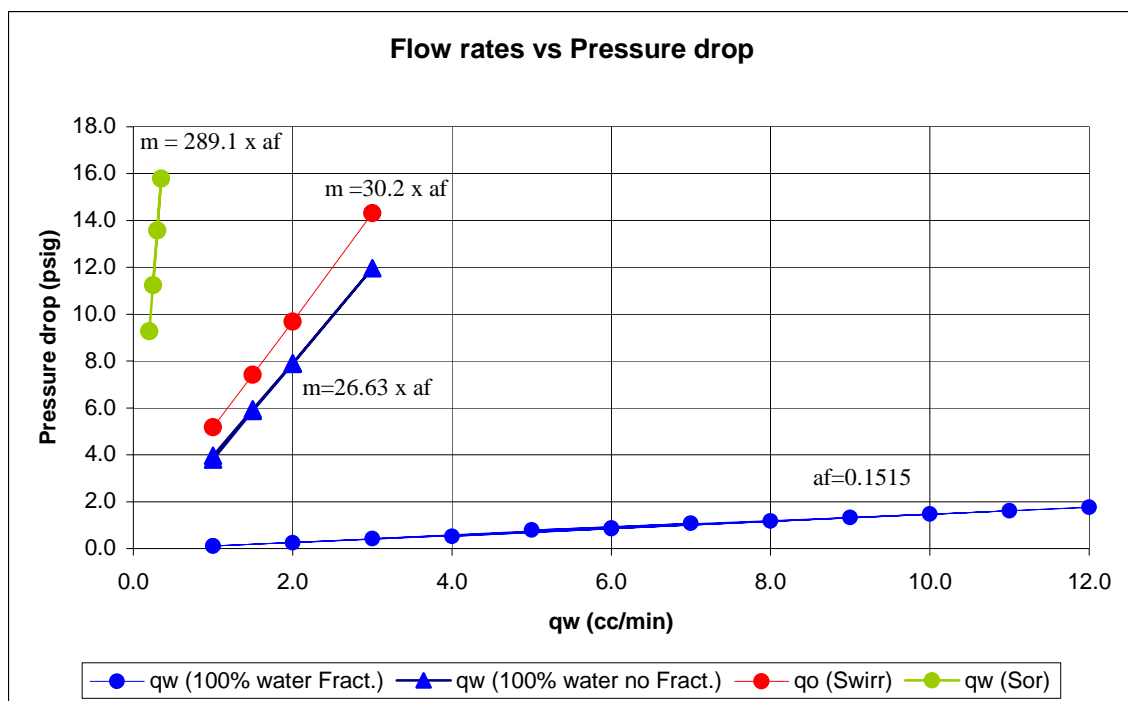


Figure 5.61: Pressure drop as a function of flow rate for a non-fractured and a fractured core.

Reversing the flow direction in the fracture allows the fluids to rearrange and release the pressure buildup. This fracture plugging behavior can be directly related to problems with gas wells, where field data report possible water slugs plugging wells in hydraulically fractured gas reservoirs, Christiansen *et al.* (2005). Some of the field solutions for re-establishing the flow for these type of wells have been injecting from the top of the wells (reversing flow).

5.4.2 Confining pressure from 500 to 2500 psig

The sample was at a saturation condition created by steady water and oil injection prior to increasing the confining pressure. During the increase in confining pressure the system was at low water flow rate (0.3 cc/min). Figure 5.62 shows a schematic of the fracture system after changing the confining pressure from 500 to 2500 psig.

The volume of the fracture prior to the change in confining was 375.8 mm and, 280.4 mm after increasing the confining pressure. Table 5.7 shows the fracture and fluids volume for the two different confining pressures, before and after changing the confining stress.

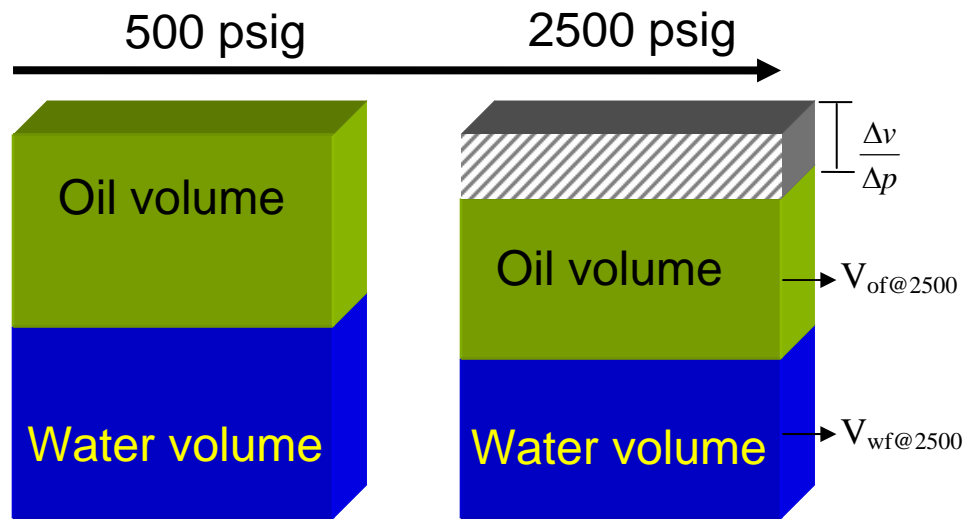


Figure 5.62: Schematic of the volume changes with confining pressure.

The oil saturation decreased by about 6% indicating a preferential removal of oil from the fracture, though both oil and water were removed (oil volume removed: 52.5 mm³, water volume removed: 43.1 mm³).

Table 5.7: Volume change with confining pressure. Before and after P_c changes

Confining pressure (psig)	Fracture volume (mm ³)	Oil Volume (mm ³)	Water Volume (mm ³)	Oil saturation	Water saturation
500	375.8	142.4	233.5	37.9	62.1
2500	280.4	89.9	190.4	32.1	67.9

The increase in confining pressure reduced the volume of the fracture and changed the volume of the water and oil present in the fracture. The volume of fluids that disappeared from the fracture could either flow out of the system through the ends of the fracture or flow into the matrix.

Average CT profiles from the matrix adjacent to the fracture are presented in Figures 5.63 and 5.64. In Figure 5.64 CT profiles for the dry and wet conditions are shown to highlight the significant difference in CT values.

Figure 5.64 highlights the similar CT registration of the matrix at 500 and 2500 psig confining pressure, indicating that migration of fluids from the fracture to the matrix did not occur. A material balance would be useful to corroborate the production of the fluids from the fracture. However, given the small changes in volume and the magnitude of the dead volume such a balance calculation is not viable.

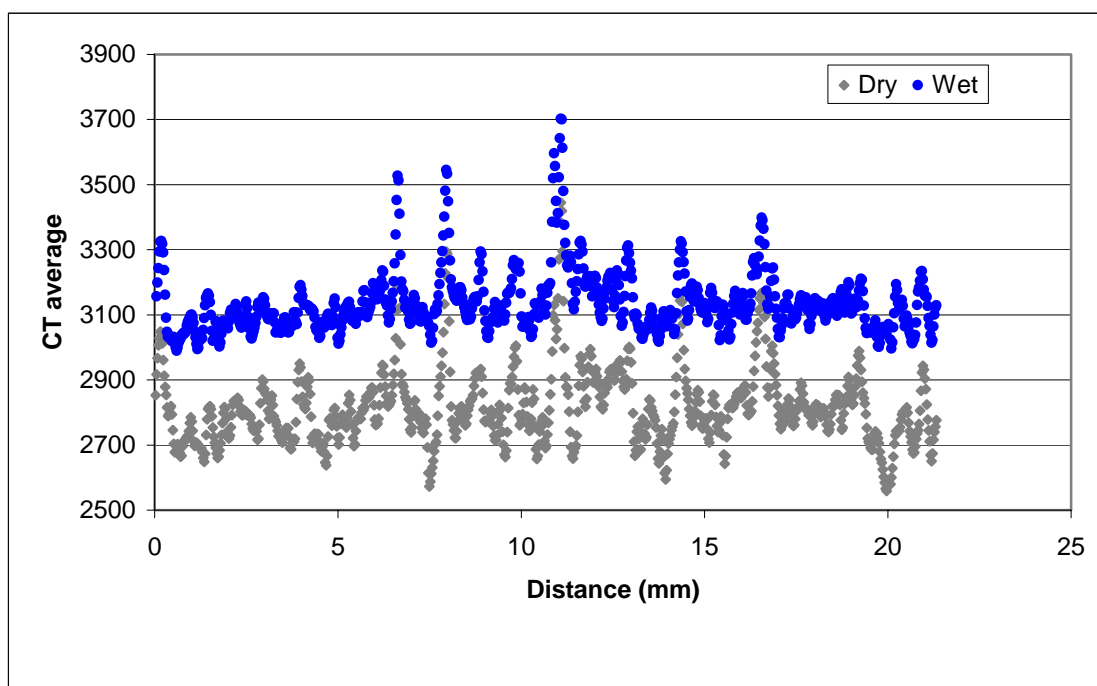


Figure 5.63: CT profile in the matrix area near the fracture (Dry and Wet).

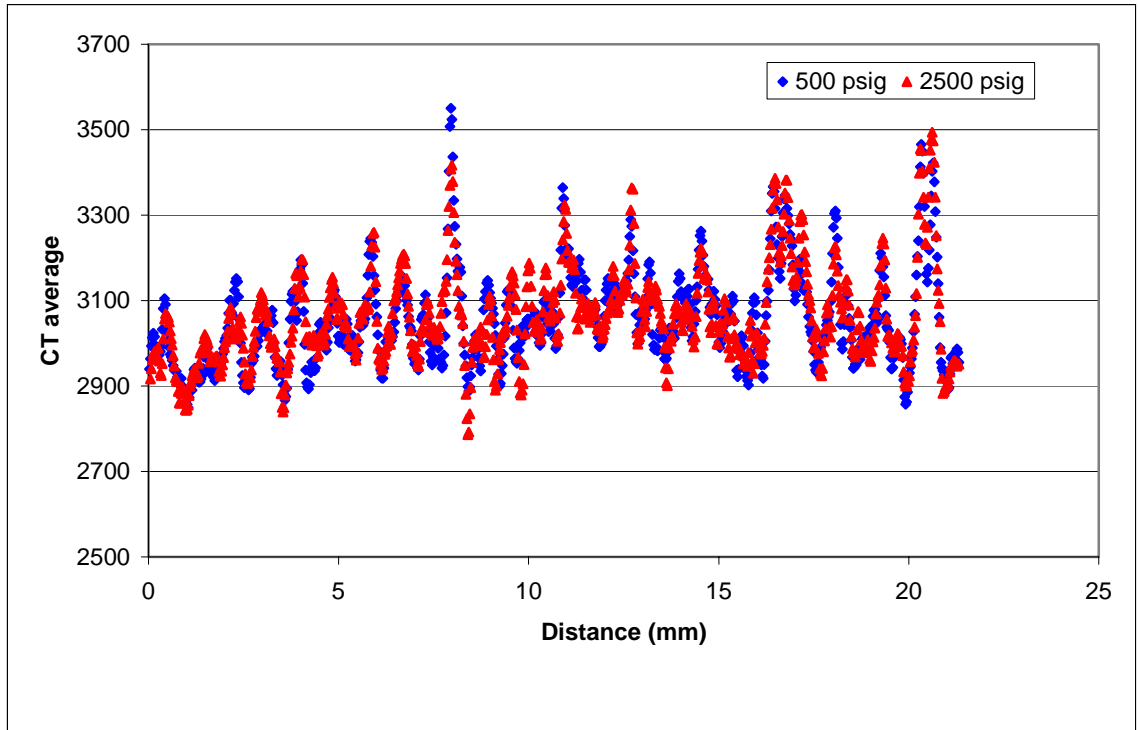


Figure 5.64: CT profile in the matrix area near the fracture at 500 and 2500 psig.

After increasing the confining pressure from 500 to 2500 psig a new state of residual oil saturation was reached and the system was scanned at this condition. Figure 5.65 shows the three dimensional distribution of the residual oil saturation in the fracture at 2500 psig. The fracture volume was 280.4 mm^3 .

Table 5.8 shows the values of the fluids saturation before and after the changes in confining pressure. The oil saturation in the fracture was 41.3% at 2500 psig, more than double the saturation of the oil saturation at 500 psig (18.6%).

Table 5.8: Fracture fluids saturation before and after changes in P_c

Confining Pressure (psig)	S_{of} (%)	S_{wf} (%)
500	18.6	81.4
2500	41.3	58.7

Table 5.9 highlights the residual oil saturation for both changes in confining pressure, 500 and 2500 psig. The oil mobile range reduced in 22% from 500 to 2500 psig confining pressure. This significant reduction in mobile oil saturation in the fracture is a key observation that has a major effect on the recovery oil from the fracture.

Table 5.9: Residual oil saturation and mobile at 500 and 2500 psig

Confining Pressure (psig)	S_{orf} (%)	Mobile Oil (%)
500	18.6	70
2500	41.3	48

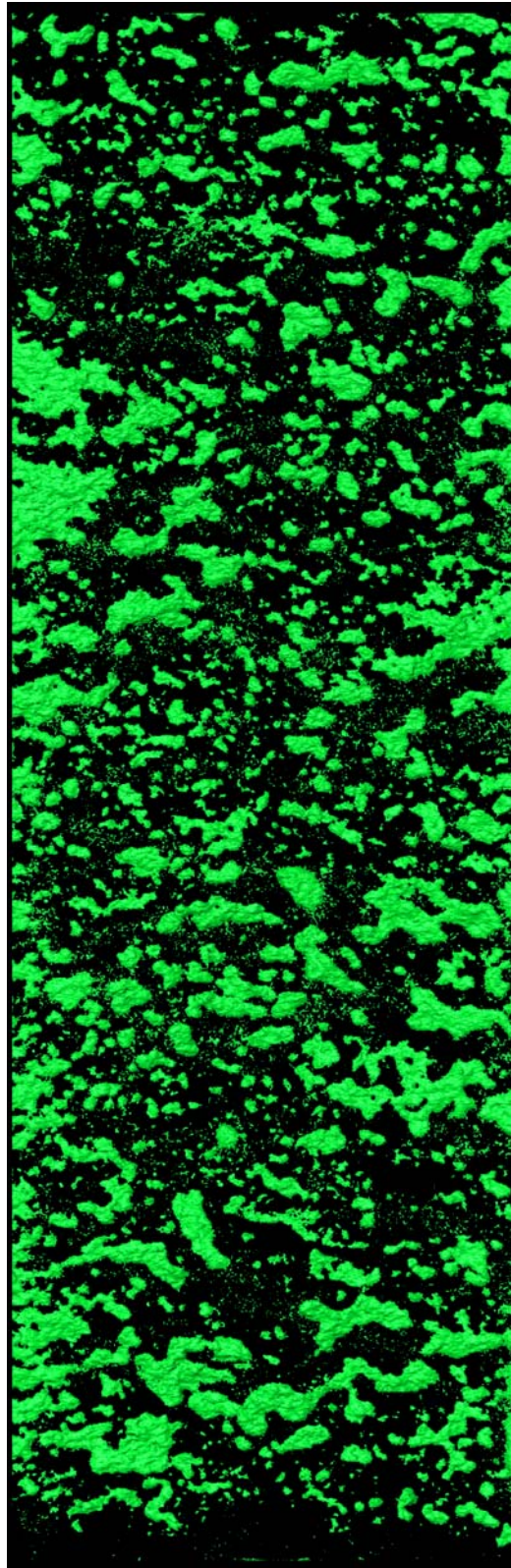


Figure 5.65: Residual oil saturation map at 2500 psig.

Different fractional flow injections were performed at 2500 psig, showing similar behavior to the responses seen prior to increasing the confining pressure. Figure 5.66 shows the pressure drop along the fracture as function of fractional flow of water at 2500 psig. The imbibition curve ended above the drainage curve indicating changes in the internal distribution of the phases.

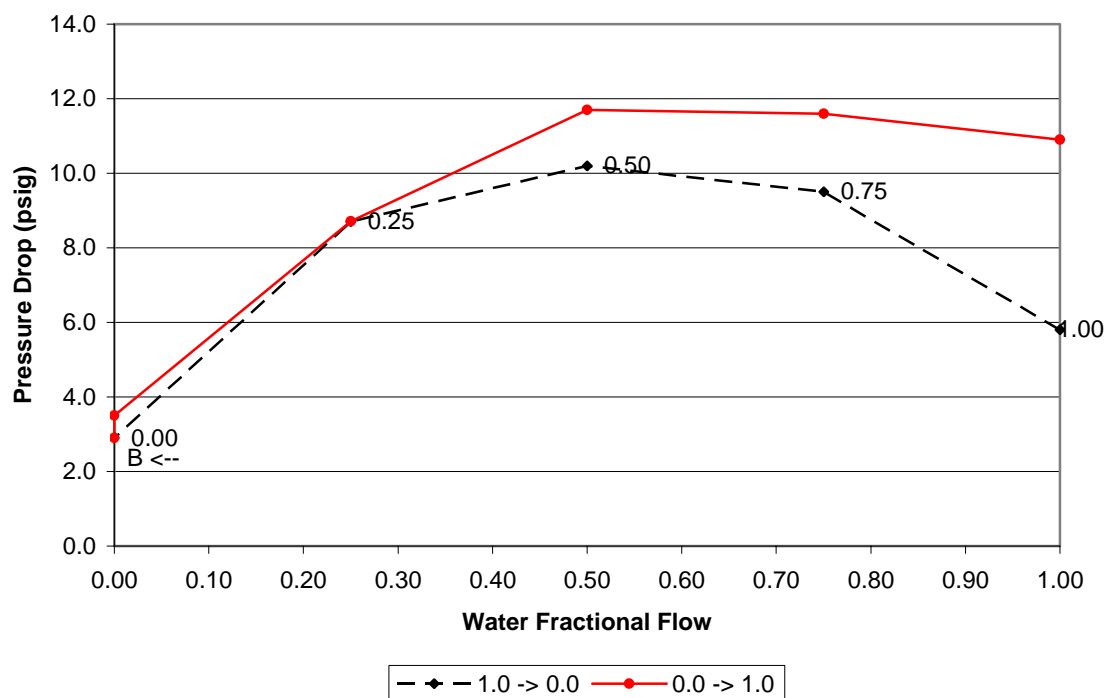


Figure 5.66: Pressure drop in the fracture at 2500 psig for a total liquid flow rate of 1cc/min.

The isolation of the fracture at the first confining pressure state (500 psig) was done by extracting the digital fracture from the dry scans. Since the sample was not moved during the experiment, excellent CT registration was obtained and the virtual fracture from the dry scans was used to isolate the fracture in the other condition. The situation at the high confining pressure (2500 psig) was different as the sample was saturated. To obtain the dry scans the sample was cleaned by injecting Ethyl Alcohol (dozen of pores volumes). Figure 5.67 shows the changes of CT values at a fixed position as a function of time. When the CT values stabilized the sample was displaced by nitrogen and then vacuum dried. Once dry conditions were established the sample was scanned and the virtual fracture at a confining pressure of 2500 psig was extracted.

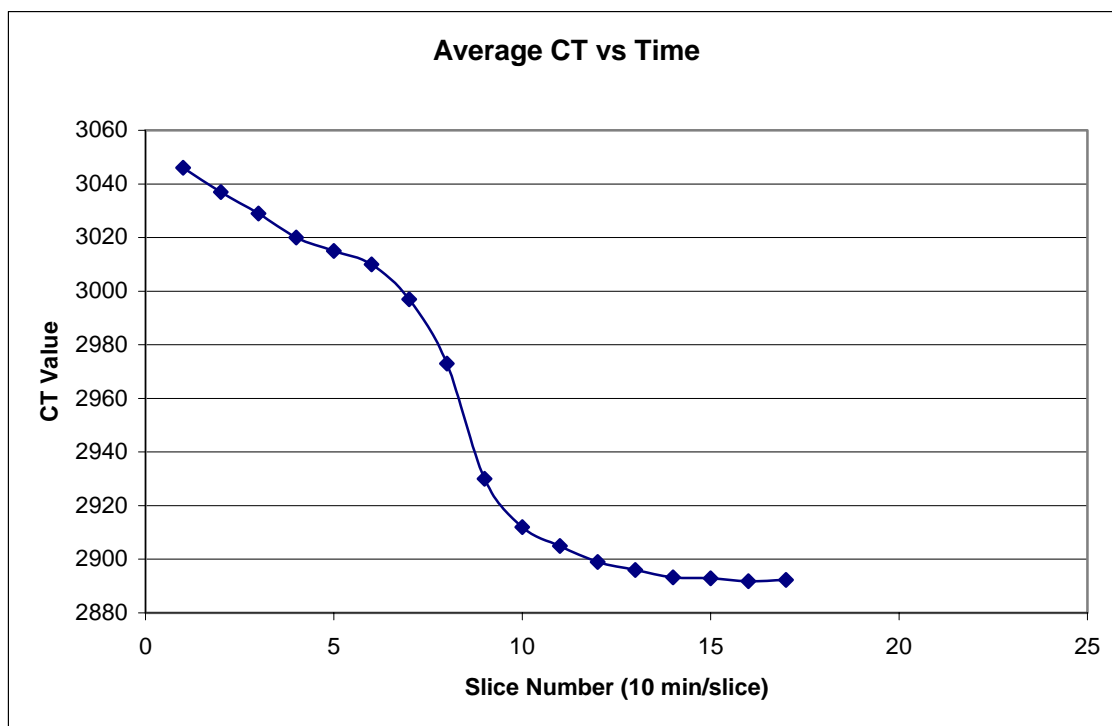


Figure 5.67: Changes in CT average (2500 psig) after injecting alcohol and vacuum drying of sample.

The fracture volume for the fracture at 2500 psig was computed showing a reduction in volume from 375.8 to 280.4 mm³. Figure 5.68 shows three-dimensional renditions of the fracture at 500 and 2500 psig at dry condition demonstrating a significant increase of asperities. An aperture fracture thickness map for both cases is shown in Figure 5.69 highlighting regions with conductivity (bright areas), while the red color denotes the asperities. A total of 2.9% of the aperture thickness map corresponds to asperities for the case of 500 psig, while 11.9% corresponds to the case where the confining pressure was raised to 2500 psig. This core shows a much higher change in the percentage of asperities (9%) than previous cases (Core BS1), where only 4.1% changes in asperities area for the same change in confining pressure.

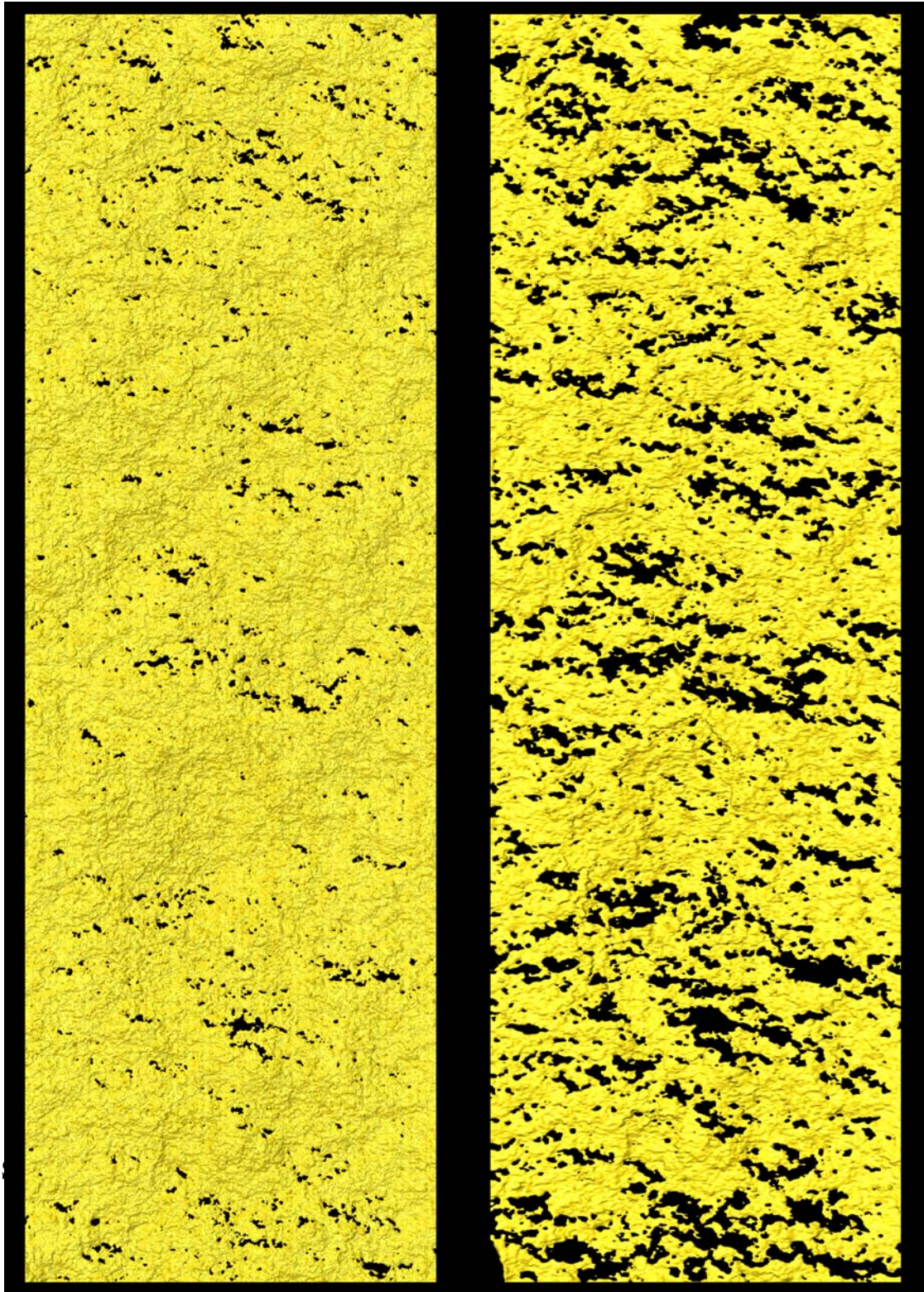


Figure 5.68: Three-dimensional recreation of the fracture at 500 (left) and 2500 (right) psig.

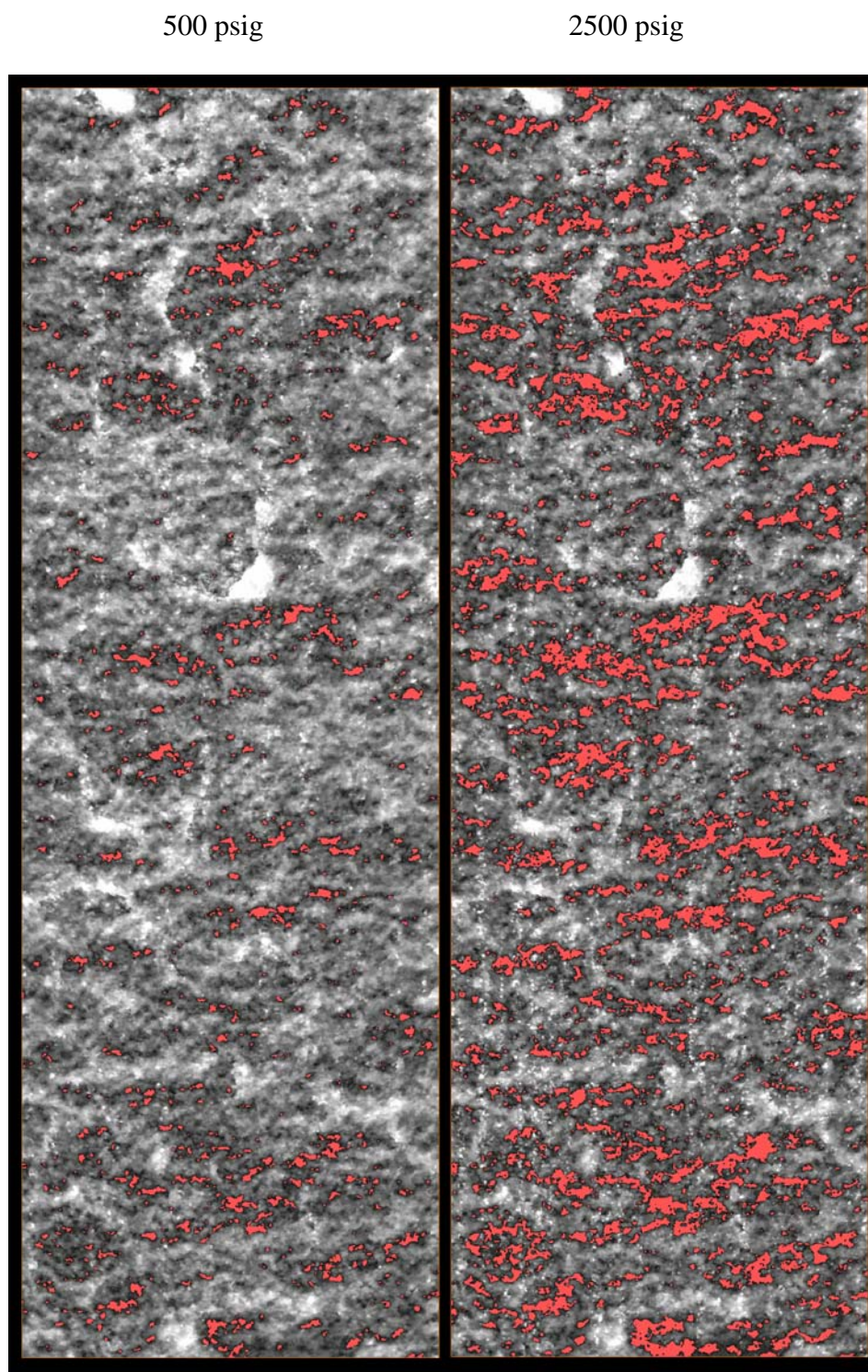


Figure 5.69: Thickness aperture map of the fracture at 500 (left) and 2500 (right) psig.

CHAPTER 6

CONCLUSIONS

A study of the behavior of multiphase flow in a tensile fracture has been performed. This study includes the characterization and the interaction of the fluids during mechanical changes in the tensile fracture using MCT. The EPC and SMI methods were used to demonstrate the fracture structure response to changes in confining stress. These characterizations will be significant in our ability to classify different fractures based on their topology. The distribution of the oil and water along the fracture have a significant impact on pressure drop and therefore on fluid transport and recovery. The change in fracture aperture has a significant impact on the fracture pore space and therefore on fluid occupancy. The redistribution of the phases in the fracture, as a consequence of changing confining stress, controls the multiphase transport properties of the fracture. The following observations and conclusions are made:

1. The distribution of the phases along the fracture modifies the conductivity of the fracture. The non wetting phase produces plugging regions that drastically reduce the multiphase conductivity of the fracture. This fracture plugging behavior can be directly related to problems with gas wells, where field data report possible water slugs plugging wells in hydraulically fractured gas reservoirs.

2. The use of the cubic law for flow through fractures severely over estimates the permeability of the fractures studied in this research. The conductivities were much lower than the predicted by the cubic law.
3. In the cases studied, relative permeabilities deviated significantly from the x-shaped curves typically used for fractures systems. In particular the conventional assumption grossly over predicts K_{ro} . Application of these observations should greatly improve accuracy of dual-permeability simulators.
4. As expected, increasing the confining pressure reduced fracture aperture and absolute permeability. Aperture closure correlates with reduction in absolute permeability. A general increase in asperity contact area accompanied the observed aperture reduction.
5. The increase in confining stress caused significant reduction in the residual oil saturation in the fracture. This reduction in residual oil saturation (S_{or}) has a major effect on the change of relative permeabilities and on the mobile saturation range of a fracture. The residual water saturation (S_{wirr}) remained constant at the pressure ranges used in this experiment.
6. Flow instability of the pressure drop during drainage and imbibition cycles was observed.

7. At constant fracture fractional flow a continuous decrease in the fracture conductivity was observed. This reduction in conductivity was not stable and was removed by reversing the flow. X-rays CT confirmed the hypothesis that instability is caused by change in phase distribution in the fracture with little change in saturation.
8. A methodology for computing a deterministic coefficient for measuring the connectivity density, EPC, (connections per unit volume) and the fracture structure model index, SMI, of a fractured system was presented. In the future, we expect to correlate multiphase hydraulic properties of the fracture and these topological coefficients.

REFERENCES

1. Alajmi, A. F. and Grader, A. S.: "Analysis of Fracture-Matrix Fluid Flow Interactions Using X-ray CT," SPE Eastern Regional Meeting, Morgantown, West Virginia, SPE 65628, 2000.
2. Alvarado, F. E., Grader, A. S., Karacan, O. and Halleck, P. M.: "Visualization of Three Phases in Porous Media Using Micro Computed Tomography," Petrophysics **45**, 2004.
3. Babadagli, T. and Ershaghi, I.: "Imbibition Assisted Two-Phase Flow in Natural Fractures," SPE, 1992.
4. Barton, N. S., Bandis, S. and Bakhtar, K.: "Strength, deformation and conductivity coupling of rock joints," Int. R. Mech., **22**: 121-140, 1985.
5. Chen, D. W., Zimmerman, R. W. and Cook, N. G. W.: "The effect of contact area on the permeability of fractures," 30. US symposium on rock mechanics, Morgantown, WV (USA), 1989.
6. Christiansen, R., Mayoral, C. and Pereira, C.: "Capillary End Effects and Gas Production From Low Permeability Formation," SCA, Canada, 2005.
7. Durham, W. B., Bourcier, W. L. and Burton, E. A.: "Direct observation of reactive flow in a single fracture," Water Resources Research **37** (1): 1-12, 2001.

8. Gale, J. E.: "Comparison of coupled fracture deformation and fluid flow models with direct measurement of fracture poro-structure and stress-flow properties," Symposium of Rock Mechanics, 1987.
9. Gentier, S. and Hopkins, D.: "Mapping fracture aperture as a function of normal stress using a combination of casting, image analysis and modeling techniques," Int. R. Mech. **34**: 3-4, 1986.
10. Grader, A. S. and O'Meara, D. J., Jr.: "Dynamic Displacement Measurements of Three-Phase Relative Permeabilities Using Three Immiscible Liquids," SPE Annual Meeting, Huston, Texas, 1998.
11. Gray, H. D., Fatt, I. and Bergamini, G.: "The Effect of Stress on Permeability of Sandstone Cores," SPEJ: 95-100, 1963.
12. Hicks, P. J., Jr., Deans, H. A. and Narayama, K.: "Distribution of Residual Oil Saturation on Heterogeneous Carbonate Cores Using X-Ray CT," SPE: 235-239, 1992.
13. Hildebrand, T. and Ruegsegger, P.: "Quantification of Bone Microarchitecture with the Structure Model Index," Computer Methods in Biomechanics and Biomedical Engineering **1**: 15-23, 1997.
14. Horie, T., Firoozabadi, A. and Ishimoto, K.: "Laboratory Studies of Capillary Interaction in Fracture/Matrix Systems," SPE, 1990.
15. Iwai, K.: "Fundamental studies of flow through a single fracture," Berkely, University of California, 1976.

16. Keller, A. A.: "Single and Multiphase Flow and Transport in Fractured Porous Media," Stanford, California, Stanford University, 1996.
17. Khilar, K. C. and Fogler, H. S.: "Colloidally induced fine migration in porous media," Reviews in chemical engineering **No. 4**: 41-108, 1987.
18. Lomize, G. M.: "Flow in Fractured Rocks" (in Russian). Gosenergoizdat, Moscow: 127, 1951.
19. Louis, C.: "A study of groundwater flow in jointed rock and its influence on the stability of rock masses," Rock Mech. Res Rep. **10**: 90, 1969.
20. Montemagno, C. D. and Pyrak-Nolte, L. J.: "Fracture Network Versus Single Fractures: Measurement of Fracture Geometry with X-ray Tomography," Phys. Chem. Earth **24 (7)**: 575-579, 1999.
21. Neuzil, C. E. and Tracy, J. V.: "Flow Through Fractures," Water Resources Research **17**: 191-199, 1981.
22. Odgaard, A. and Gundersen, H.: "Quantification of Connectivity in Cancellous Bone, with Special Emphasis on 3-D Reconstructions," Bone **14**: 173-182, 1993.
23. Persoff, P. and Pruess, K.: "Two-Phase Flow Visualization and Relative Permeability Measurements in Natural Rough-Walled Rock Fractures," Water Resources Research **31 (5)**, 1985.
24. Pyrak-Nolte, L. J., Montemagno, C. D. and Nolte, D. D.: "Volumetric Imaging of aperture distribution in connected fracture networks," Geophysical Research Letters **24:18**: 2343-2346, 1997.

25. Pyrak-Nolte, L. J., Myer, L. R., Cook, N. G. W. and Witherspoon, P. A.:
 "Hydraulic and mechanical properties of natural fractures in low permeability rock," Proceedings of the 26th International Congress of Rock Mechanics, 1987.
26. Pyrak-Nolte, L. J., Nolte, D. D., Myer, L. R. and Cook, N. G. W.: "Fluid flow through fractures," Proceedings of the International Symposium on Rock Joints, Norway, 1990.
27. Raven, K. G. and Gale, J. E.: "Water flow in a Natural Rock Fracture as a Function of Stress and Sample Size," Int. R. Mech. Min. Sci. & Geomech. **22 (4)**: 251-261, 1985.
28. Schrauf, T. W. and Evans, D. D.: "Laboratory Studies of Gas Flow Through a Single Fracture," Water Resources Research **22 (7)**: 1038-1050, 1986.
29. Tsang, Y. W.: "The effect of tortuosity on fluid flow through a single fracture," Water Resources Research **20 (9)**: 1209-1215, 1984.
30. Tsang, Y. W. and Tsang, C. F.: "Channel Model of Flow Through Fractured Media," Water Resources Research **23 (3)**: 467-479, 1987.
31. Walsh, J. B.: "The effect of pore pressure and confining pressure on fracture permeability," Int. R. Mech. Min. Sci. & Geomech. **18**: 429-435, 1981.
32. Walter, D. A. and Wong, R. C. K.: "The hydraulic and mechanical response if an oil sand fracture under a varying pressure," Can. Geotech. J **36**: 262-271, 1999.

33. Wang, S. Y., Ayral, S. and Gryte, C. C.: "Computed Tomography for the Observation of Oil Displacement in Porous Media," SPE: 53-55, 1984.
34. Wellington, S. L. and Vinegar, H. J.: "X-Ray Computerized Tomography," Journal of Petroleum Technology: 885-887, 1987.
35. Witherspoon, P. A., Wang, J. S. Y., Iwai, K. and Gale, J. E.: "Validity of cubic law for fluid flow in a deformable rock fracture," Water Resources Research **16**: 1016-1024, 1980.
36. Yeo, I. W., Freitas, M. H. and Zimmerman, R. W.: "Effect of shear displacement on the aperture and permeability of a rock fracture," Int. J. Rock. Mech. Min. Sci. Geomech. **35**: 1051-1070, 1998.
37. Zimmerman, R. W., Kumar, S. and Bodvarsson, G. S.: "Lubrication theory analysis of the permeability of rough-walled fractures," International Journal of Rock Mechanics and Mining Science and Geomechanical Abstracts **28(B12)**: 325-331, 1991.

VITA

Freddy Alvarado

Freddy Alvarado was born in Caracas, Venezuela. He earned a bachelor degree in Petroleum Engineering from Universidad Central de Venezuela in 1999, a Master degree in Petroleum and Natural Gas engendering and a Minor in High Performance Computing from The Pennsylvania State University. In 1997 and 1998 he was award with two scholarships from Universidad Central de Venezuela and from PDVSA-CIED. During 1999 he was appointed as instructor of the petroleum department in the Universidad Central de Venezuela. During his undergraduate and graduate studies he has been exposed to the academic and professional environment through different internships. He has two summer internships with British Petroleum Oil Company in the Exploration and Production Technology Group, where he worked in the Reservoir Performance Technology Unit in 2003 and in the Excellence in Performance Predictions in 2004. His research and develop activities were in reservoir modeling and reservoir simulation. His main research areas are reservoir engineering modeling, three-phase flow in porous media at pore-scale, and multi-phase flow in fractures using high-resolution x-ray computed tomography. Topics were he has several publications.